8-2019

Near-infrared Observations of Herbig Ae/Be Stars

Steven Cade Adams

Clemson University, cadeadams23@gmail.com

Follow this and additional works at: https://tigerprints.clemson.edu/all_dissertations

Near-Infrared observations of Herbig Ae/Be stars

A Dissertation
Presented to
the Graduate School of
Clemson University

In Partial Fulfillment
of the Requirements for the Degree
Doctor of Philosophy
Physics

by
Steven Cade Adams
August 2019

Accepted by:
Dr. Sean Brittain, Committee Chair
Dr. Máté Ádámkovics
Dr. Dieter Hartmann
Dr. Joan Marler

Abstract

One of the most open-ended philosophical questions a person can ask is "Where did we come from?" This question can be interpreted and approached from a multitude of angles. The work presented here will be investigating this question from the astronomical/physical perspective by studying the astronomical objects that are thought to be the immediate precursors to solar systems like our own. In order to determine how we came to be, we must first learn how our home was created.

My research area focuses on the study of the circumstellar disks around intermediate mass (2 - 8 $M_\odot$) young stellar objects, known as Herbig Ae/Be stars. These stars have been observed to harbor large disks of gas and dust left over from their parent molecular cloud. It is within these disks where planet formation is believed to be on-going. Our current models of planet formation are unable to fully depict the process of creating planets from the dusty, gaseous disk. Therefore, in order to understand how these disks create the planetary systems we now know to be ubiquitous, we must first improve our understanding of the composition of and physical processes occurring within the circumstellar disk.

Observing the molecular emission originating in the inner 10 au of these circumstellar disks allows us to understand the composition and physical environment where terrestrial planet formation is believed to occur. Molecular emission can provide a wealth of information on the inner disk. Observing multiple rovibrational transitions can give insight on the temperature of the gas. The emission line profile can also provide information on the location of the gas within the disk. The primary molecular species discussed in this research are OH, H_2O, and CO. These are the three most abundant molecules present in the circumstellar disk behind H_2, but all are more easily studied in the near-infrared wavelength regime.

In this dissertation, I present my findings on HD 101412. This source presented the first

direct detection of water vapor emission in the near-infrared. Previous observations of Herbig Ae/Be stars have yielded detections of OH, yet water has been more elusive. Due to the strong far-ultraviolet radiation fields produced by the A and B-type central star, it is believed that most of the water vapor within the disk is photodissociated. This would increase the amount of OH within the upper layers of the disk atmosphere that are irradiated most directly. HD 101412 is also unique in that we observe it nearly edge-on and the gas-to-dust ratio is high compared to other Herbig Ae/Be sources. These factors combine to allow us to observe a larger column of water vapor in the disk which allows the emission to be observable above the continuum.

I also observed OH emission in the V380 Ori multiple star system to determine the variability of asymmetrical emission lines previously reported. The observation of multiple OH $\nu = 1 \rightarrow 0$ rovibrational transitions allow for the gas temperature to be determined. This, coupled with archival CO data, present information that point to a vertical temperature gradient within the V380 Ori circumstellar disk. Both the OH and CO emission line profiles show CO and OH to be co-spatially located, however, the OH gas appears to be hotter, thus higher in the disk atmosphere, than the CO emission. This is consistent with models that show OH should be more abundant in the upper atmosphere due to the irradiation from the far-ultraviolet radiation from the central star. Our observations are unable to reproduce the asymmetry previously reported in the OH emission. High-resolution CO emission also lacks the observed asymmetry. Due to the timescales on which these data were acquired, it can rule out the previously reported asymmetry being caused by an eccentric inner disk due to the presence of a stellar companion located within the molecular emission.

A survey on OH and H_2O emission in Herbig Ae/Be disks, expanding on previous studies, is also presented here. Two more detections of water vapor emission are presented, along with five more detections of OH P4.5 (1+,1−). This increases the sample of OH detections in Herbig Ae/Be disks to 15 out of 31 (48.4%) of sources with observations in the near-infrared. The relative strength of the OH and water emission is compared to different stellar and disk parameters of Herbig Ae/Be and T Tauri sources. This provides insight as to what could be the cause of the lack of water vapor emission observed around Herbig Ae/Be stars.

Finally, a survey of hydrogen recombination emission lines is presented in an effort to understand the physical origins within the Herbig Ae/Be system. Integral field spectroscopy is combined with spectro-astrometry to study the disk-star interface of Herbig Ae/Be stars. Two H I emission lines are studied (Paβ and Brγ) to determine if they are produced directly by accretion onto the star,

or if they originate from more extended regions of the system. Initially attempts are made to remove artifacts in the spectro-astrometric analysis via the use of models. Ultimately, it is concluded that these artifacts are not removed entirely. Later data is acquired such that artifacts can be removed organically via the combination of parallel and anti-parallel observing position angles. The emission lines observed in each observing run can provide some insights based on the overall line profile. Only the spectro-astrometric information from data acquired with parallel and anti-parallel observations can be relied upon to provide information on milliarcsecond scales.

Dedication

First and foremost, I would not be the man or scholar I am today without the support provided by Harold Glen Wofford in my younger days. There has never been a more selfless, caring, or gracious human being in my life. From the early mornings he would spend with me before he left for work and I for school, all the way until my time at the University of Georgia getting my Bachelor's degree, I cherish every memory I have with him. His constant support and love provided me the strength to finish my PhD. I know that I am where I am today thanks to the morals instilled in me by both Glen and Winnell Wofford. Thanks for always being there for me.

My wife, Kendall, also deserves copious commendation for her infinite patience. This entire journey would not have been possible without you by my side. You have always been there to keep me grounded and provide support when it was required. My life with you has been nothing but happiness and I look forward to our future life together and the adventures it entails.

Finally, my parents deserve an immense amount of credit. They allowed and supported my pursuit of Physics and Astronomy during my undergraduate studies, and were supportive throughout my graduate career as well. The warm and nurturing environment you provided set me up to tackle the exacting nature of pursuing a PhD. I owe my work ethic and moral make-up to the household you provided me during my adolescence.

Acknowledgments

I would like to thank Dr. Sean Brittain for his tireless guidance during my time under his tutelage. The patience he exhibited while I finished up my writing is to be commended. I would also like to thank the office staff in the Department of Physics: Deb Helvie, Amanda Crumpton, Celeste Hackett, Lori Rholetter, and Risé Sheriff. These are the true heros that keep the Physics and Astronomy Department running like a well oiled machine. I would also like to extend my gratitude to the Astronomy faculty: Máté Ádámkovis, Marco Ajello, Dieter Hartmann, Mark Leising, Bradley Meyer, Jeremy King, Jason Brown, and Lih-Sin The. Thanks for the time you spent outside of the classroom discussing various topics both scholarly and worldly. I would also like to thank Dr. Joan Marler for being a part of my dissertation committee and for providing guidance when any molecular spectroscopy questions arose.

To all of my fellow Physics Graduate Students, young and old, thanks for the camaraderie only those suffering through similar experiences can provide. A special thanks to Shannon Stefl, Amber Porter, Courtney McGahee, Andrew Garmon, Lucas Hurd, Ethan Kilgore, Nirmal Nischal, Sam Sanders, Amy Gall, Steve Bromley, Aman Kaur, and Argo Chakravorty for the social time to help keep stresses lowered. Special thanks are also in store for John Kozlowski and Deighton Abrams for putting up with a group like those listed previously.

Table of Contents

List of Tables

List of Figures

Chapter 1

Introduction

1.1 Circumstellar disks

Our current understanding of star formation indicates that circumstellar disks are a ubiquitous feature in the early stages of a star's life (10^6 - 10^7 years; Haisch et al. 2001; Mamajek et al. 2004; Alexander et al. 2014). As stars form from a molecular cloud, the surrounding material that is not contained in the initial core that forms the central star forms an envelope that surrounds the star. Eventually, this envelope will accrete onto the disk of gas and dust around the star, due to conservation of angular momentum. Some of this material in the disk will be accreted onto the central star, photoevaporated, ejected in outflows, and some material will form planets, comets, and asteroids in a future planetary system (Adams et al., 1987). Figure 1.1 shows the basic components of the circumstellar disk around a young stellar object (YSO).

This is the current road-map to circumstellar disk formation as we understand things. The processes required to form planets are less clearly understood. In order to arrive at the correct planet formation scenarios, we must fully understand the make-up and dynamics of the circumstellar disk. Spectroscopy is one method to study the circumstellar environment in order to determine the composition and conditions.
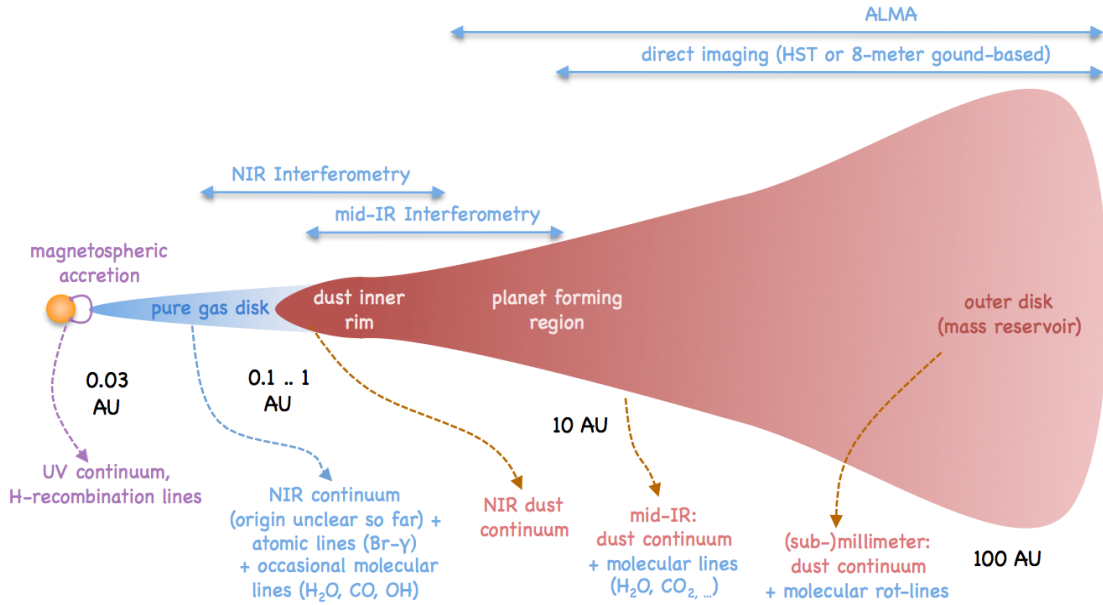
Figure 1.1: Figure from Dullemond & Monnier (2010). This schematic of a circumstellar disk labels different regions of the disk and the wavelength regimes where they are observed. This image is not to scale.

1.2 Herbig Ae/Be Stars

Herbig Ae/Be (HAeBe) stars are intermediate mass (2-8 $M_\odot$) pre-main sequence stars that have a spectral type of F6-B0 and have an excess of infrared (IR) flux in their spectral energy distribution (SED) that is associated with circumstellar materials (Herbig, 1960; Hillenbrand et al., 1992). Thé et al. (1994) have extended the definition to include sources that present an anomalous extinction law, exhibit photometric variability, and Mg II emission lines. They also exhibit hydrogen emission features in their spectra. The spectral cutoff for this classification is due to the physical differences between early and late type stars. Late type (Type M - F7) stars have outer convective layers (Figure 1.2). This convection leads to the creation of magnetic fields which interact with the circumstellar material accretion onto the stellar surface or possibly ejection of material along field lines.

Early type (Type F6 - O) stars have a radiative outer layer. Since the plasma in the outer layers of these stars is not circulating as in late type stars, early type stars generally lack strong magnetic fields. While this is the case, some early type stars have been observed to possess fossil magnetic fields (Alecian et al., 2008). Observations of more massive stars indicate that accretion
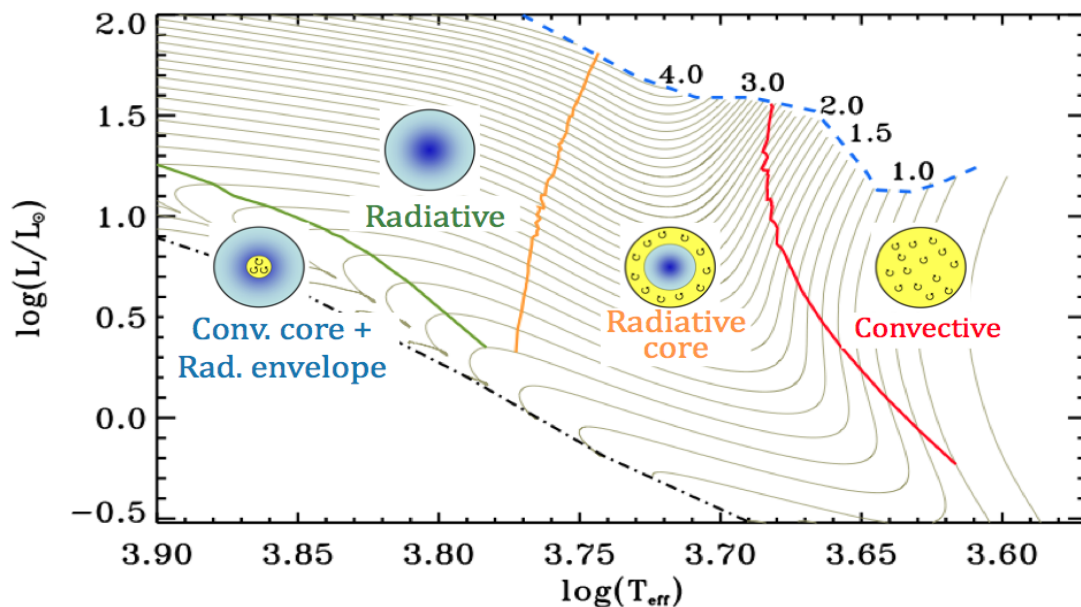
Figure 1.2: Figure from Hussain & Alecian (2014). This section of a Hertzsprung-Russell diagram shows some pre-main sequence evolutionary tracks for different mass stars, while also showing the combinations of temperature and luminosity for which a radiative or convective outer layer is present in a star.

still occurs within these systems, so it is still an open question as to how these stars accrete. A possible tracer for accretion processes in HAeBe stars is hydrogen recombination emission lines.

HAeBe stars can be further classified into two groups: Group I and Group II (Meeus et al., 2001). This classification scheme is based off characteristics observed in the SED of the source. HAeBe sources show evidence of excess emission in the IR, however, the level of excess emission is not consistent across all HAeBes. Group I sources show strong, and sometimes rising, mid-infrared (MIR) excesses. This has been attributed to a flared geometry of the circumstellar environment. The close, inner portion of the circumstellar disk is directly irradiated by the central star, causing it to puff up slightly and block the region immediately behind the puffed region. Eventually, the outer disk flares to a point where it can intercept some of the stellar radiation, causing it to warm and emit at longer wavelengths. Group II disks have a flat geometry in the outer portions. Because of this, the MIR and far-infrared (FIR) parts of the SED are not as strong. Group I disks can also be divided further into Group Ia and Ib disks. Group Ia sources show emission from silicates and/or polycyclic aromatic hydrocarbons (PAH) between 3 and 50 μm, while Ib lack this emission. The lack of these emission features in Group Ib sources is attributed to the absence of small silicate grains in
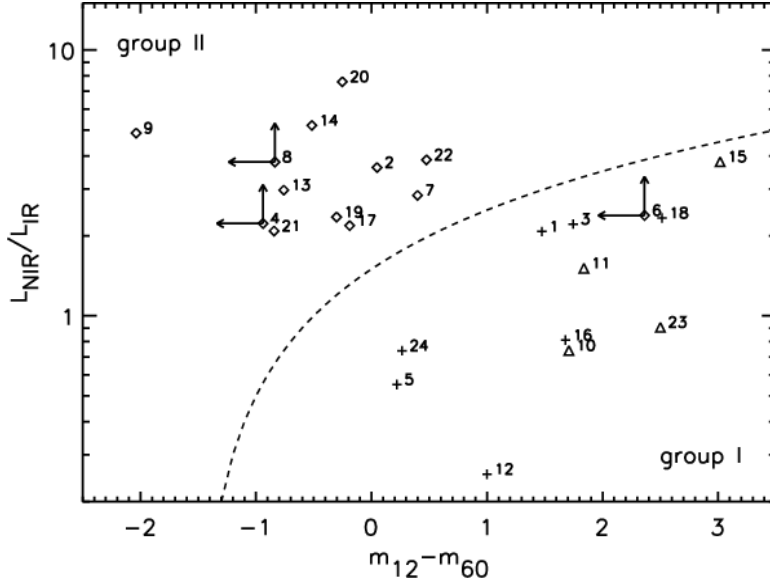
Figure 1.3: Figure from van Boekel et al. (2005). A plot of L_{NIR}/L_{IR} vs m_{12}-m_{60} as determined from photometric observations of Herbig Ae/Be stars.

the disk. van Boekel et al. (2005) quantified this classification scheme with Group I sources having $L_{NIR}/L_{IR} \leq (m_{12}$-$m_{60}) + 1.5$ and Group II having $L_{NIR}/L_{IR} > (m_{12}$-$m_{60}) + 1.5$ (Figure 1.3).

The scale height of the circumstellar disk can be estimated by comparing the relative strengths of the pressure exerted by the gas in the disk and the vertical gravitational force. If the disk is not self-gravitating, then the dominant source of gravity is the central star. Thus, the vertical acceleration due to gravity is simply

$$g_z = g \sin \theta = \frac{GM_*}{(r^2 + z^2)} \frac{z}{(r^2 + z^2)^{1/2}}. \tag{1.1}$$

If we assume that the disk is in vertical hydrostatic equilibrium, the gravitational acceleration must be balanced with the vertical pressure gradient in the gas, $(1/\rho)(dP/dz)$. If we assume the disk is vertically isothermal and rewrite the pressure gradient equation in terms of density and the speed of sound, c_s, we get

$$\frac{1}{\rho} c_s^2 \frac{d\rho}{dz} = \frac{GM_*}{(r^2 + z^2)} \frac{z}{(r^2 + z^2)^{1/2}}. \tag{1.2}$$

If the disk is geometrically thin, then z << r and the right hand side of Equation 1.2 can be simplified such that

$$\frac{1}{\rho} c_s^2 \frac{d\rho}{dz} = GM_* \frac{z}{r^3}. \tag{1.3}$$

4

With some rearranging, we arrive at

$$\frac{\mathrm{d}\rho}{\rho} = \frac{GM_*}{c_s^2 r^3} z \mathrm{dz}, \text{ where } \Omega_k \equiv \sqrt{\frac{GM_*}{r^3}}. \tag{1.4}$$

Ω_k is the Keplarian angular velocity. From here, we can integrate each side from the midplane to a height, z', above the midplane,

$$\int_{\rho_o}^{\rho'} \frac{\mathrm{d}\rho}{\rho} = \frac{\Omega_k^2}{c_s^2} \int_0^{z'} z \mathrm{dz}. \tag{1.5}$$

The desity of the disk at the midplane is defined as ρ_o. This gives

$$ln(\rho') - ln(\rho_o) = \frac{\Omega_k^2}{c_s^2} \frac{z'^2}{2} \tag{1.6}$$

This can be simplified to give

$$\rho = \rho_o e^{\frac{z^2}{2H^2}}, \text{ where } H \equiv \frac{\Omega_k}{c_s}. \tag{1.7}$$

In order to determine if the disk will flare as you move out radially from the central star, we must parameterize the sound speed of the disk as a function of radius, r,

$$c_s \propto r^{-\beta}, \tag{1.8}$$

which makes the scale height's radial profile

$$\frac{H}{r} \propto r^{-\beta+1/2}. \tag{1.9}$$

Since the sound speed goes as the square root of the temperature, $T^{1/2}$, for an isothermal gas, this indicates that the circumstellar disk will flare as you move radially outward if the disk temperature profile is $T(r) \propto r^{-1}$ or shallower.

Another class of disks around YSOs are transition disks (Strom et al., 1989; Espaillat et al., 2007). These objects show a lack of near-infrared (NIR) excess emission in their SEDs. The lack of NIR excess is attributed to an absence of dust in the inner region all together. This optically thin region of the disk may still house some gas, which can be observed using spectroscopy.

1.2.1 Hydrogen Emission

Hydrogen is the most abundant atomic species in the universe, so it should not be a surprise that it is also a key ingredient in stellar formation. The primary feature that gives HAeBe stars their name is the observation of hydrogen recombination lines in the optical and IR. However, it is still uncertain as to what the origins of the H I recombination emission are (Kraus et al., 2008b). Various scenarios have been proposed: **(1)** a gaseous inner disk, **(2)** stellar winds, **(3)** magnetospheric accretion, **(4)** stellar driven X-winds, and **(5)** disk winds.

The recombination lines could arise from residual gas in the inner disk. Since the gas is actively accreting onto the star, there must be some gas that is gradually moving inward in the system. This material would lie close to the star and form a mini-H II region. The free electron would recombine with the hydrogen ions and cascade through higher energy levels producing the observed emission.

Stellar winds have been postulated due to the P Cygni profile exhibited by some of the H I emission line profiles. A P Cygni profile is one that exhibits both absorption (in the blue portion of the feature) and emission (in the red portion of the feature). Some HAeBe stars are fast rotators. If they rotate fast enough, the outer layers of the star could be launched as a stellar wind. Seeing that stars are primarily hydrogen, this would provide a shell of hydrogen gas moving away from the star. As such, this gas moving away would impart an absorption feature in the blue portion of any H I feature. Gas within the circumstellar disk would be present such that the emission in the red portion would be observed.

Magnetospheric accretion (Koenigl, 1991; Shu et al., 1994) is a popular theory for how material is accreted from the circumstellar disk onto the surface of T Tauri stars due to their convective outer layers giving rise to magnetic fields with ample strength to channel flows of ionized material. The mass accretion rate of T Tauri stars has been correlated to the luminosity of the Br γ emission line at 2.166 μm (Muzerolle et al., 1998b; Calvet et al., 2004). This correlation extends to HAeBe stars as well (Donehew & Brittain, 2011; Fairlamb et al., 2015), even though HAeBe stars are not expected to have strong magnetic fields. While this is the case, magnetospheric accretion cannot be entirely ruled out as a partial contributor to H I emission (Mendigutía et al., 2015a).

Another consequence of magnetic fields around YSOs could be launching via X-winds (Shu et al., 1994). Due to the interaction between the magnetic field and the circumstellar disk, the

field lines that penetrate the disk could wind-up once you get beyond the co-rotation radius (where the rotation rate of the star equals the Keplerian rotation of the disk). As the field lines wind-up, magnetic surfaces would form and charged particles from the stellar wind would be trapped and launched as collimated outflows.

Disk winds are similar in nature to the X-wind, but arise from further out in the disk. If the magnetic field threads the disk, some of the disk material could be centrifugally accelerated and launched along open field lines (Blandford & Payne, 1982).

1.2.2 Molecular Emission

The clouds that form stars are made up primarily of molecular hydrogen (H_2). As the cloud collapses into the central star, some of the molecular gas that is not part of the initial in-fall will form a circumstellar disk. One would expect that the best method of observing the circumstellar disk would be the detection of H_2 emission, however, H_2 is difficult to observe directly. H_2 lacks a permanent dipole moment, meaning H_2 must radiate via a quadrupole transition, and the Einstein A coefficient for quadrupole transitions are 10^7 times weaker than the allowed dipole transitions. H_2 has been observed in the disks around T Tauri stars in both the IR (Beck et al., 2008) and UV (Herczeg et al., 2004), while only upper limits have been determined for HAeBe stars (Carmona et al., 2008; Martin-Zaïdi et al., 2008a, 2010). The current interpretation of the origins of the H_2 emission from T Tauri stars is that it arises from hot gas located interior to the CO emitting regions of ($0.1 <$ a ≤ 2 AU for H_2 vs. a ≥ 2 AU for CO; France et al. 2012, 2014). H_2 has been observed in absorption around HAeBe stars, however, indicating that the emission could be the product of photoevaporative winds in the outer disk or an envelope of gas that is the remnant of the molecular cloud from which the star was born (Martin-Zaïdi et al., 2008b). Since the most abundant molecule proves difficult to observe, we look at other molecules: CO, OH, and H_2O.

1.2.2.1 Carbon Monoxide

CO has a similar binding energy to that of H_2, allowing it to survive even in some harsh environments (CO has a binding energy of 11.1 eV which allows the molecule to self-shield in UV radiation fields). Studies of molecular clouds indicate that CO is $\sim 10^{-4}$ times less abundant than H_2. The primary reason that CO is more readily observed in circumstellar disks is due to the permanent electric dipole moment. The rotational energy levels are also more closely spaced than those of H_2.

Rotational transitions for CO show up at longer wavelengths in the radio regime. Ro-vibrational transitions are observed in the NIR regime. The $\nu = 1 \rightarrow 0$ fundamental band peaks at 4.30 μm, while the first overtone ($\nu = 2 \rightarrow 0$) emission peaks at 2.29 μm. For CO, only transitions with $\Delta J = J' - J'' = \pm 1$, with J' corresponding to the upper state and J'' denoting the lower state, can occur (no dipole transitions for the $\Delta J = 0$, Q-branch). The $\Delta J = -1$ (R-branch) increase until the minimum wavelength then pile-up to form bandheads where emission lines overlap, while the $\Delta J = +1$ (P-branch) increase in separation as you advance through higher vibrational levels.

CO was first observed around a YSO by Mould et al. (1978), and first reported in T Tauri and HAeBe systems by Carr (1989) and Thi et al. (2001), respectively. CO has been used as a diagnostic for the dynamics of circumstellar disks. Pontoppidan et al. (2011) combined spectro-astrometry (see Chapter 2) with CO observations to conclude that the CO emission likely originates from a combination of gas in Keplarian orbit in the disk and a disk wind. Banzatti & Pontoppidan (2015) decomposed fundamental CO emission features into both broad and narrow components to illustrate how the two probe different regions of the circumstellar disk (broad components originate from the hot inner disk at $\sim$0.05 au while the narrow component probes the colder outer regions of the terrestrial planet forming regions, out to about 10 au).

1.2.2.2 Hydroxyl

OH is less abundant in the interstellar medium than H_2 by a factor of $\sim 10^{-7}$. Like CO, it has a permanent electric dipole. However, OH differs from CO due to the presence of an unpaired electron. This unpaired electron leads to splitting among individual rotational levels in the molecule. The spin of the unpaired electron can either align with the spin of the internuclear spin axis, or lie orthogonal to it. This produces a slight energy difference that is known as Λ-Doubling (Figure 1.4). Additionally, the $^2\Pi$ ground state of OH can be further split if the spins of the unpaired electron and the hydrogen nucleus are parallel or antiparallel. This slight energy difference produces magnetic hyperfine splitting that can be observed in radio wavelengths starting at 18 cm (or 1612 MHz). When OH is observed in the circumstellar environments of YSOs, each feature has a + state and − state. This will reduce the strength of emission features by a factor of four in comparison to CO, assuming the same temperature and abundances.

OH was first detected in HAeBe stars by Mandell et al. (2008). Since then, studies have shown that OH appears in about 50% of HAeBes (Brittain et al., 2016, and references therein).
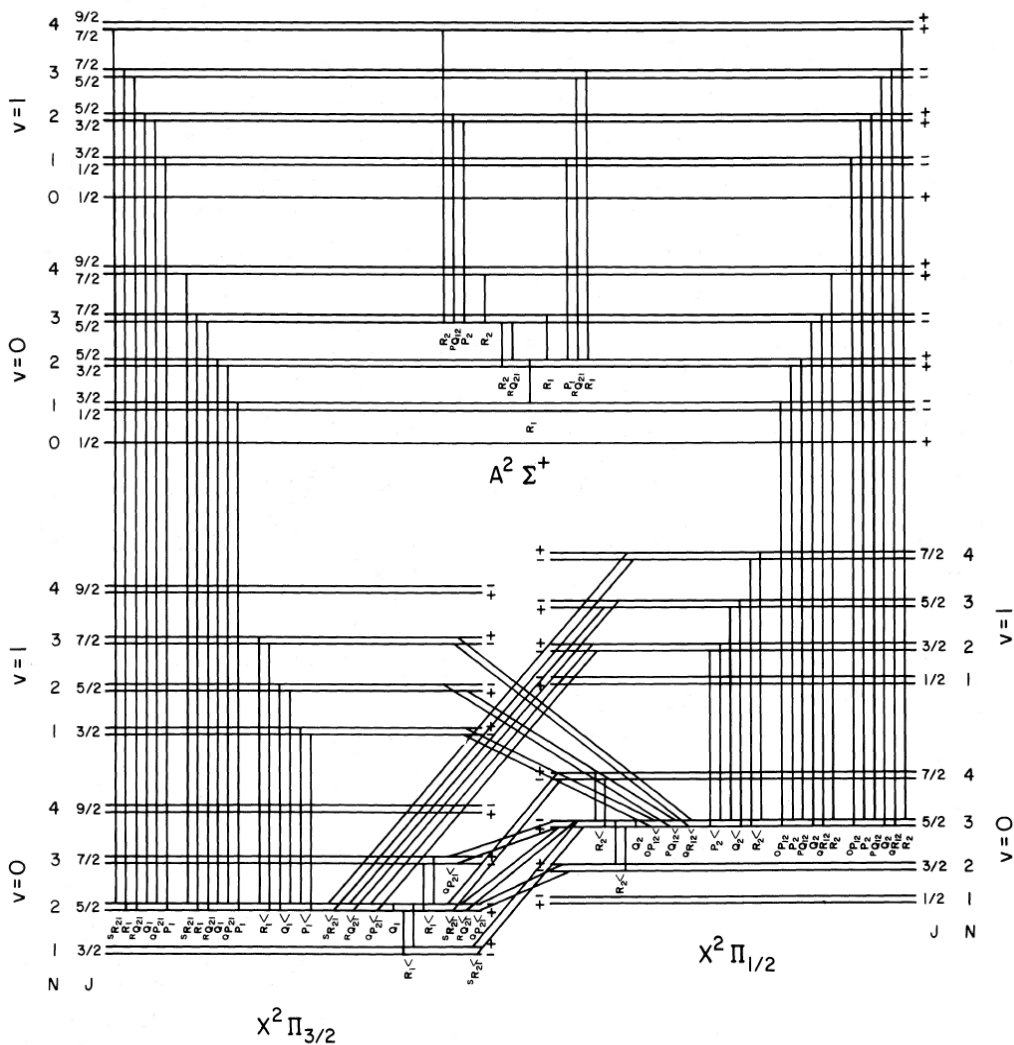
Figure 1.4: Energy level diagram for the ground state ($X^2\Pi$) and first excited state ($A^2\Sigma^+$) for the OH molecule. The $X^2\Pi$ is split due to Λ-doubling. Hyperfine splitting is not shown. Notation for the energy levels is as follows: J denotes the total angular momentum quantum number, N denotes the rotational quantum number, and ν denotes the vibrational quantum number. Figure from Schleicher & Ahearn (1982).

The prevailing theory of OH production in circumstellar disks around HAeBe stars is either in situ formation (see Equation 1.12) or via photodissociation of H_2O

$$H_2O + h\nu \rightarrow OH + H. \tag{1.10}$$

1.2.2.3   Water

H_2O is comprised of the first (H) and third (O) most abundant elements in the universe, so it would seem logical that it should be one of the more abundant molecules. However, in observing molecular clouds, that is not the case. In order to understand why, we must look at the various formation mechanisms for H_2O: radiative association, neutral-neutral reactions, ion-neutral reactions, and dust grain surface chemistry. Molecular clouds have densities and temperatures that are below that required for H_2O formation via radiative association and neutral-neutral reaction pathways. When observing these regions, H_2O is typically observed in shocked regions that are denser and more energetic. Ion-ion reactions require large reservoirs of ions in the environment, thus regions near massive stars (with strong X-Ray and UV radiation fields) would provide the best formation locations. H_2O has been observed in the solid phase in some regions suggesting that the formation via dust grain surface chemistry is the most efficient formation pathway for interstellar H_2O. The solid state H_2O observed approaches an abundance of $\sim 10^{-4}$ relative to H_2, similar to that of interstellar CO ratios.

As the molecular cloud collapses and the material not included in the formation of the central star forms the circumstellar disk, the density increases. This allows for temperatures (T $\geq$ 300 K) which are conducive to neutral-neutral H_2O formation to occur (Fedele et al., 2011). The pathway for H_2O formation to occur is as follows:

$$H + H + dust \rightarrow H_2 + dust \tag{1.11}$$

$$O + H_2 \rightarrow OH + H \tag{1.12}$$

$$OH + H_2 \rightarrow H_2O + H. \tag{1.13}$$

H$_2$O

Para   Ortho

Energy E/hc (cm^{-1})

Energy E/k_B (K)

Angular Momentum J
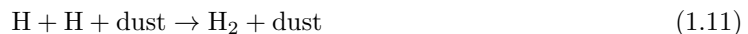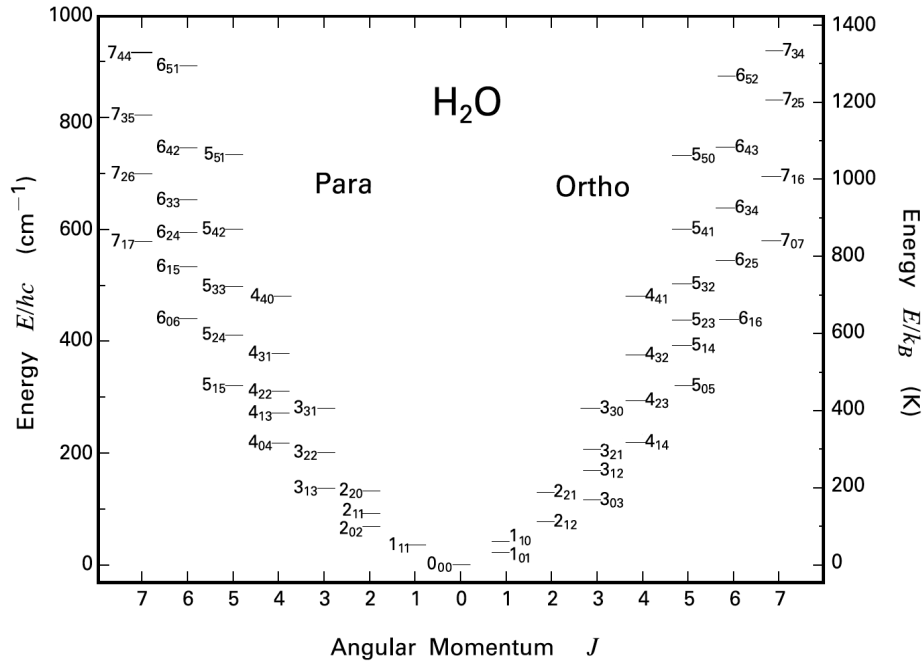
Figure 1.5: Rotational energy levels for a H$_2$O molecule. The "ortho" and "para" designations are in reference to the spin orientation of the two hydrogen atoms in the molecule. If the spins are both even (or odd) they are para-rotational states, while if one spin is even while the other odd, the rotational state is an ortho-rotational state. Figure adapted from Stahler & Palla (2005).

If the hydrogen in the disk is primarily in the form of atomic H rather than H$_2$, then radiative association reactions can occur:

$$H + O \rightarrow OH + h\nu \tag{1.14}$$

$$OH + H \rightarrow H_2O + h\nu. \tag{1.15}$$

H$_2$O is an asymmetric top molecule. This means that H$_2$O molecules have unequal moments of inertia along their principle axis. This provides additional rotational levels compared to CO and OH, thus making the spectrum of H$_2$O more complicated than those molecules. The asymmetry makes it such that the energy level transitions of H$_2$O cannot be expressed as analytical functions. Numerical means are required to determine the individual transition properties.

Another complication in observing H$_2$O in YSOs is the fact that Earth's atmosphere contains large amounts of it. The IR has large bands of absorption from H$_2$O in the atmosphere so any transitions that correspond with these bands will not be observable using ground based instruments.

H_2O plays a vital role in the evolution of circumstellar disks and terrestrial planet forming regions. It has a high freezing point which allows it to freeze out in the disk closer to the central star. When molecules freeze out in circumstellar disks, this leads to pressure bumps which helps facilitate pebble growth and could lead to the formation of planets. Since the H_2O snowline would be closer to the star, it could lead to terrestrial planet formation. Due to the UV absorbing properties of H_2O molecules, it could also shield organic molecules forming deeper in the disk.

Models indicate that H_2O should be produced in the circumstellar environments of HAeBe stars (Walsh et al., 2015), however, the detection of it around HAeBe stars has proven difficult. Some MIR and FIR emission features have been reported for regions in the outer disk, however, NIR H_2O vapor coming from the terrestrial planet forming region in the inner disk has only been found in three sources: HD 101412 (see Chapter 3), HD 104237, and HD 163296 (see Chapter 5). The prevailing theories behind the lacking H_2O detections are (1) that the harsh UV radiation fields of HAeBe stars photodissociate the H_2O into OH, which accounts for the increased detections of OH around HAeBe stars or (2) the H_2O emission from other HAeBes is simply not bright enough to be observed above the IR continuum from the circumstellar material.

Chapter 2

Methods

2.1 Near-Infrared Spectroscopy

Infrared spectroscopy is a key tool in the investigation of the molecular make-up of the cirucumstellar environment around Herbig Ae/Be stars. This is due to the fact that the energy levels corresponding to rotational and vibrational transitions within molecules lie in the near-infrared (NIR) wavelength regime (1 - 5 μm). There are also prominent hydrogen recombination lines present in the NIR used in the study of HAeBes (e.g., Brγ, Paβ).

In order to study all these features, multiple instruments are employed. Each one has its strengths and weaknesses. High-resolution spectrographs are used to study emission features in order to understand the conditions in which the emission lines are formed. Integral field spectrographs with medium resolution, coupled with a technique known as specto-astrometry, are used to unravel the origins of hydrogen emission features. Further insights are garnered when coupling modeling with observations.

2.1.1 High Resolution NIR Spectroscopy

High resolution NIR spectroscopy is generally defined when the spectral resolution, $\lambda/\delta\lambda \geq 10^5$. This resolution is achievable via ground based instruments, however, they have large spatial requirements to contain the optics and equipment. Space based instrumentation is limited in their spectral resolution due to the size requirements to achieve the high resolution observations. The
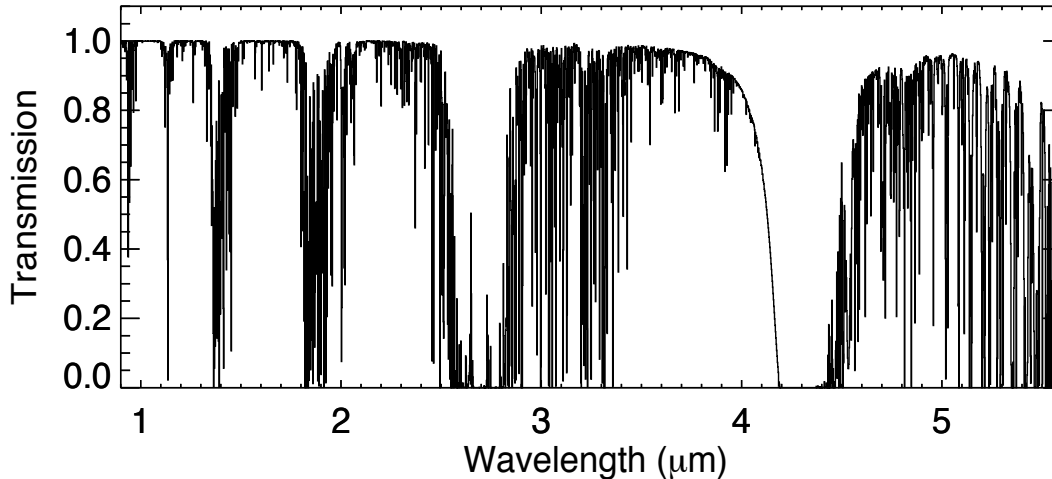
Figure 2.1: Transmittance spectrum of Earth's atmosphere in the NIR (0.9 - 5.5 μm). Data is taken from the ATRAN model (Lord, 1992).

atmosphere allows a majority of infrared radiation through, excluding some regions between 1 and 2 μm due to atmospheric H_2O, and near 3 μm due to CO_2. The atmosphere becomes opaque beyond about 5.5 μm due to H_2O forcing mid-infrared observations to space based missions. Figure 2.1 provides the atmospheric transmittance as a function of wavelength in the infrared regime.

In order to maximize efficiency when taking observations, the high resolution NIR spectrographs are coupled with large aperture telescopes. The state-of-the-art instruments for high resolution NIR spectroscopy are typically housed on 2 - 8 m class telescopes. These telescopes allow for high signal-to-noise (S/N) observations to be made in an efficient amount of time (S/N $\approx$ 200 can be achieved in $\sim$ 60 minutes on an 8-m class telescope for a source with K-band magnitude of 7.5). This study takes advantage of three instruments in particular: CRIRES, Phoenix, and NIFS. Figure 2.2 plots the atmospheric transmittance of the wavelength regions covered by each instrument. The following sections detail each instrument individually.

Flat and dark images are taken in conjunction with observations for calibration. Flats are taken in order to determine the response of the CCD detector when fully illuminated. Flats can either be taken at twilight when the sky is still bright or by illuminating a screen in the dome of the telescope. Dark files are taken with the shutter closed on the CCD detector in order to determine the noise due to the instrumentation. Dark files are exposures which are of the same integration time as the data files.

14
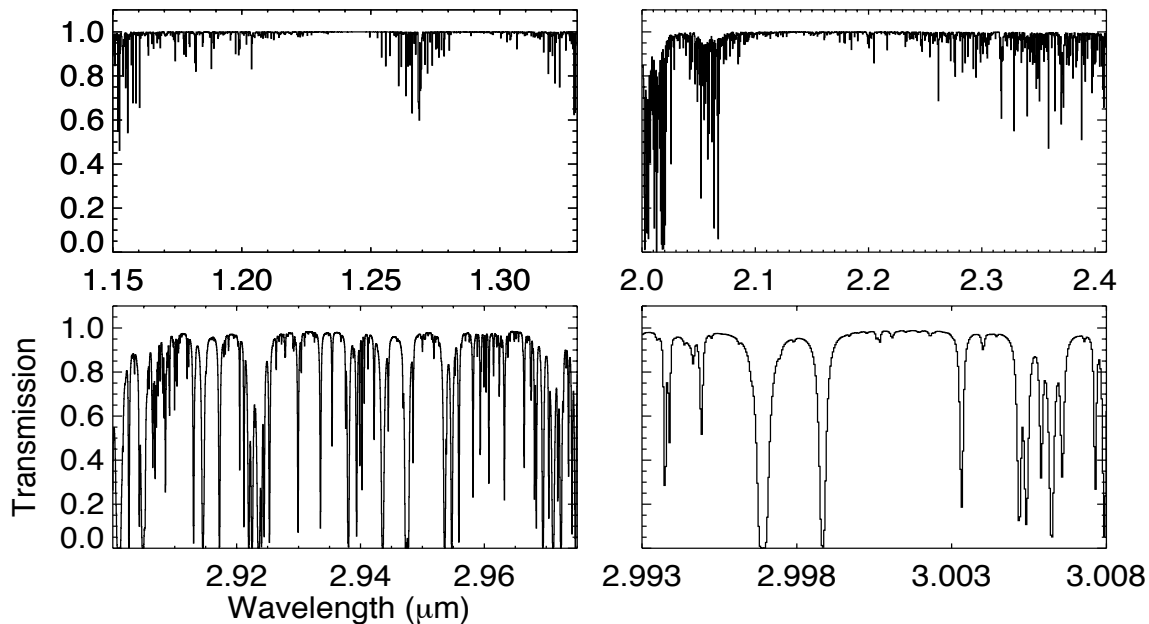
Figure 2.2: Transmittance spectrum of Earth's atmosphere for NIFS (top; J-band left, K-band right), CRIRES (bottom left), and Phoenix (bottom right). Each region is based on observations discussed in future chapters. Data is taken from the ATRAN model (Lord, 1992).

Emission from different molecules in the atmosphere must also be corrected. Sky emission in the NIR evolves on short timescales and distances. In order to correct for this emission, observations are made in a nodding pattern. The first observation is made with the source near the center of the detector. This is called the A position. Next, the telescope is nodded $\sim$10.$''$ and two more observations are made. This is called the B position. Finally, the telescope is moved back to the original A position for the final exposure for one set of observations. In total, four exposures make up one set of $ABBA$ observations. The images are then combined as such: $(A - B - B + A)$.

The reason the images are taken in and $ABBA$ pattern versus an $ABAB$ is due to the time dependence of the sky emission. If the sky emission, s_o, were constant, then the order in which the nods were combined would not matter.

$$ABAB : s_o - s_o + s_o - s_o = 0 \tag{2.1}$$

$$ABBA : s_o - s_o - s_o + s_o = 0 \tag{2.2}$$

15

However, since the sky changes with time, the time derivative of the sky emission must be taken into consideration.

$$s(t) = s_o + \frac{ds}{dt} * t \tag{2.3}$$

$$\Delta s = \frac{ds}{dt} * \Delta t \tag{2.4}$$

Now, the order in which the images are combined changes the sky removal.

$$ABAB : s_o - (s_o + \Delta s) + (s_o + 2\Delta s) - (s_o + 3\Delta s) = -2\Delta s \tag{2.5}$$

$$ABBA : s_o - (s_o + \Delta s) - (s_o + 2\Delta s) + (s_o + 3\Delta s) = 0 \tag{2.6}$$

This method is only good for removing first order sky variations.

Wavelength calibration for NIR spectroscopic data is performed using a spectral synthesis program (SSP; Kunde & Maguire 1974) in order to model the Earth's atmospheric absorption features in the wavelength range being investigated. The model spectrum is then compared to both the standard star and science star spectrum. The absorption features are then aligned giving the dispersion for the observations. Telluric features are removed via ratioing the standard and science star.

2.1.1.1 CRIRES

The *CRyogenic high-resolution InfraRed Echelle Spectrograph* (CRIRES; Käufl et al. 2004) is a high resolution ($\lambda/\delta\lambda = 10^5$) echelle spectrograph used on the *Very Large Telescope* (VLT) unit telescope #1 (UT1). The VLT UT1 is an 8 meter class telescope located at Cerro Paranal in Chile, and is operated by the European Southern Observatory (ESO). CRIRES offers high resolution spectroscopy for wavelengths between 1 and 5 μm, which is optimal for observing rotational-vibrational transitions in molecules. Certain atomic transitions are also available in this regime. The CCD used with CRIRES is a mosaic of four chips which gives a pixel grid of 4096×512. The output spectrum is not continuous due to the layout of the chips.

2.1.1.2 Phoenix

Phoenix is a cryogenic, high-resolution (R $\sim$ 50,000) echelle spectrograph that covers the NIR region between 1-5 μm (Hinkle et al., 1998). It has been housed at the Gemini South telescope and at Kitt Peak National Observatory on both the 4m Mayall telescope and the 2.1m telescope. The output spectra is single order and the spectral coverage is roughly 5% of the central wavelength being observed. Phoenix uses an Aladdin InSb CCD with a detector array of 1024x1024 pixels. Only a small subset of the detector is illuminated such that resultant data is contained in a 512x1024 pixel array.

2.1.2 Integral Field Spectroscopy

Integral Field Spectroscopy (IFS) allows one to study extended objects using spectroscopy. There are multiple techniques (Figure 2.3) one can employ to achieve this: image slicers, lenslet arrays, and optical fibers. Lenslet arrrays split the input image into different elements. Light from each lenslet is concentrated into a point of light and dispersed by the spectrograph. The dispersed light is tilted with respect to the optical axis such that the spectra from each lenslet does not overlap. This technique suffers from not allowing for very broad wavelength coverage. Optical fiber arrays are similar to lenslet arrays, differing only by the image splitting mechanisms. The image is formed at the openings of a bundle of fibers which then pass the light to the spectrograph. This method does not produce a contiguous sampling of the observing region as fibers are cylindrical. If the fiber array is coupled with a lenslet array (in order to focus the light into each fiber), however, this limitation can be overcome.

The method employed by my research uses the image slicer. Instead of focusing the light using lenslets or fibers, the image is first formed on a segmented mirror. Each "slice" of the mirror will direct light to certain location along the slit. The result will be a continuous line of spectra. Upon reduction of the data, the final product will be able to reconfigure the spectra such that you have a 3D data cube with a 2D image of the sky as a function of wavelength.

2.1.2.1 NIFS

The *Near-infrared Integral Field Spectrograph* (NIFS; McGregor et al. 2003) is an instrument used on the 8.1 m Gemini South telescope on Cerro Pachon in Chile. It is a medium resolution (R
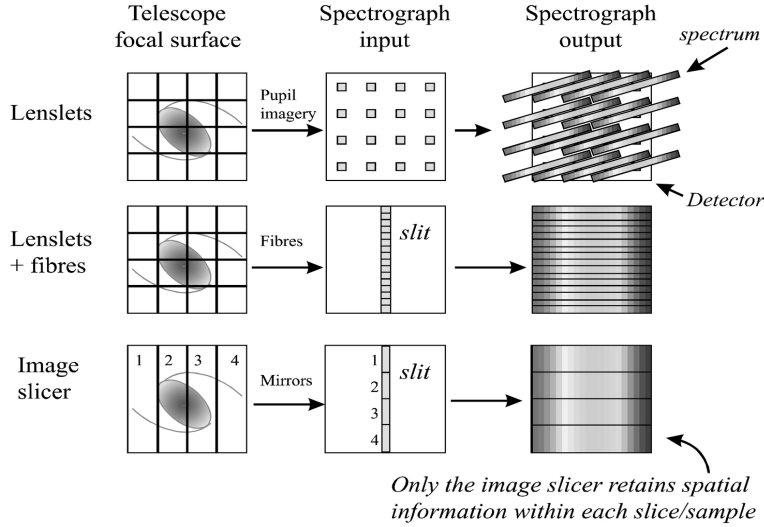
Figure 2.3: Different integral field unit designs. The instrument (NIFS) used for the work in this dissertation uses the image slice design (third row). Figure from Allington-Smith & Content (1998).

~ 5000) integral field unit that provides a spatial resolution of $0.''1$ when the adaptive optics are used during observations. The whole field of view for the instrument amounts to a $3''$ x $3''$ window. The pixels for the CCD have different sampling along and across the image slicer (the pixel scale is $0.''103$ across the slices and $0.''04$ along the slices). Each "spaxel" (or spatial pixel) will thus have an associated spectra giving an array of 29 x 69 (or 2001) individual spectra across the 2D image. NIFS uses a 2048x2048 pixel Rockwell HAWAII-2 detector.

2.1.3 Spectro-astrometry

Spectro-astrometry (SA) is a technique that combines spectroscopy and astrometry, as the name suggests. It measures the center of light as a function of the wavelength to determine if spectral features are offset from the location of the continuum emission in the source (Bailey, 1998b). The first step is to take a traditional spectroscopic observation of your source, and then reduce the data in the usual fashion (flat field, dark correct, wavelength calibrate, etc.). After that step is finished, you can extract the point spread function (PSF) from each wavelength channel in the spectrum. Once the PSF is extracted, it is fitted with a Gaussian function to extract the location of the peak of the PSF (other funtions, such as a Lorentzian or Moffat, can be used if the PSF profile better matches these functional forms). The peak location of the PSF can be determined at a higher precision (Equation 2.7; Whelan & Garcia 2008) than the typical spatial resolution (Equation 2.8)

of the telescope used to take the observations.

$$\sigma_{\text{centroid}} = \frac{\text{FWHM}}{2.3548 \cdot \text{SNR}} \tag{2.7}$$

$$\Delta\theta \geq \frac{\lambda}{4\pi \cdot \text{D}} \tag{2.8}$$

For reference, telescopes with a diameter of 8-meters are typically used for high resolution NIR spectroscopic studies and can achieve a signal-to-noise ratio of $\sim$200 and a seeing (FWHM) of $\sim 1''$. Assuming observations are made near 2 μm, these values give a diffraction limit of $\Delta\theta \geq 0.''06$, or about 60 mas. The accuracy to which the PSF centroid can be determined from these parameters is $\sim$10 mas. Use of adaptive optics in conjunction with SA can get the FWHM down to $0.''1$ dropping the centroiding accuracy to 0.2 mas. Previously, SA has been used to detect binary star systems (Bailey, 1998a; Takami et al., 2003) and trace jets/outflows from YSOs (Takami et al., 2003; Whelan et al., 2004; Brannigan et al., 2006).

SA does have some issues, however. Artifacts can add spurious SA offsets during the data analysis (Brannigan et al., 2006; Whelan & Garcia, 2008). Instrumental effects, such as misalignment of the spectrum with CCD columns, if the CCD pixels deviate from a regular grid, or imperfect flat-fielding or charge transfer deficiencies in the CCD can lead to false SA signals (Bailey, 1998a). These artifacts can typically be removed by taking observations at anti-parallel slit position angles. This will result in real SA signals changing sign, but false signals will remain unchanged. A simple subtraction of one position angel from the other will remove the spurious signals.

Systematic effects pose a slightly more complicated issue. Telescope tracking issues or unstable adaptive optics can also cause spurious SA signals (Bailey, 1998b) that resemble P Cygni-like profiles. These artifacts can be removed in the same fashion as instrumental effects, however, care must be taken when acquiring the second set of observations such that the systematic effects are similar between exposures. The systematic effect which produces the largest false signal is uneven slit illumination (Maciejewski & Binney, 2001; Brannigan et al., 2006). This is caused when the light from the source is non-uniform across the slit, resulting in a blue/red shifted spectrum. This will distort the PSF throwing off the centroid measurement. This effect is compounded if the slit width of the spectrograph is larger than the seeing for the instrument.

2.2   Modeling

In conjunction with spectroscopy, modeling of the line profiles and flux levels can determine important characteristics of the environment in which the emission is formed.

2.2.1   Line Profiles

Modeling of the emission line profiles can give dynamical information on the location within the disk that the emission forms. When studying the circumstellar disk of HAeBe stars, one of the first assumptions is that the material orbiting the central star is moving with a Keplerian velocity profile,

$$v = \sqrt{\frac{GM_*}{r}}. \tag{2.9}$$

When looking at the circumstellar disk on the sky, we can only detect velocity shifts from material moving away or towards the observer. Radiation from materials moving towards the observer will be blue-shifted (shorter wavelengths), while radiation receding from the observer will be red-shifted (longer wavelengths). Thus, in order to observe the motions of circumstellar disks, they must be inclined with respect to the plane of the sky, i.e., if the circumstellar disk is face-on, no velocity shift will be observed and it would be impossible to determine dynamics from emission lines.

The general idea of this scenario is presented in Figure 2.4. Each colored bin represents a region of the disk moving at the same velocity. The emission from these iso-velocity bins will all show up with the same red- or blue-shifted wavelength in the spectrum. The flux received from each contour will depend on the emitting area: the bigger the contour, the more radiation it emits. If the gas is confined to a small area in the disk, the line profile will appear as a double peaked profile since the low velocity bins would not be present to fill in the central region. Low spectral resolutions can mask the double peaked structure

2.2.2   Slab Models

Determining line of sight column densities and temperatures is also achievable via modeling. The simplest method is to assume that the emission arises from gas residing in a slab with constant temperature, column density, and number density. The slab is also assumed to be in chemical and Local Thermodynamic Equilibrium (LTE). By varying the temperature and column density of the
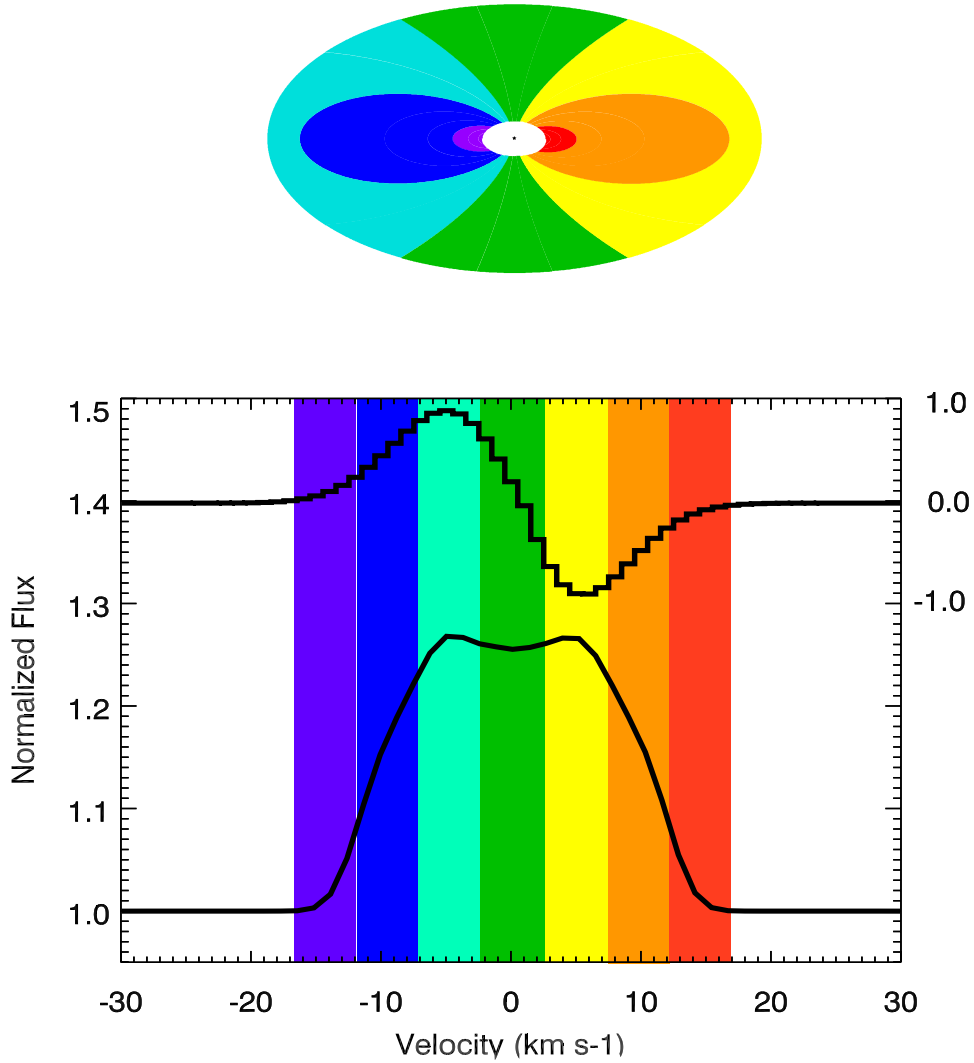
Figure 2.4: Simulation of an emission line profile from a Keplerian disk. Iso-velocity contours are different colors, with corresponding flux bins highlighted below in the same color. The plot above the line profile is the expected SA offsets measured in the center of light as a result of the iso-velocity contours of the disk.

slab, the flux will change. In order to uniquely determine conditions for molecular species, it is important to know the relative strengths of the emission lines from different transitions. This will remove the degeneracy between the temperature and column density.

Chapter 3

Water and OH emission from the inner disk of a Herbig Ae/Be star[1]

3.1 Introduction

High-resolution spectroscopic studies of Herbig Ae/Be (HAeBe) stars indicate that their circumstellar environments are commonly home to hot CO (Blake & Boogert, 2004; Brittain et al., 2007; Salyk et al., 2011b,a; Brown et al., 2013; Banzatti & Pontoppidan, 2015; van der Plas et al., 2015) and, less frequently, OH gas (Mandell et al., 2008; Fedele et al., 2011; Brittain et al., 2016), but they have yet to yield a detection of the H_2O emission from 2 to 4 μm that has been observed in lower-mass pre-main-sequence T Tauri systems (Carr et al., 2004; Salyk et al., 2008; Doppmann et al., 2011; Fedele et al., 2011; Mandell et al., 2012; Banzatti et al., 2017).

Likewise, mid- and far-infrared studies have yielded few detections of H_2O emission from cooler gas in disks around HAeBes. In a study of 25 HAeBes using *Spitzer*, there were marginal detections of H_2O emission reported for 12 of 25 systems (Pontoppidan et al., 2010). These detections were reported based on inspection by eye and were not determined to be above the 3.5σ detection threshold defined in the study. In contrast, similar surveys of T Tauri stars yield a much higher detection rate for H_2O emission in the mid-infrared (22 of 48 exhibited a significant detection of H_2O emission; Pontoppidan et al. 2010). Statistics compiled by Banzatti et al. (2017) showed that

---

[1]Accepted for publication to the Astrophyscial Journal; Adams, S. C. et al. 2019, ApJ, 871, 173

between 63% and 85% out of 64 stars with a stellar mass less than 1.5 $M_\odot$ exhibit mid-infrared H_2O emission. In searches for H_2O in the far-infrared, only 3 sources were detected out of 25 HAeBes observed (Fedele et al., 2012, 2013; Meeus et al., 2012). These results suggests that the abundance of H_2O gas in the optically thin upper atmosphere around HAeBes is low.

One possible explanation for the dearth of near-infrared (NIR) water detections among HAeBes compared to T Tauri stars is that the high far-ultraviolet (FUV) luminosity of HAeBe stars causes a larger column of water to be dissociated to produce OH (e.g., Ádámkovics et al. 2016; Najita & Ádámkovics 2017). As the water falls below the dust photosphere, emission from the water becomes impossible to detect. Here we report what appears to be an exception to this picture - the first detection of NIR H_2O emission from the HAeBe star HD 101412.

HD 101412 is a B9.5Ve star (Valenti et al., 2003) located at a distance of 411^{+5}_{-4} pc (Gaia Collaboration et al., 2016, 2018). As part of an X-Shooter survey of 92 HAeBes, Fairlamb et al. (2015) determined the stellar parameters of their sample self-consistently. They find that $T_{eff} = 9750 \pm 250$ K and $\log(L/L_\odot) = 1.36 \pm 0.23$ adopting d = 301 pc. We adopt the *Gaia* distance and use Siess pre-main-sequence models to recalculate the stellar mass, radius, and luminosity (Siess et al., 2000). The updated values are M = 2.5 $M_\odot$, R = 2.3 $R_\odot$, and $\log(L/L_\odot) = 1.63$.

The inner disk surrounding HD 101412 is nearly edge-on. Fitting a uniform ring model to N-band visibilities acquired with MID-Infrared Interferometric instrument (MIDI) on the Very Large Telescope (VLT) indicates that the disk is inclined $80° \pm 7°$ (Fedele et al., 2008). No (sub)mm observations have been made of this source so there is no observational estimate of the extent or mass of the disk. The mid-infrared spectral energy distribution (SED) of the star indicates that it is a self-shadowed disk (Group II; Fedele et al. 2008). Fairlamb et al. (2017) report the flux of $H\alpha$ for this source and provide a relationship between the accretion luminosity and the luminosity of the $H\alpha$ line. Adopting the stellar parameters above, we find that the accretion rate is 1.6×10^{-7} $M_\odot$ yr^{-1}. The accretion rate indicates that HD 101412 still harbors a large gaseous reservoir.

The disk of HD 101412 reveals a rich molecular spectrum. Both the rovibrational CO overtone (Cowley et al., 2012; Ilee et al., 2014; van der Plas et al., 2015) and fundamental (van der Plas et al., 2015) emission lines have been observed. Modeling of the profile of these lines indicates that the emitting region is narrow (0.8-1.2 au; van der Plas et al. 2015). Mid-infrared spectroscopy also reveals CO_2 emission from the disk of HD 101412 (Pontoppidan et al., 2010; Salyk et al., 2011b). CO_2 emission and CO bandheads of the first overtone emission are both unusual features to observe

Star	Date	Airmass	Exposures	Int. Time (s)
L band				
HD 101412	2013 May 27	1.265	20	3600
λ Cen	2013 May 27	1.277	8	240
K band				
HD 101412	2011 Apr 05	1.250	8	4800
j Cen	2011 Apr 05	1.301	8	640

Table 3.1: Observation information for HD 101412 OH, H_2O, and CO data presented. All data were obtained using the ESO Data Archives.

in the spectrum of HAeBe stars. Only 7% show CO overtone bandhead emission in a survey of 91 HAeBes (Ilee et al., 2014) and only 4% show CO_2 emission in a survey of 25 HAeBes (Salyk et al., 2011b). Here we report the detection of rovibrational OH and H_2O emission from this source as well (Sections 3.2 and 3.3). We apply slab models of CO, OH, and H_2O to compare the emitting radii, temperature, and column densities of these molecules (Section 3.4) and to compare the molecular emission observed in HD 101412 to other young stellar objects (Section 3.5). Finally, we discuss the implications for our understanding of the molecular content of the inner disks around HAeBe stars (Section 3.6).

3.2 Observations

L-band observations of HD 101412 were obtained from the European Southern Observatory (ESO) Data Archives along with the associated raw calibration files, based on observations under program ID 091.C-0796(A). The data were acquired on 2013 May 27 using a 0.″2 slit width at a central wavelength of 2.94 μm using the Cryogenic Infrared Echelle Spectrograph (CRIRES; Käufl et al. 2004) on the ESO VLT UT1. CRIRES has four detectors that each cover $\sim$0.0160 μm with a $\sim$0.0045 μm gap between each chip. Exposures were taken in an *ABBA* nod pattern with a 10.″ nod in order to remove sky emission lines. An integration time of 60 s and 3 sub-integrations were used for each of the 20 exposures, giving a total integration time of 3600 s. Table 3.1 gives details of all observations used in this study.

Data reduction was performed using software based on algorithms developed for the reduction of Phoenix and Near-InfraRed echelle SPECtrograph (NIRSPEC) data (described in Brittain et al. 2007). Flats and darks were taken in order to remove systematic variation in the pixel gain. Se-

quential AB observations were combined (A - B) and then divided by the normalized flat field image. Median values of the combined images were used to identify and remove hot and bad pixels, as well as cosmic-ray hits. Pixel values that differ by 6σ were rejected. Spectra were then extracted using a rectangular extraction method. Wavelength calibration was performed using the telluric absorption features observed in the spectrum. A Sky Synthesis Program (SSP) model atmosphere (Kunde & Maguire, 1974), which accesses the 2003 HIgh-resolution TRANsmission (HITRAN) molecular absorption database (Rothman et al., 2003), was computed based on the airmass of the observations. Standard star observations of λ Cen were taken immediately after the observations of HD 101412. The telluric standard was reduced following the same process as HD 101412. The normalized spectrum of HD 101412 was divided by the normalized spectrum of λ Cen to correct for atmospheric absorption lines. Regions of the spectrum where the atmospheric transmittance was below 50% were excluded. Final reduced L-band spectra and ratios are presented in Figure 3.1.

We also reduced archival data for the CO bandhead emission previously reported for HD 101412 (Cowley et al., 2012; Ilee et al., 2014). The data were obtained based on observations made with CRIRES on the VLT under program ID 087.C-0124(A). The CO data were re-reduced using the same method as the OH and H_2O observations. The CO data were then modeled in order to determine self-consistently the CO-emitting region, temperature, and column density.

The flux densities adopted for the continua of the K- and L-band spectra were obtained using values from Johnson:K and Johnson:L filter photometry measurements found using the VizieR Photometry Viewer (Ochsenbein et al., 2000). The flux density at 2.94 μm was estimated at a value between the flux density at these filters by a linear fit to the two data points. A continuum flux of 3.20×10^{-10} erg s^{-1} cm^{-2} μm^{-1} was used for the L band (OH), and 4.21×10^{-10} erg s^{-1} cm^{-2} μm^{-1} was used for the K band (CO).

3.3   Results

The fully reduced L-band spectrum has a spectral resolution of R $\approx$ 90,000 and a signal-to-noise ratio of $\sim$200. We detect the OH P4.5 and OH P5.5 doublets with the peak in the normalized line flux relative to the continuum of 9% (Figure 3.2, panel (A) and (C), respectively). Gaps in the profile of the P5.5 doublet are due to telluric absorption greater than 50%. We also detect H_2O emission near 2.93 μm (Figure 3.4). Another H_2O feature between 2.9074 and 2.9110 μm is also

26
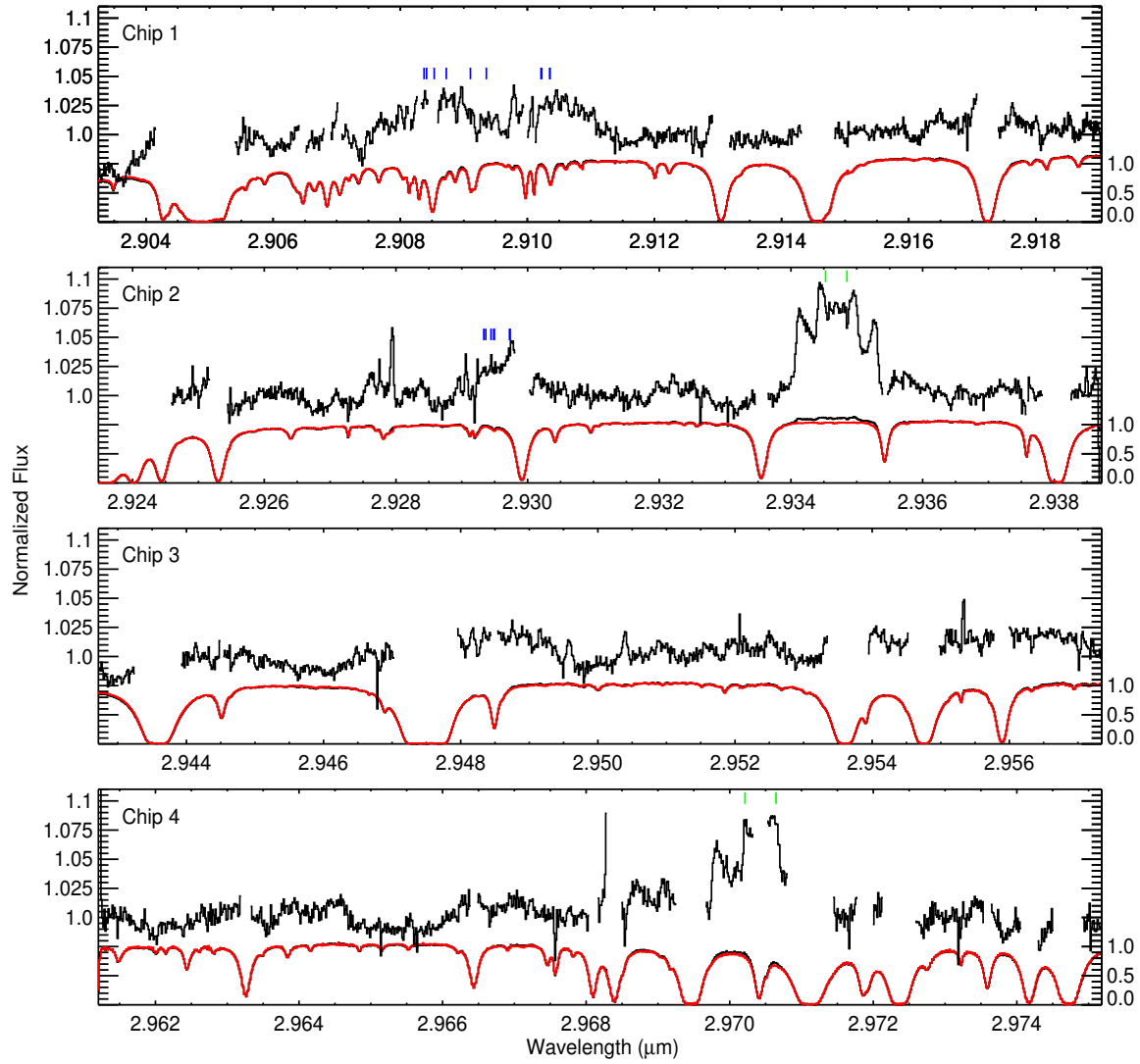
Figure 3.1: *L*-band observations of HD 101412. Chip 1 is the upper plot and chip 4 is the lower plot, with the gap between each plot resulting from the gaps between the chips. In each panel we plot the normalized spectrum of HD 101412 (black) and the telluric standard λ Cen (HR 4467) (red). The telluric corrected spectrum of HD 101412 is plotted above (stretched by a factor of 20 and offset by 0.5 units). The left axis shows the normalized flux units scaled to the ratioed spectrum while the right axis shows the normalized flux units for the science and standard star spectra. The locations of the OH emission doublets are marked with green hashes with the structure observed in the continuum coming from H_2O emission, with the strongest H_2O features marked with blue hashes.

Wavelength (μm)	Transition	A_{ul} (s^{-1})	g_u	E_u (K)
OH Lines				
2.97040	3/2 P5.5f	12.67	20	5627.64
2.96997	3/2 P5.5e	12.67	20	5626.56
2.93461	3/2 P4.5f	11.68	16	5414.92
2.93428	3/2 P4.5e	11.68	16	5414.31
H$_2$O Lines				
2.92949	$10_{\ 8\ 2} \rightarrow 11_{\ 8\ 3}$	18.45	63	8540.39
2.92948	$10_{\ 8\ 3} \rightarrow 11_{\ 8\ 4}$	21.20	21	8540.39
2.92925	$11_{\ 5\ 6} \rightarrow 12_{\ 5\ 7}$	39.56	23	8221.99
2.92924	$14_{\ 2\ 13} \rightarrow 15_{\ 2\ 14}$	48.79	29	8697.67
2.92920	$14_{\ 1\ 13} \rightarrow 15_{\ 1\ 14}$	48.58	87	8697.71
2.92912	$13_{\ 3\ 11} \rightarrow 14_{\ 3\ 12}$	48.45	81	8583.04
2.92909	$13_{\ 2\ 11} \rightarrow 14_{\ 2\ 12}$	48.94	27	8582.23
2.91011	$13_{\ 2\ 12} \rightarrow 14_{\ 2\ 13}$	48.78	81	8293.46
2.91011	$13_{\ 1\ 11} \rightarrow 14_{\ 1\ 12}$	48.91	27	8293.43
2.90998	$12_{\ 2\ 10} \rightarrow 13_{\ 2\ 11}$	49.17	75	8177.10
2.90997	$12_{\ 3\ 10} \rightarrow 13_{\ 3\ 11}$	48.16	25	8178.82
2.90911	$10_{\ 6\ 4} \rightarrow 11_{\ 6\ 5}$	31.81	63	8030.62
2.90886	$11_{\ 3\ 8} \rightarrow 12_{\ 3\ 9}$	53.09	23	7976.11
2.90848	$10_{\ 6\ 5} \rightarrow 11_{\ 6\ 6}$	31.57	21	8029.60
2.90829	$11_{\ 4\ 8} \rightarrow 12_{\ 4\ 9}$	42.70	69	8004.54
2.90817	$14_{\ 1\ 14} \rightarrow 15_{\ 1\ 15}$	48.52	29	8340.48
2.90813	$14_{\ 0\ 14} \rightarrow 15_{\ 0\ 15}$	48.04	81	8340.56

Table 3.2: Parameters for some transitions that comprise observed emission features in HD 101412 L-band observations. Line groups are presented in the order that the emission feature is discussed in the text. All data were acquired using the HITRAN database (Rothman et al., 2013).

observed (Figure 3.5). Table 3.2 gives transition parameters for the individual transitions that we propose comprise the most prominent emission features. Errors for equivalent widths (EWs) are determined by adding the noise across each pixel in the emission feature in quadrature.

3.3.1 OH Emission

The P4.5 doublet transition is spectrally resolved; however, the doublet itself is blended. The emission feature is bracketed by strong telluric absorption features. The EW is calculated over the entire range of the doublet between the absorption features and divided by 2 due to the blending. The EW is $4.3 \pm 0.2 \times 10^{-5}$ μm that, when factoring in the distance and L-band flux density, corresponds to a line luminosity of $7.2 \pm 0.3 \times 10^{-5}$ L$_\odot$. The line to continuum contrast of the P4.5 OH doublet is 9% (Figure 3.2), which is more than three times the line to continuum contrast typically observed for this doublet in previous observations of HAeBes (Mandell et al., 2008;
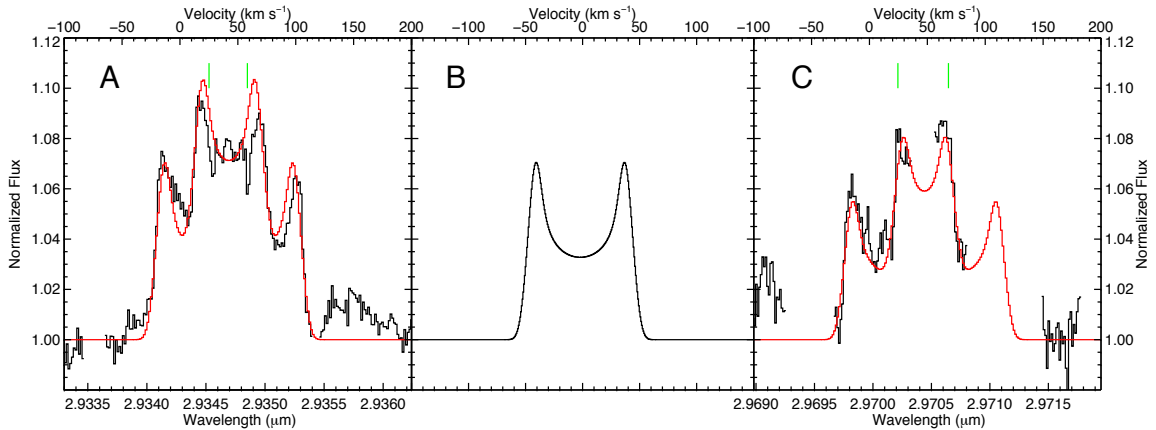
Figure 3.2: (A) P4.5 (1+, 1−) OH emission doublet. The normalized fluxes of the OH doublets are plotted vs. wavelength. The upper x-axis shows the relative velocity of the emission features. The zero velocity is centered at the laboratory rest wavelength of the P4.5 (1+) line (2.93428 μm). The green tick marks indicate the wavelength of each doublet feature in the rest frame of the star. The Doppler shift inferred from the molecular emission indicates that the heliocentric radial velocity is 16.9 km s^{-1}, which is consistent with the heliocentric radial velocity inferred from the measurement of photospheric lines (16.5 km s^{-1}; Hubrig et al. 2010). The best-fit model is plotted in red. (B) Model line profile of each doublet feature, scaled to match the P4.5 intensity. (C) P5.5 (1+, 1−) OH emission feature. The emission feature is partially obscured by telluric absorption. The green tick marks indicate the location of each doublet feature in the rest frame of the star. The zero velocity bin is centered at 2.96997 μm, which is the laboratory rest wavelength of the P5.5 (1+) lines.

Fedele et al., 2011; Brittain et al., 2016).

The P5.5 emission feature is partially obscured by atmospheric absorption. The profile of the P5.5 doublet and P4.5 doublet differ slightly in the blue portion due to different separations of the doublet transition energies. Thus, the individual peaks in the blue portion of the P5.5 feature show each doublet's peak as being further apart. This broadens the overall line width; however, the inner peak separation between the blue portion of the (1−) line and red portion of the (1+) line is reduced. Due to the atmospheric absorption, an EW cannot be determined from the data. Based on the model fits obtained from fitting the full P4.5 doublet, we determine the P5.5 EW to be 3.7 ± 0.1 × 10^{-5} μm, which corresponds to a line luminosity of 6.2 ± 0.3 × 10^{-5} L$_{\odot}$.

We observe a Doppler shift of 24.4 km s^{-1}. This implies a heliocentric radial velocity of 16.9 km s^{-1} based on the date the observations were made. Hubrig et al. (2010) observe Fe lines in the spectrum of HD 101412 and report an average heliocentric radial velocity of 16.65 km s^{-1}, which is consistent with our determined radial velocity.
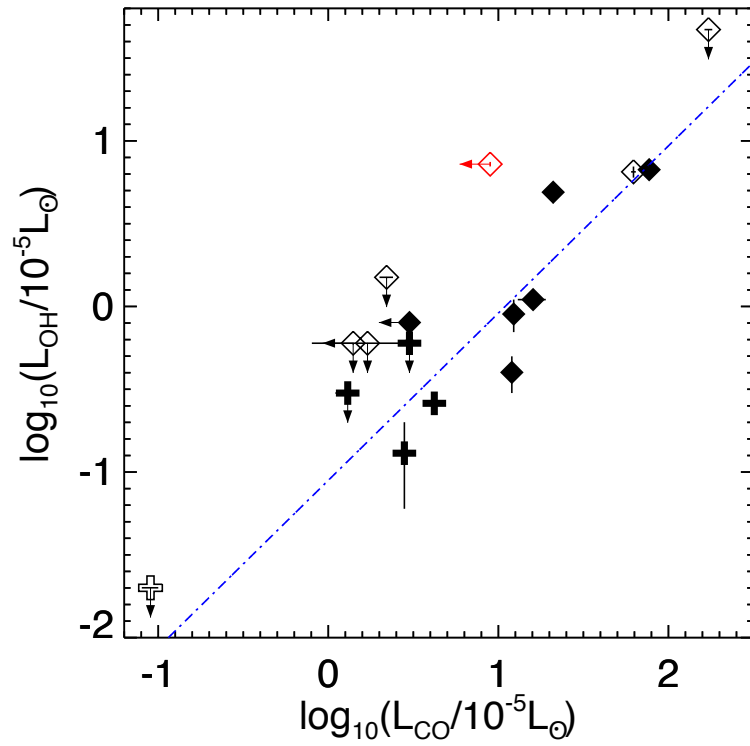
Figure 3.3: Adapted from Brittain et al. (2016). HD 101412 has been added and is plotted in red. Group I HAeBe stars are marked as filled symbols. Group II HAeBe stars are marked as open symbols. The disks that have been observed to have an optically thin inner disk are labeled with "plus" signs. Disks without such optically thin regions are labeled with diamonds. The dotted-dashed line is a linear least-squares fit to the detections, not including HD 101412.

Brittain et al. (2016) find a power-law relationship between the luminosity of rovibrational CO ($\nu = 1 \rightarrow 0$ P30) and OH ($\nu = 1 \rightarrow 0$ P4.5) emission from HAeBes and find that the ratio of their luminosities is 11.0±0.2. We compare the relative luminosity of the OH and CO emission for HD 101412 (Figure 3.3). Because the lines are so broad, there is significant line blending. We take the most isolated CO line ($\nu = 1 \rightarrow 0$ P26 transition; Troutman 2010) and determine the luminosity of the P30 line, assuming the gas is 1300 K (see section 3.4). Because of the line blending, we take the CO luminosity to be an upper limit and find that L(CO)/L(OH) $\leq$ 1.24. Thus the relative flux of the OH emission is an order of magnitude larger than the previous HAeBes studied.

3.3.2   H$_2$O Emission

One prominent H$_2$O emission feature is observed at 2.929 μm (Figure 3.4). This feature is partially obscured by telluric absorption. The emission is due to a blend of multiple transitions. Table 3.2 presents some transitions that comprise the emission feature.

Another H$_2$O emission feature is observed between 2.9074 and 2.9110 μm (Figure 3.5), with some regions obscured by atmospheric absorption. This feature is also a blend of multiple transitions. In both instances, the H$_2$O transitions observed all require high temperatures to reach the upper levels, thus making it unlikely that the H$_2$O emission observed is residual from telluric correction.

3.3.3   CO Observations

In order to determine self-consistently the column densities of CO, OH, and H$_2$O, we also present K-band observations of HD 101412. We reproduce the results of Cowley et al. (2012) and Ilee et al. (2014) in that we detect both the CO $\nu = 2 \rightarrow 0$ and $\nu = 3 \rightarrow 1$ bandheads. We determine the signal to noise of the chips containing the CO $\nu = 2 \rightarrow 0$ bandhead and isolated emission features (Chips 2 and 3) to be $\sim$290, while Chip 4, containing the $\nu = 3 \rightarrow 1$ bandhead emission, has a signal to noise of $\sim$120. Figure 3.6 shows the isolated CO $\nu = 2 \rightarrow 0$ emission lines (Chip 3), while Figure 3.7 show the CO $\nu = 2 \rightarrow 0$ (left) and $\nu = 3 \rightarrow 1$ (right) bandhead emission. A discussion of the modeling is presented in Section 3.4.
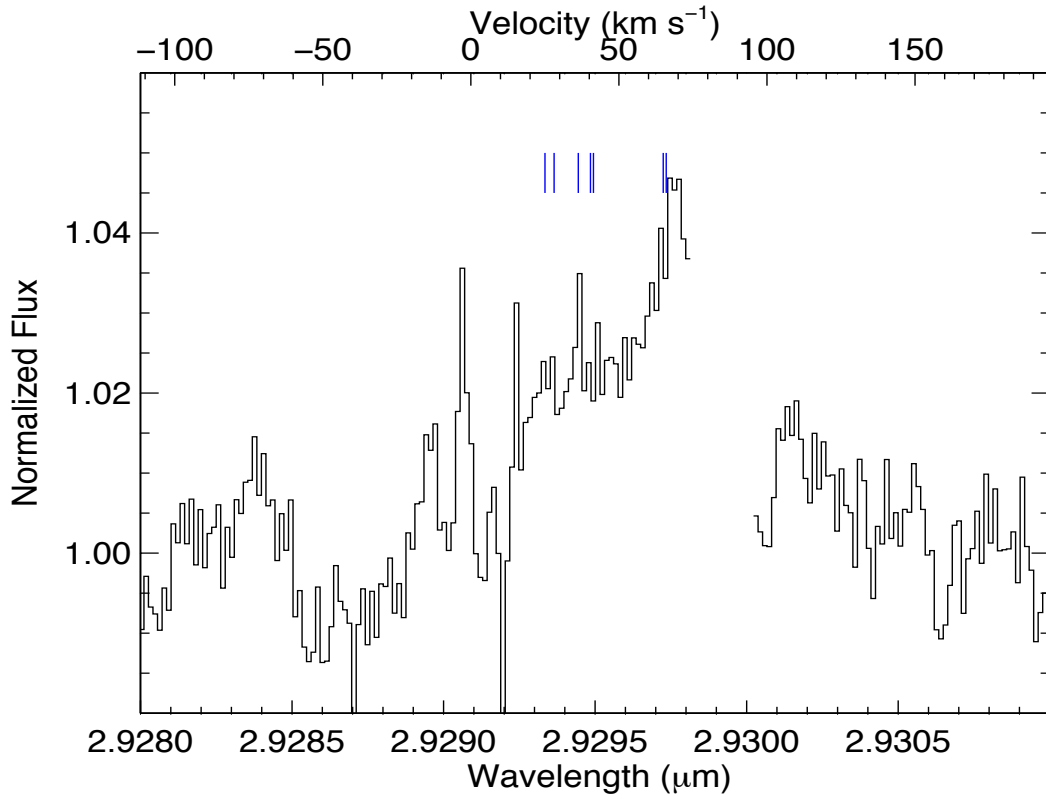
Figure 3.4: The 2.93 μm H_2O emission lines. The blue tick marks indicate the positions of the dominant transitions contributing to the emission feature. The zero velocity bin is centered at 2.92909 μm, the transition with the shortest wavelength of the list in Table 3.2 found in this spectral region. The upper x-axis gives the velocity space information and shows a Doppler shift of 24.4 km s^{-1}, consistent with the OH lines.
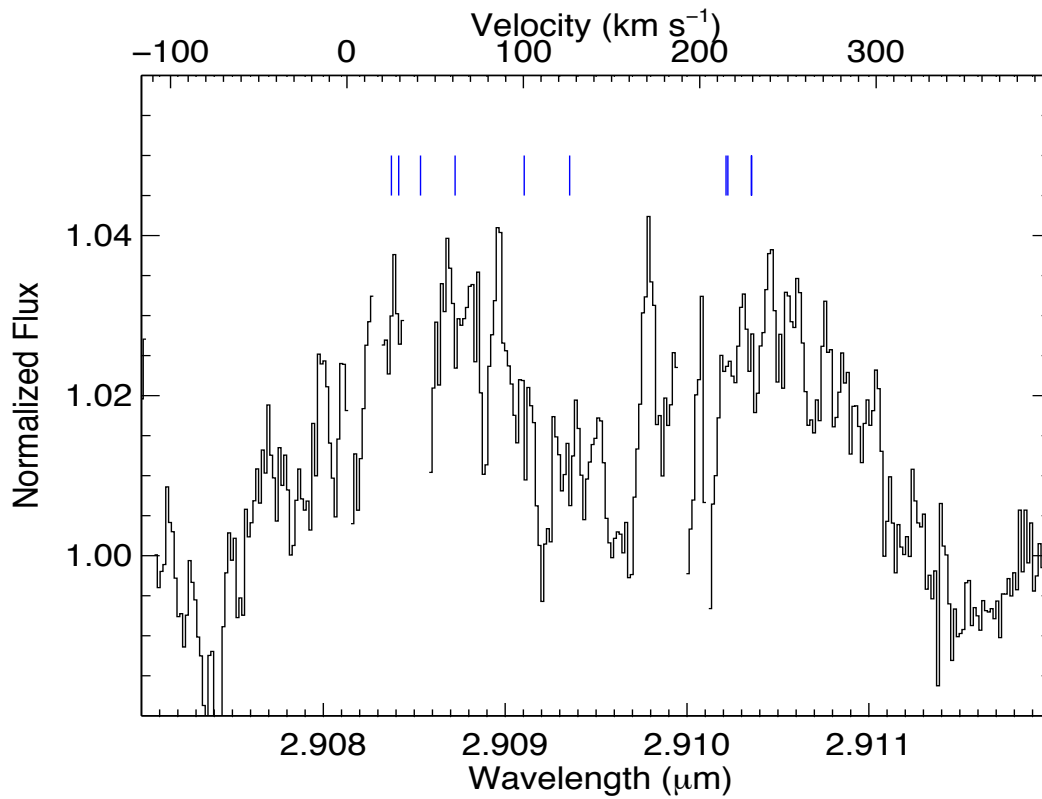
Figure 3.5: The 2.91 μm H_2O emission lines. The blue tick marks indicate the positions of the dominant transitions contributing to the emission feature. The zero velocity bin is centered at 2.90813 μm; the transition with the shortest wavelength of the list in Table 3.2 found in this spectral region. The upper x-axis gives the velocity space information and shows a Doppler shift of 24.4 km s^{-1}. H_2O transition information can be found in Table 3.2.
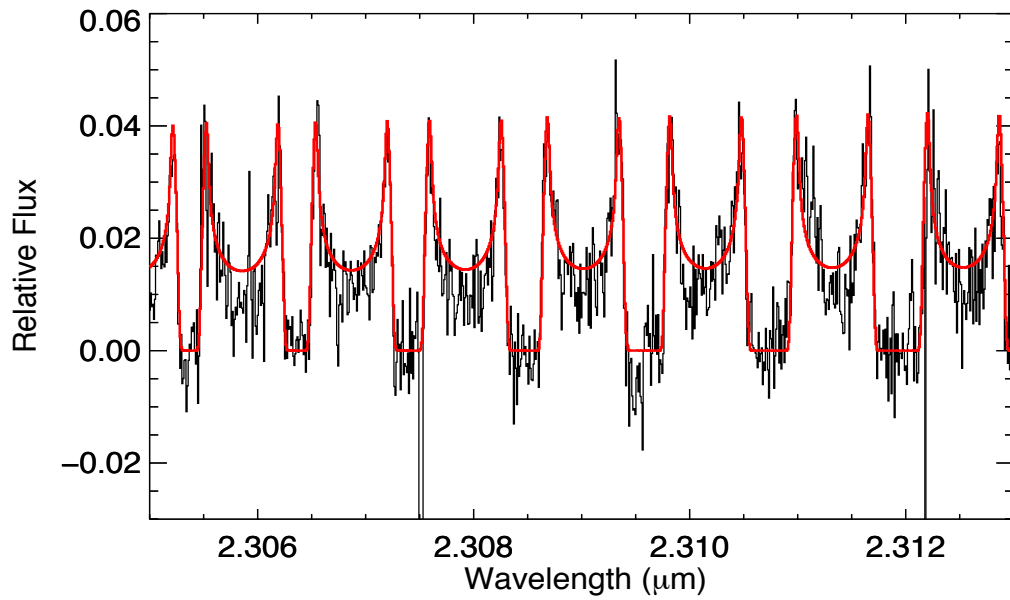
Figure 3.6: Isolated CO $\nu = 2 \rightarrow 0$ emission lines. The best-fit model is plotted in red. Final parameters for the model are T = 1300 K, N(CO) = 7×10^{20} cm^{-2}, with R$_{in}$ = 0.88 and R$_{out}$ = 1.27 AU, and i = 86°.
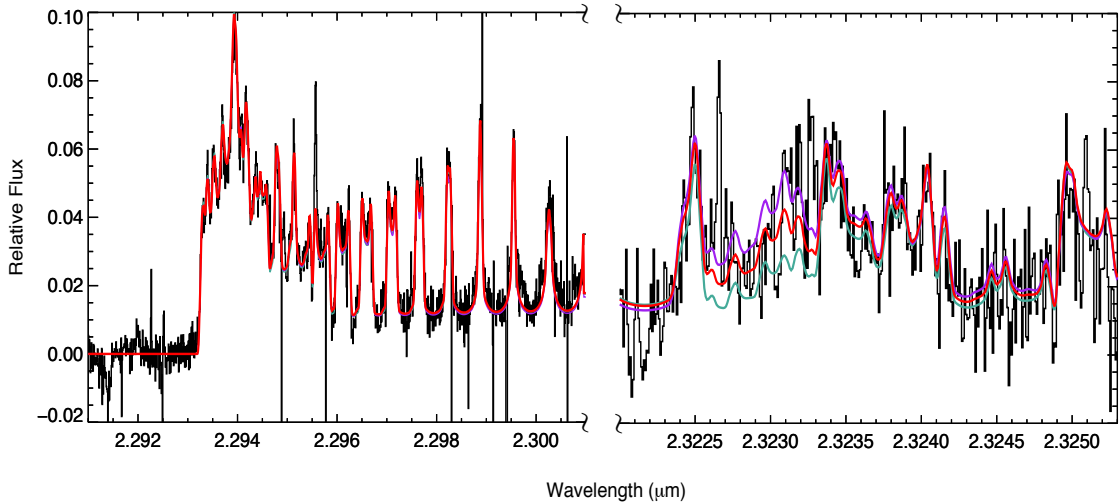
Figure 3.7: CO $\nu = 2 \to 0$ (left) and $3 \to 1$ (right) bandhead emission modeling. The best-fit model is plotted in red. Final parameters for the red model are the same as in Figure 3.6. Data is plotted in black, with the turquoise model indicating a temperature of 1000 K, red has a temperature of 1300 K, and purple has a temperature of 1500 K. The model is most sensitive to the region near 2.323μm.

3.4 Modeling

To determine the spatial location, column density, and temperature of the CO, OH, and H_2O emission, we fit the spectra using a slab model (Carr et al., 2004). The disk models assume Local Thermodynamic Equilibrium (LTE) and Keplerian rotation. Because we find that the emission originates in a fairly narrow annulus, the gas temperature and the column density for each species are taken to be constant over the emitting region.

We start by fitting the velocity profile of the CO $\nu = 2 \to 0$ lines, because the CO spectrum covers the greatest range of energy levels and has the highest signal to noise. The CO lines near 2.31 μm (Figure 3.6) are separated from other lines and give a clean measure of the line profile. A composite profile is formed using the four lines least affected by telluric absorption. A Keplerian disk emission model is fit to the profile using χ^2 minimization, which gives 50.5 km s^{-1} for the projected velocity at the inner radius of the emitting region and 42.1 km s^{-1} at the outer radius (or equivalently, R_{out}/R_{in} = 1.44). A third fit parameter is the exponent of a power law for the radial intensity, $I \propto r^\alpha$; however, the result is insensitive to this parameter, due to the small radial extent

of the emission, and the exponent is set to a fixed value of $\alpha = -2$.

Having set the kinematics of the CO emission, the CO $\nu = 2 \rightarrow 0$ bandhead and isolated lines are fit with a disk emission model. Given the narrow radial extent of the emission, the CO column density, N(CO), and temperature, T, are taken to be constant with radius. The main parameters that determine the bandhead shape and relative line intensities are T and N(CO). If you hold T constant, increasing N(CO) will increase the luminosity of the emission lines. For a given T and N(CO), matching the CO emission flux gives the projected emitting area, which is characterized by the radius of an equivalent circular area. The shape of the bandhead is also affected to a lesser degree by the local line broadening; the local line width was initially set to the CO thermal width. We find that the model fits to the CO $\nu = 2 \rightarrow 0$ bandhead have a large degeneracy between T and N(CO). Acceptable fit temperatures range from 1000 to 2500 K, and we rule out emission for temperatures above 3000 or below 800 K. When the CO $\nu = 3 \rightarrow 1$ bandhead is included in the fit, the relative flux of the $\nu = 3 \rightarrow 1$ and $\nu = 2 \rightarrow 0$ emission restricts the range in T and N(CO), removing the degeneracy from fitting the CO $\nu = 2 \rightarrow 0$ alone (Figure 3.7).

The best-fit parameters for the CO overtone emission are T $= 1300^{+200}_{-300}$ K and N(CO) $= 7.0^{+6.9}_{-1.3} \times 10^{20}$ cm^{-2}, and the projected emitting area, πR_e^2, has a radius of $R_e = 0.156$ au. This model is overplotted in red on the CO $\nu = 2 \rightarrow 0$ and $\nu = 3 \rightarrow 1$ bandheads in Figure 3.7, along with models for higher and lower temperatures.

Once we have the emitting column and projected area, we can break the degeneracy between disk inclination and the radius by finding the inclination that is consistent with both the projected velocity and the projected emitting area. For the above solution, this inclination is i $= 86°$. The inner and outer radii for the CO emission are then $R_{in} = 0.88$ and $R_{out} = 1.27$ au.

We also investigate the impact of nonthermal broadening (turbulence). The thermal width of CO at 1300 K is 1.5 km s^{-1} (FWHM). Different amounts of extra broadening are added to the thermal width and the CO composite profile is refit. Then, the fits to the $\nu = 2 \rightarrow 0$ bandhead are repeated. A change in the local line width alters the overlap of the closely spaced transitions at the bandhead. Because the CO lines are optically thick, the amount of overlap affects the relative distribution of flux with the wavelength and hence the shape of the bandhead. As the turbulence becomes larger, the fit to the shape at the bandhead becomes progressively worse. Based on this, we rule out v_{turb} (FWHM) ≥ 3.5 km s^{-1} (Figure 3.8).

In modeling the OH, we first determine the radial extent of the OH emission by modeling

the profile of the blended OH P4.5 doublet feature, using the same procedure used for the CO profile. Using the same inclination angle (86°) from the CO modeling, the OH emitting region extends from R_{in} = 0.81 to R_{out} = 1.46 au. Figure 3.2, panel (A) shows the model fit to the P4.5 doublet. The model includes nonthermal line broadening (FWHM) of 6.7 km s^{-1}, which improves the appearance of the fit at the peaks of the OH emission; however, the statistical significance versus thermal broadening is small, and its inclusion does not change the derived radii for the emission. The same best fit velocity profile is consistent with the P5.5 emission feature, as shown in Figure 3.2, panel (C).

The OH and CO emission originate from similar radii, but the radial extent (and area) of the OH emission is somewhat larger than that found for the CO emission. Given that the CO and OH spectra were obtained 2 yr apart, it is not clear whether the OH and CO line profiles point to an intrinsic difference in their respective radial distributions or reflect the variability of the emitting size.

In order to derive a column density for the OH emission, we adopt the temperature of 1300 K found for CO, since the the OH features give no constraint on the gas temperature. Using the projected area for the OH emission, the column density is adjusted to match the flux in the OH P4.5 doublet. We find that N(OH) = $2.8^{+1.4}_{-0.7} \times 10^{18}$ cm^{-2}, which yields a ratio of N(OH)/N(CO) = $4.0^{+2.3}_{-2.5} \times 10^{-3}$.

Modeling of the H$_2$O emission is more complicated. We originally confirmed our identification of these features as water by comparison to emission from LTE slab models. Due to the lower signal to noise of the H$_2$O emission, we find that it is not possible to determine uniquely the temperature and column density of water from the spectrum, although it is clearly hot, in the range of 1000-3000 K. In addition, the velocity line profile cannot be constrained to the accuracy that is possible for CO and OH. Hence, the OH velocity profile and emitting area are used for H$_2$O, along with the same 1300 K temperature. The column density required to match the H$_2$O flux is N(H$_2$O) = $5.8^{+0.6}_{-0.8} \times 10^{17}$ cm^{-2}. This model is compared to the H$_2$O emission features in Figure 3.4. Other features, outside of those mentioned in Section 3.2, are consistent with the H$_2$O emission model. The adopted parameters are consistent with the relative fluxes and velocity widths in the H$_2$O spectrum. The derived water column density yields ratios of N(H$_2$O)/N(OH) = $0.21^{+0.11}_{-0.06}$ and N(H$_2$O)/N(CO) = $8.3^{+3.0}_{-4.1} \times 10^{-4}$.
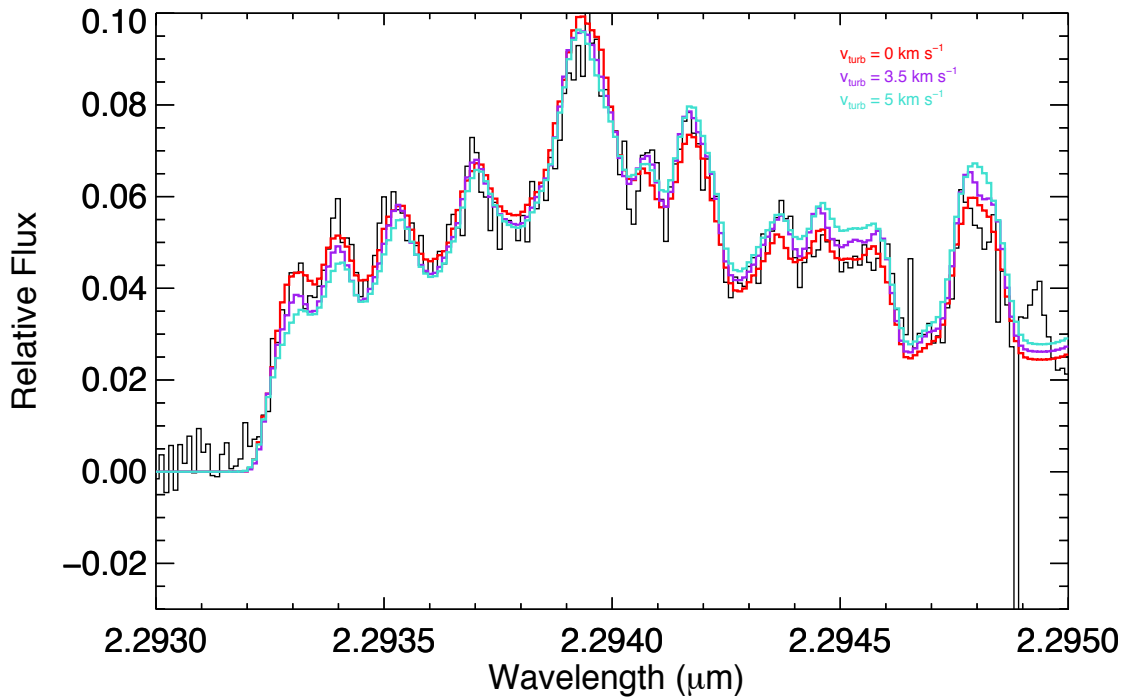
Figure 3.8: Models of the CO $\nu = 2 \rightarrow 0$ bandhead for different levels of turbulent broadening compared to the observed spectrum. The nominal model, with only thermal broadening, is plotted in red. The turquoise model includes an additional broadening (FWHM) of 5.0 km s^{-1}, which corresponds to the total line width of 5.2 km s^{-1} in Ilee et al. (2014). We rule out v_{turb} (FWHM) ≥ 3.5 km s^{-1} (purple plot).
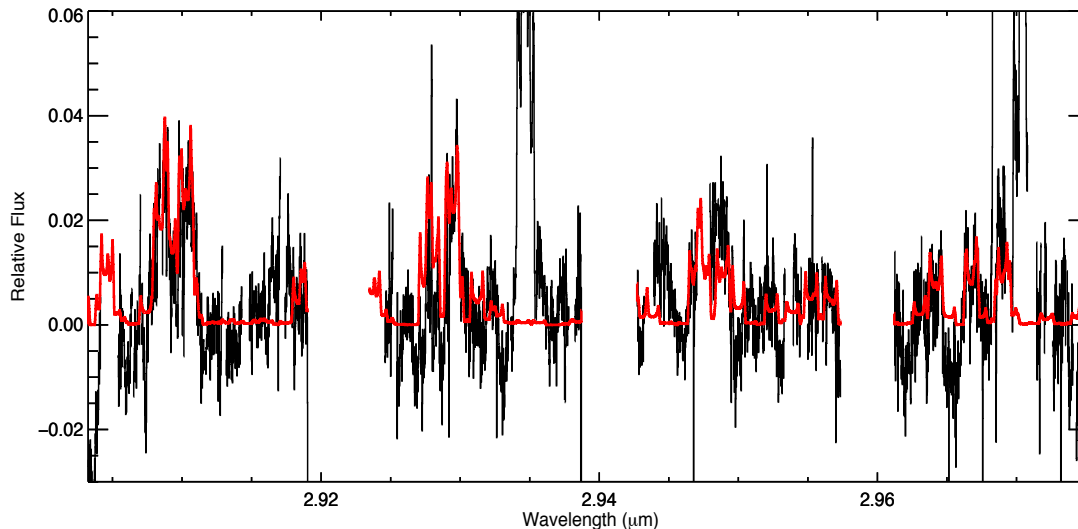
Figure 3.9: Model of observed H_2O emission features. The model uses the same geometry as the best-fit OH P4.5 model: R_{in} = 0.81 au, R_{out} = 1.46 au, and an inclination angle of 86°.

3.5 Comparison to Young Stellar Objects

To contextualize our detection of water in the inner disk around HD 101412, we compare the column densities of CO, OH, and H_2O among seven other young stars for which water has been detected (HD 259431 does not have a detection of NIR water emission, just an upper limit on the water column density; Table 3.3). SVS 13 is a $\geq$ 3 $M_\odot$ (Hirota et al., 2008) young stellar object on the Class 0/Class I boundary (Chen et al., 2009) from which the CO $\nu = 2 \rightarrow 0$ bandhead and H_2O emission lines near 2.2935 μm have been observed (Carr et al., 2004). AS 205A, DR Tau, and RU Lup are all classical T Taruri stars (CTTS; spectral type K0, K5, and G5, respectively) around which CO, OH, and H_2O emission has been observed (Salyk et al., 2008; Mandell et al., 2012). V1331 Cyg is a 2.8 $M_\odot$ intermediate mass T Tauri star (IMTTS; spectral type G7-K0; Petrov et al. 2014). Doppmann et al. (2011) observed OH and H_2O emission in the L band from this star. 08576nr292 is a massive young stellar object (MYSO; $\sim$6 $M_\odot$ B5 star) from which H_2O and CO bandhead emission have also been detected (Thi & Bik, 2005).

For four of the sources (HD 101412, SVS 13, V1331 Cyg, and 08576nr292) in Table 3.3, the CO column density is comparable (0.7-6 $\times$ 10^{21} molecules cm^{-1}). Three other sources (AS 205A, DR Tau, and HD 259431) have much lower CO column densities reported, ranging from 0.6 to 1.6

Star	SpT	$M_\star$ $(M_\odot)$	Class	$N(CO)$ (cm^{-2})	$N(OH)$ (cm^{-2})	$N(H_2O)$ (cm^{-2})	$N(OH)/N(CO)$	$N(H_2O)/N(CO)$
SVS 13(1)	–	3.0	Class 0/1	1.2×10^{21}	–	1.8×10^{21}	–	1.5
DR Tau(2)	K5	0.8	CTTS	7.0×10^{18}	2.0×10^{17}	8.0×10^{17}	2.9×10^{-2}	1.1×10^{-1}
AS 205A(2)	K0	1.2	CTTS	6.0×10^{18}	2.0×10^{17}	6.0×10^{17}	3.3×10^{-2}	1.0×10^{-1}
V1331 Cyg(3)	G7-K0	2.8	IMTTS	6.0×10^{21}	1.0×10^{20}	2.0×10^{21}	2.0×10^{-2}	3.0×10^{-1}
RU Lup(4)	G5	0.7	CTTS	–	–	–	$1.6 - 3.3 \times 10^{-2}$	5.5×10^{-2}
HD 101412	B9.5	2.5	HBe	$7.0^{+6.9}_{-1.3} \times 10^{20}$	$2.8^{+1.4}_{-0.7} \times 10^{18}$	$5.8^{+0.6}_{-0.8} \times 10^{17}$	$4.0^{+2.3}_{-2.5} \times 10^{-3}$	$8.3^{+3.0}_{-4.1} \times 10^{-4}$
08576nr292(5)	B5	6.0	MYSO	3.9×10^{21}	–	2.5×10^{18}	$\sim 1.0 \times 10^{-3}$	6.4×10^{-4}
HD 259431(6),(7)	B5	6.6	HBe	1.6×10^{19}	7.9×10^{15}	$<3.2 \times 10^{14}$	4.9×10^{-4}	$<2.0 \times 10^{-5}$

Table 3.3: Comparison of molecular column densities from previously reported observations of young stellar objects. Thi & Bik (2005) did not observe OH emission in 08576nr292. N(OH)/N(CO) for 08576nr292 is based off chemical models. (1) Carr et al. (2004); (2) Salyk et al. (2008); (3) Doppmann et al. (2011); (4) Mandell et al. (2012); (5) Thi & Bik (2005); (6) Ilee et al. (2014); (7) Fedele et al. (2011):.

$\times 10^{19}$ molecules cm^{-1} (RU Lup only has column density ratios reported in Mandell et al. 2012). However, even with the range in column densities, the ratios between molecules show similar trends when comparing similar sources. Lower-mass T Tauri stars have N(OH)/N(CO) of a 2-3.3 $\times 10^{-2}$ and N(H$_2$O)/N(CO) of 0.6-3.0 $\times 10^{-1}$. As you move to more massive sources, this trend changes. N(OH)/N(CO) is now 0.5-4 $\times 10^{-3}$ and N(H$_2$O)/N(CO) is 0.2-8 $\times 10^{-4}$. The fact that the latest type star is surrounded by the disk with the highest H$_2$O/CO ratio suggests that the UV radiation from the star plays a pivotal role in determining the abundance of water in the atmosphere of the inner disk

In addition to the comparison among a handful of young stars for which water has been detected, we compare a sample of 19 T Tauri and HAeBe stars reported in the literature for which both OH and H$_2$O are measured (Table 4; Fedele et al. 2011; Banzatti et al. 2017). Plotting the OH line luminosity versus the H$_2$O line luminosity, we find that the T Tauri stars follow a linear trend given by Eqn. 3.1, confirming the constant OH/H$_2$O line flux ratios presented in Banzatti et al. (2017):

$$L_{H_2O}/L_\odot = (2.1 \pm 0.1)L_{OH}/L_\odot + (0.09 \pm 0.23). \tag{3.1}$$

Among the sources included in this sample is EX Lupi while it was undergoing an outburst and was in quiescence (Banzatti et al., 2017). The luminosity increases along the fit to the T Tauri data, indicating that the ratio of L$_{H_2O}$ and L$_{OH}$ is relatively constant over a wide range of stellar luminosities. However, it is not clear if the FUV luminosity of the star would impact the emission from the circumstellar disk while undergoing an outburst. During outbursts, the inner disk heats up to the point that the continuum emission from the inner region buries the emission from the star. The outer disk would thus only see emission from the self-luminous inner disk. For example, the FUV spectra of T Tauri stars is more similar to FUors than to the far more FUV luminous HAeBes (Valenti et al., 2000).

While HD 101412 is the only HAeBe in the sample for which both water and OH are detected, upper limits for eight additional sources are available from Fedele et al. (2011). We find that the HAeBes consistently show weaker water luminosity for a given OH luminosity than the T Tauris. This trend is also suggestive that the UV luminosity of the stars plays an important role in determining the relative column density of water.

Star	SpT	$M_\star$ $(M_\odot)$	Class	L_{H_2O} $(10^{-5}\ L_\odot)$	L_{OH} $(10^{-5}\ L_\odot)$
AS 205A	K0	1.2	CTTS	3.76 ± 1.39	1.06 ± 0.39
DF Tau	K5	0.8	CTTS	2.19 ± 0.28	0.79 ± 0.10
DR Tau	M3	0.5	CTTS	3.41 ± 0.52	0.96 ± 0.14
EX Lup08	M0	0.8	CTTS	6.79 ± 2.04	3.03 ± 0.91
EX Lup14	–	–	–	0.25 ± 0.02	0.09 ± 0.01
RU Lup	K7-M0	0.7	CTTS	3.42 ± 0.48	1.28 ± 0.18
S Cra N	G0	0.6	CTTS	6.36 ± 1.97	2.75 ± 0.85
T Tau N	K1.5	2.4	IMTTS	8.28 ± 6.63	3.98 ± 3.18
VW Cha	K7	0.6	CTTS	2.39 ± 0.13	1.52 ± 0.08
VZ Cha	K7	0.8	CTTS	0.85 ± 0.01	0.35 ± 0.01
BF Ori	A5	1.4	HAe	<0.16	<0.16
HD 34282	A0	1.9	HAe	<0.20	<0.20
HD 76534	B2	11.4	HBe	<1.51	<1.51
HD 85567	B5	6	HBe	<3.32	33.19 ± 9.96
HD 98922	B9	5.2	HBe	<0.40	<0.40
HD 101412	B9.5	2.5	HBe	3.96 ± 0.30	7.18 ± 0.25
HD 250550	B7	3.6	HBe	<1.06	2.23 ± 0.16
HD 259431	B5	6.6	HBe	<0.55	23.86 ± 3.29
UX Ori	A3	2.1	HAe	<0.33	<0.33
V380 Ori	A1	2.8	HAe	<1.13	6.31 ± 3.75

Table 3.4: Luminosity values from the literature used in Figure 3.10. T Tauri flux values are obtained from Banzatti et al. (2017), and HAeBe flux values and upper limits are from Fedele et al. (2011). HD 101412 flux values are from this work. Flux values are converted to luminosities using distances obtained from Gaia Collaboration et al. (2016). Upper limits have been converted to 1σ limits for consistency.

3.6 Discussion

The infrared molecular emission from HD 101412 is unusual in several respects. Firstly, we see the CO bandhead emission arising from a narrow annulus. To populate the CO bandheads, the gas must be hot (T$\gtrsim$2000 K) and dense ($n_H \gtrsim 10^{10}$ cm^2; Najita et al. 1996). The requisite conditions are ordinarily only met in systems with high accretion rates ($\sim 10^{-7} - 10^{-6}$ M$_\odot$yr^{-1}; Ilee et al. 2014). CO bandhead emission is rarely observed in HAeBe systems, with a detection rate of 7% (Ilee et al., 2014).

In order to detect the large columns of CO gas observed in emission, all CO bandhead sources require strong suppression of the K-band opacity in the CO-emitting region. For HD 101412, the CO column density inferred from overtone bandhead emission (7×10^{20} cm^{-2}; Table 3.3) corresponds to $N_H = 1.4 \times 10^{25}$ cm^{-2}, assuming a CO/H$_2$ of 1×10^{-4} or an $A_K = 600$ if the dust were interstellar. Detecting a CO column as large as 7×10^{20} cm^{-2}, therefore, requires a reduction in the K-band
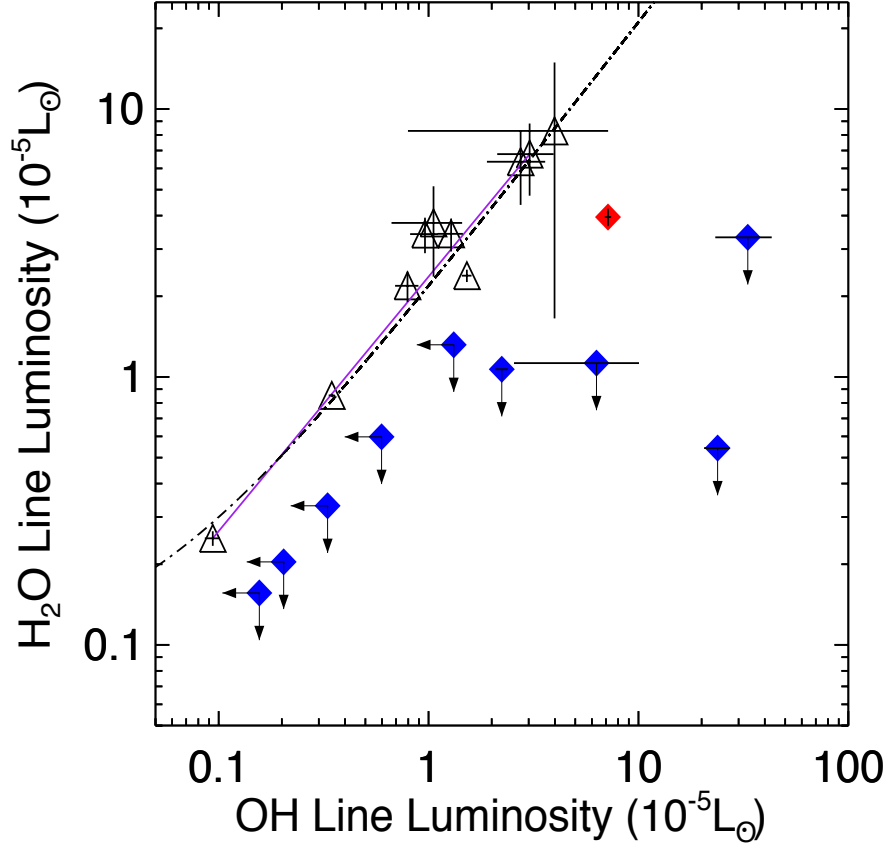
Figure 3.10: Comparison of the H_2O line luminosity to the OH line luminosity taken from the literature (Fedele et al., 2011; Banzatti et al., 2017) for T Tauri and HAeBe stars. T Tauri stars are plotted as open black triangles, HAeBe stars as blue diamonds, and HD 101412 as a red diamond. The black line is a weighted linear least-squares fit to the T Tauri data. We do not plot T Tauri sources with upper limits from Banzatti et al. (2017), only T Tauris with detections of both water and OH at 2.9 μm. We only plot the HAe/Be sources with OH detections or upper limits and water upper limits for 2.9 μm from Fedele et al. (2011), and we have converted HAeBe upper limits to 1σ levels for consistency. The purple line connects EX Lup observations from 2008 and 2014. The 2008 observation occurred during an accretion outburst, resulting in higher OH and H_2O fluxes. The luminosity of the water emission from the T Tauri stars is consistently larger than the upper limits placed on HAeBe stars.
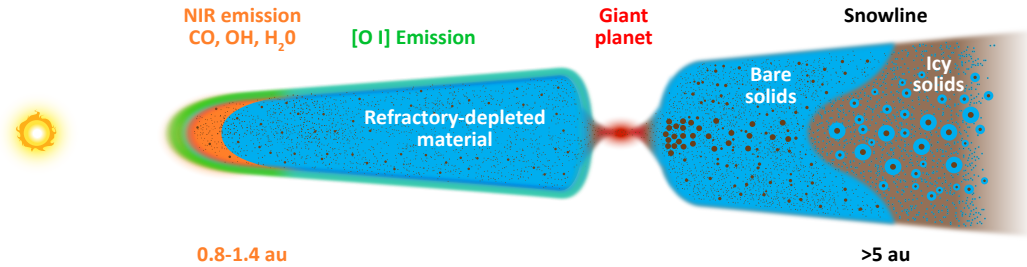
Figure 3.11: Above schematic presents one possible scenario, discussed in detail in the text, to explain the NIR observations of HD 101412. Based on the stellar luminosity for HD 101412, we determine the dust sublimation radius to be at 0.25 au. The molecular emission arises from a narrow annulus (∼0.8-1.4 au). Refractory elements are observed to be below solar abundances based on photospheric observations, while C and O are found to be at solar abundances (Folsom et al., 2012). This indicates that large dust grains are filtered out, leading to a depletion of refractory elements in the inner disk. If a planetary body was forming within the snow line (>5 au), this would allow for C- and O-containing molecules to reside in the inner disk, eventually accreting onto the central star, and giving rise to the observed photospheric abundance pattern. This figure is not to scale.

continuum opacity by a factor of ∼600, i.e., a factor of ∼6 larger than the typical factor of ∼100 reduction in grain surface area that is found for T Tauri disks (Furlan et al., 2007).

Ilee et al. (2014) mention that CO emission is primarily observed around B-type stars, which makes sense due to the required temperatures to excite CO bandhead emission. Conditions around lower-mass stars may only reach requisite temperatures during episodic accretion events, thus resulting in variable CO bandhead emission. Also, due to the high gas density required, some disks may lack sufficient material to allow for CO bandhead emission. Ilee et al. (2014) also mention a possible connection to high disk inclinations with CO bandhead emission. Their sources with detections had a range of inclinations from 51° to 72°, based on model fits. A possible explanation for this inclination dependence would be the CO bandhead emission tracing the inner disk wall near the dust sublimation radius.

Secondly, whereas water emission is rare among HAeBe disks (Section 3.1), in HD 101412 we detect hot water emission with a luminosity comparable to the most luminous water emission from T Tauri disks. One possible explanation for the dearth of water emission from HAeBe disks compared to T Tauri disks is the relative UV luminosities to which the circumstellar disks are exposed; the strong FUV field of HAeBe stars can readily dissociate water in their disk atmospheres. This may not be apparent from the Walsh et al. (2015) chemical model of a disk around an HAe star, which finds a water-rich disk atmosphere with water column densities much larger than is consistent with

observations. As they note, one reason for the discrepancy between the observed and predicted water columns may be their assumption of interstellar grains (gas-to-dust ratio and grain size distribution), which limits the penetration depth of the UV photons and their effect on disk molecular abundances.

The T Tauri disk models of Ádámkovics et al. 2014 (their Figure 4; see also Ádámkovics et al. (2016); Najita & Ádámkovics (2017)) support this perspective. Assuming grain growth at the level inferred for observed sources (e.g., Furlan et al. 2007), these models find that increasing the FUV radiation from T Tauri stars does, in fact, push the molecular layer deeper into the disk and dissociates H_2O to produce more extensive OH. Models of HAeBe disks that assume a comparable level of grain growth would likely find a similar reduction in the water column density in the disk atmosphere, which is more consistent with the general lack of water emission detected from HAeBe stars (Figure 3.10). In principle, water emission could be detected in HAeBe disks if the dust opacity in the disk atmosphere was low enough that the dust photosphere was located below the transition from OH to H_2O.

There are reasons to expect a low dust opacity in the inner disk of HD 101412. The stellar photosphere of HD 101412 is strongly depleted in refractory elements (Fe, Mg, Si), but has solar-like abundances of volatile elements (C, N, O), thus HD 101412 is a λ Boö star (Folsom et al., 2012). Kama et al. (2015) hypothesize that the depletion of heavy elements in the photosphere of the star is a consequence of selective accretion of gas relative to dust, which is the accreting material has a gas-to-dust ratio of ∼600, i.e., a reduction in refractories by a factor of ∼ 6, similar to the extra factor of 6 reduction needed in the K-band continuum opacity to expose the entire CO bandhead-emitting column to view.

What is the source of the depletion of refractory material in the disk? If a giant planet (with mass from 0.1 M_J to 10 M_J) is present in the disk, the pressure bumps it creates (e.g., at the edge of a gap) could preferentially reduce the accretion of solids relative to gas through the disk by aerodynamic drag (Rice et al., 2006; Zhu et al., 2012). Due to the lack of a convective outer layer in early-type stars, the refractory depleted material that accretes onto the star would reside on the surface, giving rise to the λ Boö abundance pattern (Figure 3.11).

The detection of C- and O-bearing molecules (CO, OH, and H_2O) from the inner region of the HD 101412 disk and the detection of CO_2 with *Spitzer* (Pontoppidan et al., 2010), which presumably will eventually accrete onto the star, is consistent with the high abundance of volatile elements in the stellar atmosphere of HD 101412. The presence of oxygen-bearing molecules, such
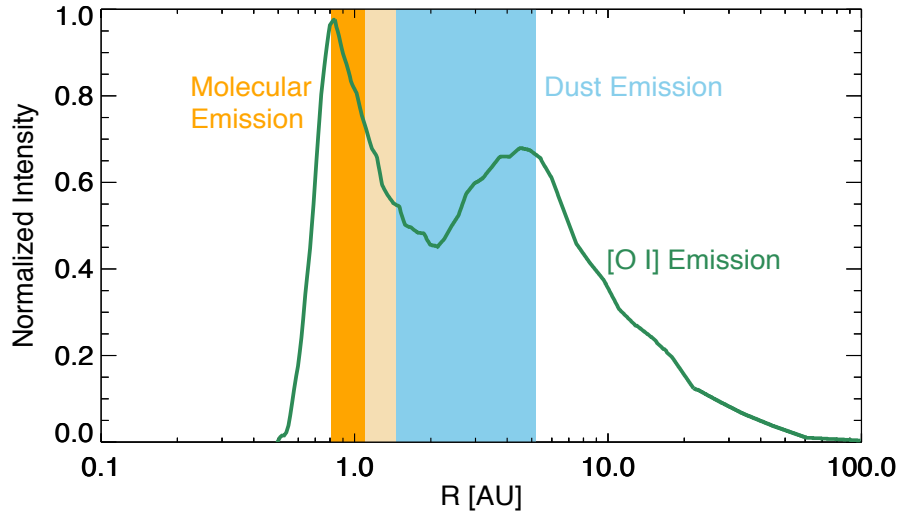
Figure 3.12: Updated Figure 8 from Fedele et al. (2008) showing locations of [O I] emission, dust emission, and molecular emission from HD 101412. The orange region indicates the location of OH, H_2O, and CO gas presented from our analysis. The blue region indicates the dust emission based on MIDI observations, updated to account for the Gaia Collaboration et al. (2016) distance. The light brown region is the overlap of the two regions, with the [O I] emission (in green) remaining unchanged due to the use of similar stellar masses between the studies.

as H_2O and CO_2, in the gas phase implies that if a planet-induced gap is responsible for filtering out the solids from the inwardly accreting material (Kama et al., 2015), the planet would likely be located well inward of the snow line (which we estimate is located at ∼25 au, adopting the distance at which a blackbody is 150 K, but must lie beyond 5 au; Figure 3.11). If the planet were located near or beyond the snow line, dust filtering would remove water ice (and oxygen) as well from the accreting material, creating a more carbon-rich composition, in which molecules like H_2O and CO_2 are unlikely to be abundant (Figure 3.11).

The NIR molecular emission from HD 101412 overlaps the [O I] emission from the source and is roughly coincident spatially with the inner edge of the dust disk seen in the mid-infrared. The mid-infrared dust emission arises from 1.1 to 5.2 au when taking into consideration the new distance from *Gaia* (Figure 3.12; Fedele et al. 2008; van der Plas et al. 2008). The structure shown in Figure 3.12 is analogous to a miniature photodissociation region with the inner emission arising from [O I], then molecular emission, followed by dust emission. The [O I] emission probes the tenuous atomic layer of the disk that is depleted of dust and molecules. It is not clear what the radial extent of the disk is as there are presently no far-infrared or submillimeter observations that would probe the

cooler dust arising from beyond 5 au.

Given the high inclination of the system (i = 86°; Section 3.4), the hot molecular emission we see may be coming from the inner wall of the far side of the disk. A viewing angle 4° from edge-on appears large enough to obtain an unobstructed view of the bright molecular emission from the far side of the inner disk. Given the temperature of the molecular emission (1300 K; Section 3.4) and the stellar mass (2.5 $M_\odot$; Section 3.1), the disk scale height at the radius of the molecular emission (1 au) is 0.05 au if the gas is in hydrostatic equilibrium; thus the height of the molecular emitting gas on the near side of the disk may rise $\sim 1.5°$ above the midplane when viewed from the far side of the disk 2 au away.

There are two observational approaches to test our hypothesis that the luminosity of the water emission and CO bandhead emission are enhanced by the depletion of dust in the inner disk (by a factor of 6 or more; Kama et al. 2015). Firstly, one can compare the EW of the molecular emission to the gas-to-dust ratio of the accreting material as inferred from photospheric abundances of the star. Larger molecular emission EWs are expected for systems with larger gas-to-dust ratios. Secondly, one can test the role of the disk inclination by observing additional edge-on systems and comparing these to more inclined systems. The emission from the edge-on systems will be dominated by the inner wall of the disk and should probe denser gas than the more face-on systems where the emission is dominated by less dense gas from the disk surface.

The feasibility of this scenario can also be tested through thermochemical modeling of the inner disk. One possible concern is that if grains are too underabundant, it is difficult to synthesize H_2 on grains, which is a critical first step in the gas phase synthesis of molecules, such as OH, CO, and water. Severe dust depletion may make it difficult to counteract photodestruction of molecules and to sustain a substantial reservoir of molecular gas. Self-consistently fitting the infrared portion of the SED and molecular column density in the disk atmosphere will inform the feasibility of our hypothesis.

3.7 Conclusions

We present the first detection of water emission at 2.9 μm in a Herbig Ae/Be star system, along with a new detection of OH rovibrational emission. The OH emission observed represents the strongest ever observed in an HAeBe disk in terms of a line-to-continuum ratio. The observed line

profiles for both OH and H_2O indicate that the emitting region for both molecules is narrow and ~ 1 au from the star.

The bright molecular emission from HD 101412 may be related to its photospheric abundance pattern, i.e., its nature as a λ Boö star, and the disk's large inclination angle. If the low abundance of refractory elements is a result of selective accretion of gas relative to dust, as has been previously hypothesized, the inner disk from which HD 101412 accretes should be strongly dust-depleted and its continuum should be more optically thin. This situation would tend to produce strong molecular emission from the inner disk, as is observed. Our detection of C- and O-bearing molecules from the inner disk is consistent with the expected presence in this scenario of abundant volatiles in the accreting material.

Chapter 4

Molecular emission from the circumbinary disk of V380 Ori[1]

4.1 Introduction

Studies of molecular species in the inner disk regions of Herbig Ae/Be stars has yielded a wealth of information on the structure and dynamics of these systems. While CO is the most abundant molecular species in this region that can be observed in the near-infrared (NIR) (Blake & Boogert, 2004; Brittain et al., 2007; Salyk et al., 2011b,a; Brown et al., 2013; van der Plas et al., 2015; Banzatti & Pontoppidan, 2015), OH has proven to be another key tracer for the structure and chemical make-up of the circumstellar environment (Mandell et al., 2008; Fedele et al., 2011; Brittain et al., 2016; Adams et al., 2019). The observed prominence of OH in Herbig Ae/Be systems has been attributed to the strong UV radiation from the central star photodissociating H_2O in the disk (Fedele et al., 2011; Brittain et al., 2016).

V380 Ori is a known binary star system (Leinert et al., 1994), with a circumbinary disk. Fairlamb et al. (2015) determine an effective temperature of 9750 ± 750 K for the primary star and a distance of 330^{+73}_{-17}. They find that V380 Ori has a mass of $2.3^{+1.1}_{-0.2}$ $M_\odot$ and radius of $2.5^{+0.5}_{-0.1}$ $R_\odot$. The recent Gaia data release (Gaia Collaboration et al., 2016, 2018) reports a distance of 490^{+42}_{-36} pc, and, using Siess pre-main sequence models (Siess et al., 2000), we recalculate the mass and radius

---

[1]Based on work submitted for publication to the Publications of the Astronomical Society of the Pacific.

based off this distance. For this paper, we use M = 3.0 $M_\odot$, R = 3.8 $R_\odot$, and L = 113.1 $L_\odot$. Siess's models also give an age of 1.95 Myr for V380 Ori. Alecian et al. (2009) report the presence of a low-mass companion that is close ($a \sin i \sim 0.83$ milliarcsec) to the central star. At a distance of 490 pc, this would mean the stars are separated by 0.4 au. Leinert et al. (1994) and Leinert et al. (1997) report the presence of a tertiary infrared companion located 0.154 arcsec, which would correspond to a distance of 75 au.

Fedele et al. (2008) first reported the detection of OH around V380 Ori. They detected the P4.5 (1+, 1−) doublet in emission with an asymmetric profile. Per their modeling, they report that the OH emission extends from 2 au out to 15 au. This would mean that the companion lies within the inner radius of the OH emitting region, and would likely be the source of the asymmetric profile. CO P26 $\nu = 1 \rightarrow 0$ emission presented in Brittain et al. (2016), obtained with Phoenix (R $\sim 50,000$), does not show the same asymmetric profile observed in the OH P4.5 doublet.

We present a new detection of OH P5.5 (2−, 2+) emission in V380 Ori. Section 4.2 details the data acquisition and reduction process. Section 4.3 presents the new detection with a comparison to the P4.5 emission reported in Fedele et al. (2011). Modeling of the emission lines is presented in section 4.4, followed by discussion and conclusions in section 4.5.

4.2   Observations

Data were acquired using the Phoenix spectrograph (Hinkle et al., 1998, 2000, 2003) on the 4m Mayall telescope located at Kitt Peak under proposal ID 2013B-0376. Observations were made over 2 nights. Flats and darks were obtained each night in order to correct for hot/dead pixels and instrument noise. Observations were made in an *ABBA* nod pattern. Data reduction was performed using custom scripts, described in detail in Brittain et al. (2007). Exposures were combined (*A* - *B*) in order to remove sky emission lines. Next, a Sky Synthesis Program (SSP; Kunde & Maguire 1974), which accesses the 2003 HITRAN molecular database (Rothman et al., 2003), was computed in order to wavelength calibrate the spectra. After both the science and telluric standard (γ Ori) were reduced, they were ratioed in order to remove telluric absorption features. Spectral regions where the atmospheric transmittance was below 50% were removed. Observation information is provided in Table 4.1.

Archival data was also obtained from the European Southern Observatory that observed

Star	Date	Airmass	Exposures	Int. Time (s)	Emission Features
OH Observations					
V380 Ori	13 Feb 2014	1.66	24	14400	OH P5.5
γ Ori	13 Feb 2014	2.08	48	2880	
V380 Ori	14 Feb 2014	1.55	24	14400	OH P5.5
γ Ori	14 Feb 2014	1.67	20	1200	
Archival OH Observations					
V380 Ori	8 Dec 2008	1.33	24	360	OH P4.5
o Ori	8 Dec 2008	1.54	4	120	
V380 Ori	14 Sep 2014	1.46	44	2640	OH P4.5, P9.5, P10.5
γ Tri	14 Sep 2014	1.28	16	960	
CO Observations					
V380 Ori	26 Nov 2004	1.56	8	480	CO P26
β Aur	26 Nov 2004	1.40	4	240	
V380 Ori	13 Jan 2006	1.65	16	960	All other CO
ζ Ori	13 Jan 2006	1.98	8	480	

Table 4.1: Observation log for V380 Ori data used in this report. Observations at Kitt Peak National Observatory using the 4m Mayall telescope were taken on 13 & 14 Feb 2014. Archival OH observations were used to determine the temperature of the OH gas. CRIRES data (8 Dec 2008; Fedele et al. 2011) were reduced using the same procedure as the Phoenix OH data presented. NIRSPEC data (14 Sep 2014; Brittain et al. 2016) were used to provide additional OH emission features (P9.5 and P10.5) for analysis. CO Observations were taken with NIRSPEC at Keck II (26 Nov 2004) and Phoenix at Gemini South (13 Jan 2006; Brittain et al. 2016).
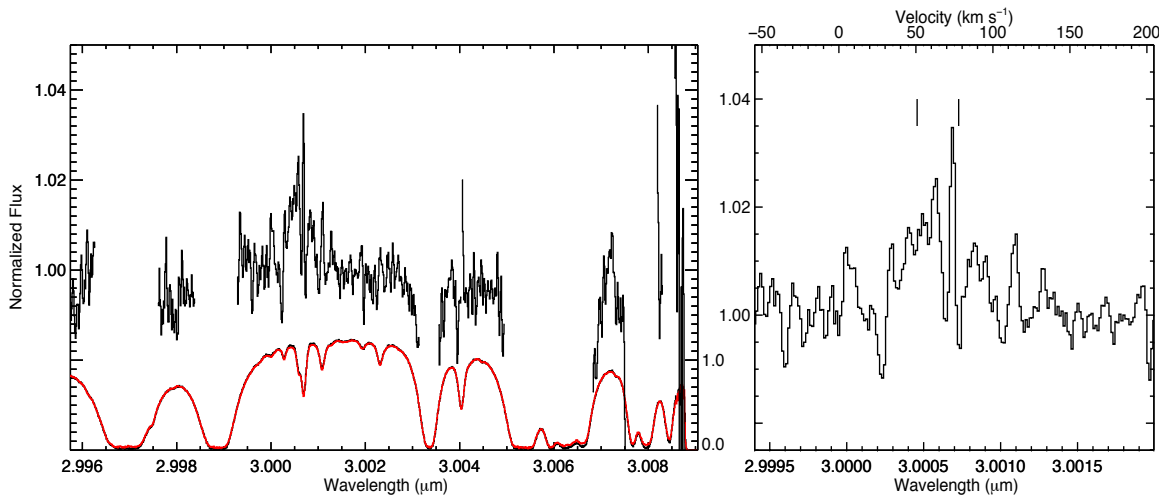
Figure 4.1: Detection of the OH P5.5 (2−, 2+) doublet at 3 μm. The reduced science spectrum is plotted in black with the standard star spectrum over-plotted in red. The ratio is plotted above, offset by 2 units and scaled by a factor of 50. The left y-axis shows the scale for the ratioed spectrum, while the right shows the scale for the science and standard spectra. The right plot is zoomed in on the P5.5 (2−, 2+) emission feature. The upper x-axis shows the velocity shift observed for the P5.5 emission feature, with zero corresponding with Earth's rest frame for the P5.5 (2+) doublet. The black vertical lines label the doublet features in the rest frame of V380 Ori. We report a heliocentric velocity shift of 48 km s^{-1} which is consistent with observed radial velocity measurements ($\sim$27 km s^{-1}; Alecian et al. 2009) plus a radial velocity correction factor based on Earth's orbit of 21 km s^{-1}.
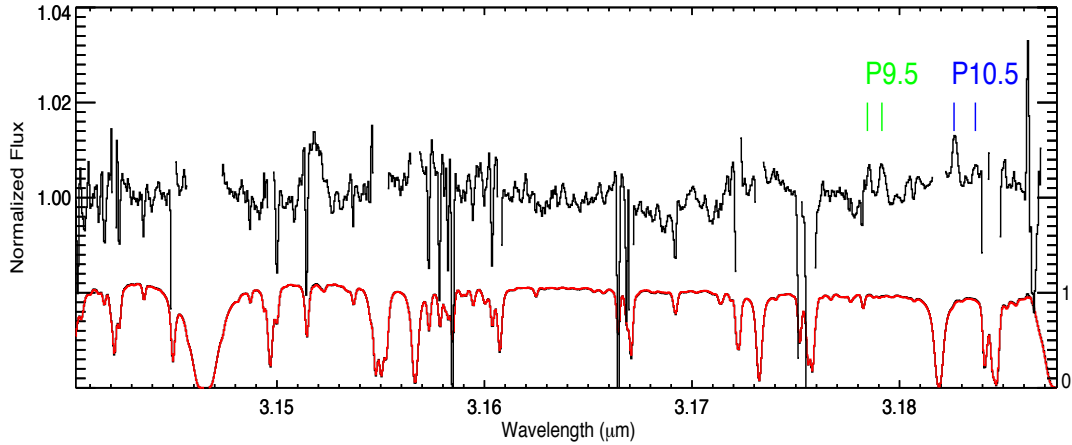
Figure 4.2: OH P9.5 (2−, 2+) and P10.5 (1+, 1−) doublets taken with NIRSPEC on Keck II (14 Sep 2014). The reduced science spectrum is plotted in black with the standard star spectrum over-plotted in red. The ratio is plotted above, offset by 2 units and scaled by a factor of 50. The left y-axis shows the scale for the ratioed spectrum, while the right shows the scale for the science and standard spectra. The P9.5 and P10.5 doublets are indicated by the green and blue hashes, respectively. The P10.5 (1−) transition falls in an absorption feature.

the P4.5 (1+, 1−) doublet, initially presented in Fedele et al. (2011). This data was obtained using CRIRES on the *Very Large Telescope* UT1, and was reduced using similar procedures as the Phoenix data. In order to determine the flux of the OH emission, flux density values were found using the Vizier Photometry Viewer (Ochsenbein et al., 2000) using 2MASS K_s filter and WISE W1 filter photometric observations. Since these filters do not overlap the 2.94 or 3.0 μm region, a linear fit between the 2MASS K_s and WISE W1 filter was used to determine the continuum flux density in this region. The flux density value used is 1.25×10^{-9} erg s^{-1} cm^{-2} μm^{-1} for both the P4.5 (1+, 1−) and P5.5 (2−, 2+) doublets.

We also look at CO observations from Gemini South using Phoenix and Keck II using NIRSPEC (McLean et al., 1998). These data were reduced using similar methods employed in the OH data reduction explained above. The data were obtained 13 Jan 2006 and 26 Nov 2004, respectively. Phoenix data were first reported in Brittain et al. (2016). The flux density used for CO P(26) emission feature was determined between WISE W2 and Johnson M filters and was found to be 3.80×10^{-10} erg s^{-1} cm^{-2} μm^{-1}.
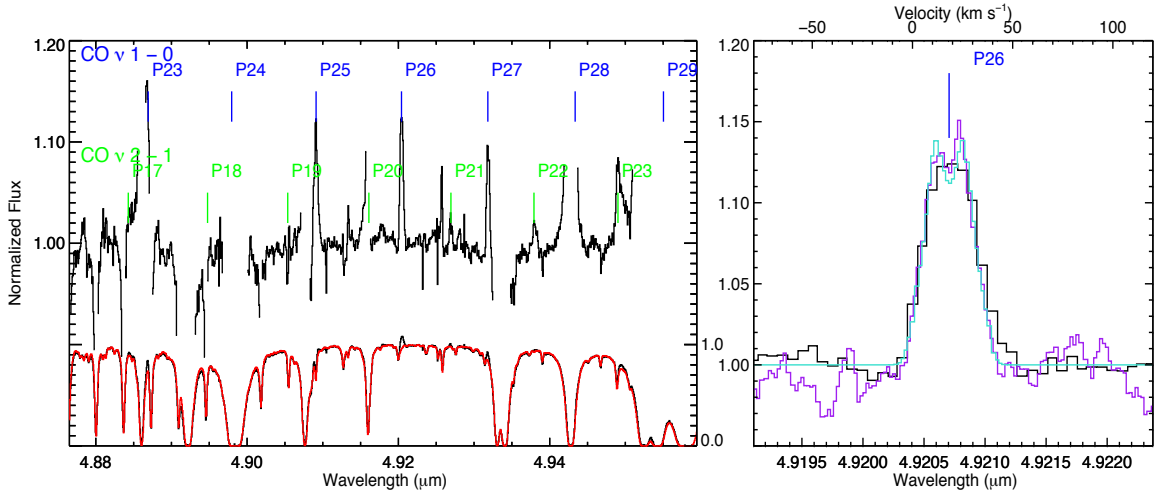
Figure 4.3: CO emission observed toward V380 Ori with NIRSPEC on Keck II. Like in Figure 4.1, the left panel shows V380 Ori's spectrum in black, the standard star spectrum over-plotted in red, and the ratio offset by 2 and stretched by a factor of 10 above. The CO $\nu = 1 \to 0$ line positions are indicated by the blue tick marks and the CO $\nu = 2 \to 1$ line positions are indicated by the green tick marks. The right panel shows a zoom in on the CO $\nu = 1 \to 0$ P26 emission line. The NIRSPEC observation is plotted in black (as in the left panel), the Phoenix P26 emission feature is plotted in purple, and the best fit model is plotted in turquoise. The upper x-axis shows the velocity shift observed centered on the P26 rest frame wavelength. We report a heliocentric velocity shift of 19 km s^{-1} for the NIRSPEC observations which is consistent with observed radial velocity measurements ($\sim$27 km s^{-1}; Alecian et al. 2009) plus a radial velocity correction factor based on Earth's orbit of -8 km s^{-1}.

4.3 Results

We detect the P5.5 (2$-$, 2+) doublet in emission for V380 Ori in the Phoenix observations from 14 Feb 2014. The profile is presented in Figure 4.1. The equivalent width (EW) is determined by looking over the full OH P5.5 doublet and dividing by 2 as the components are not individually resolved. We find that the EW = $3.57 \pm 0.11 \times 10^{-6}$ μm. Converting this to a luminosity, we find that $L_{\mathrm{OH}} = 3.35 \pm 0.10 \times 10^{-5}$ $L_\odot$. There is a telluric absorption feature within the P5.5 emission region. It does not drop below the 50% transmittance cutoff, therefore the region is kept in the analysis. This absorption feature does affect the profile, but only over a small region of the P5.5 feature.

The P4.5 doublet has an EW measured at 5.4×10^{-6} μm for the red portion of the doublet and 6.0×10^{-6} μm for the blue portion in the re-reduced CRIRES data from 5 Dec 2008. Using 490 pc and a flux density of 1.25×10^{-9} erg s^{-1} cm^{-2} μm^{-1} at 2.92 μm gives an OH P4.5 luminosity of
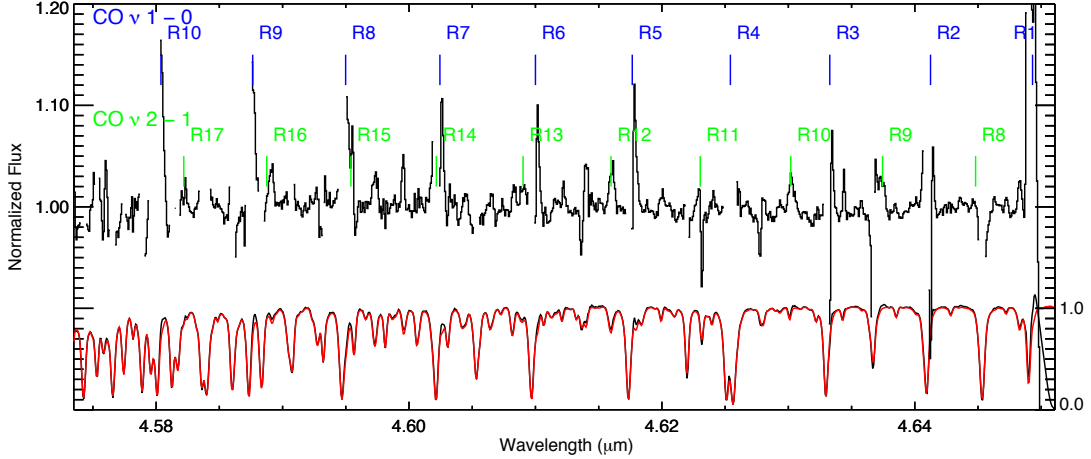
Figure 4.4: CO emission taken with NIRSPEC on Keck II. The $\nu = 1 \to 0$ emission are not Doppler shifted enough to be distinguished from the telluric absorption.

$5.31 \pm 0.15 \times 10^{-5}\ L_{\odot}$, averaged over each doublet. This is consistent the luminosity determined by Fedele et al. (2011) of $7.48 \pm 4.45 \times 10^{-5}\ L_{\odot}$, as determined using their OH P4.5 EW ($8 \times 10^{-6}\ \mu$m) and the flux density used in our analysis. Figure 4.2 shows the P9.5 and P10.5 emission features.

Upper limits on H_2O emission are similarly consistent with Fedele et al. (2011). Using their upper limit definition of $3 \times \sigma \times \Delta\lambda$, where $\Delta\lambda = 30$ km s^{-1}. We find an EW $\leq 2.70 \times 10^{-6}\ \mu$m, or $L_{H_2O} \leq 2.52 \times 10^{-5}\ L_{\odot}$.

CO observations made using NIRSPEC at the Keck II telescope and Phoenix on Gemini South give clean detections of the CO $\nu = 1 \to 0$ P25, P26, and P27 emission lines. CO $\nu = 2 \to 1$ emission lines are also observed in the NIRSPEC observation (left panel in Figure 4.3). Flux values for the emission features are consistent across instruments. We can clearly see the double peaked emission line characteristic of gas in a Keplerian rotation in the Phoenix observation (right panel in Figure 4.3). We do not see the double peak in the NIRSPEC data as the resolution is not sufficient. We find a P26 EW of $6.45 \pm 0.12 \times 10^{-5}\ \mu$m. This corresponds to a luminosity of $17.6 \pm 0.3 \times 10^{-5}\ L_{\odot}$. This gives a CO/OH ratio of ~ 11, which is consistent with the luminosity ratio found in Brittain et al. (2016). Figure 4.4 shows the low J emission lines observed with NIRSPEC.

Figure 4.5 estimates the rotational temperature of the OH based off P4.5, P5.5, P9.5, and P10.5 emission features. The P9.5 and P10.5 emission features were observed using NIRSPEC on
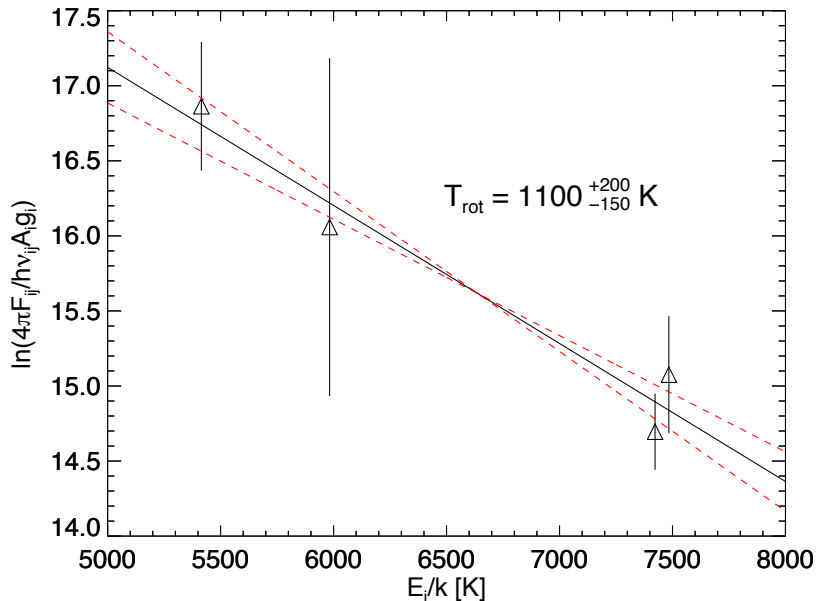
Figure 4.5: Boltzmann plot to determine the rotational temperature of OH gas. Error bars for both the data points and fit are 1σ. Transition data are obtained from HITRAN (Gordon et al., 2017).

Keck II. Brittain et al. (2016) present the P4.5 emission feature from this data. Due to the presence of the absorption feature in the P5.5 emission feature, the error bars on the flux are large. In spite of that, we are able to estimate a rotational temperature for OH of $T_{\rm rot} = 1100^{+200}_{-150}$ K.

The signal-to-noise ratio in the NIRSPEC data is better than the Phoenix observations so the NIRSPEC fluxes are used to calculate the rotational temperature. Figure 4.6 shows the gas temperature determined from three $\nu = 1 \rightarrow 0$ detections and seven CO $\nu = 2 \rightarrow 1$ detections also observed with NIRSPEC. The gas temperature is found to be 700^{+60}_{-35} K fitting all 10 data points.

4.4 Modeling

We perform modeling on both the P4.5 and P5.5 emission features to determine the origins of the emission. The model assumes Keplerian rotation ($v \propto r^{1/2}$) with a power-law intensity ($I \propto r^{-2}$). Initial parameters are centered around the same best fit parameters reported in Fedele et al. (2008) and then a χ^2 minimization is performed with a grid over the inner radius, $R_{\rm in}$, outer radius, $R_{\rm out}$, and the inclination angle, i. The initial parameter space search is done by fitting the P4.5 emission feature as it has the higher line-to-continuum ratio and is less affected by telluric
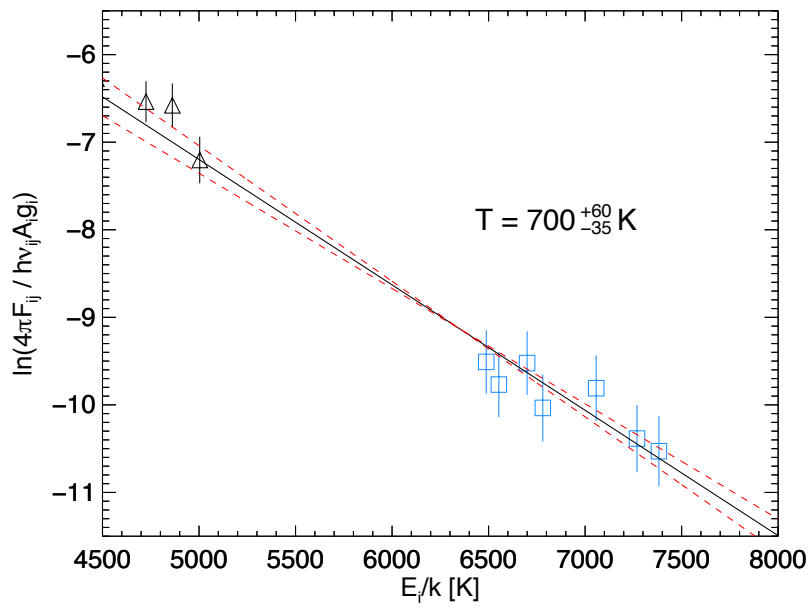
Figure 4.6: Boltzmann plot to determine the rotational temperature of CO gas. CO $\nu = 1 \to 0$ data are presented as triangles and CO $\nu = 2 \to 1$ data are presented as blue squares. Error bars on the data points and the best fits are 1σ. Transition data are obtained from HITRAN (Gordon et al., 2017).
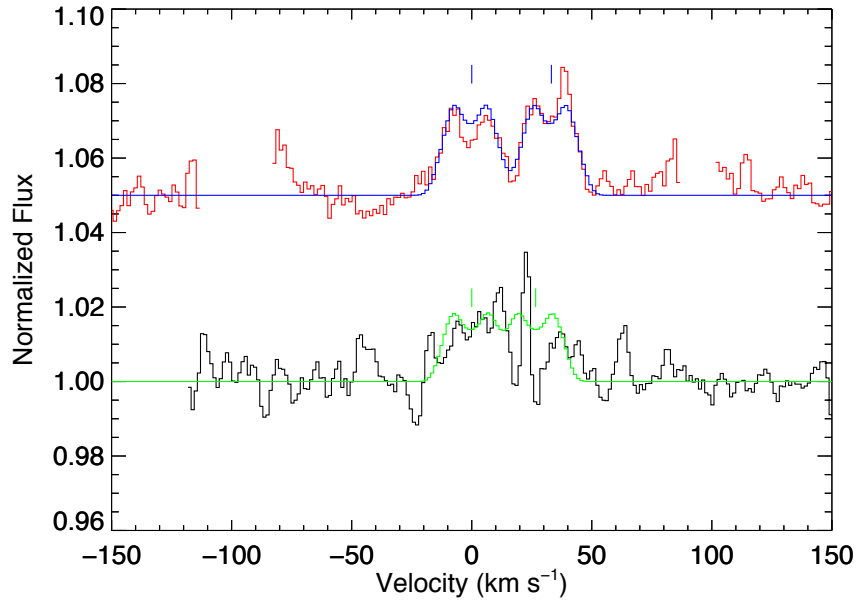
Figure 4.7: OH P5.5 (2−, 2+) (in black) emission feature vs. P4.5 (1+, 1−) (in red) presented in Fedele et al. (2011). P4.5 data has been shifted up by 0.05 units. The tick marks above each spectrum indicates the location of each doublet feature, with the zero velocity bin shifted such that the shorter wavelength transition is set to 0 km s^{-1}. In order to do this, a heliocentric radial velocity of 48 km s^{-1} was used for the P5.5 data and 24 km s^{-1} was used for the P4.5 data. Both of these radial velocities are consistent with radial velocity measurements from Alecian et al. (2009) plus additional components from Earth's motion found using RVcorrect in IRAF. Best fit models are plotted over each spectrum; green for the P5.5 data and blue for the P4.5 data.
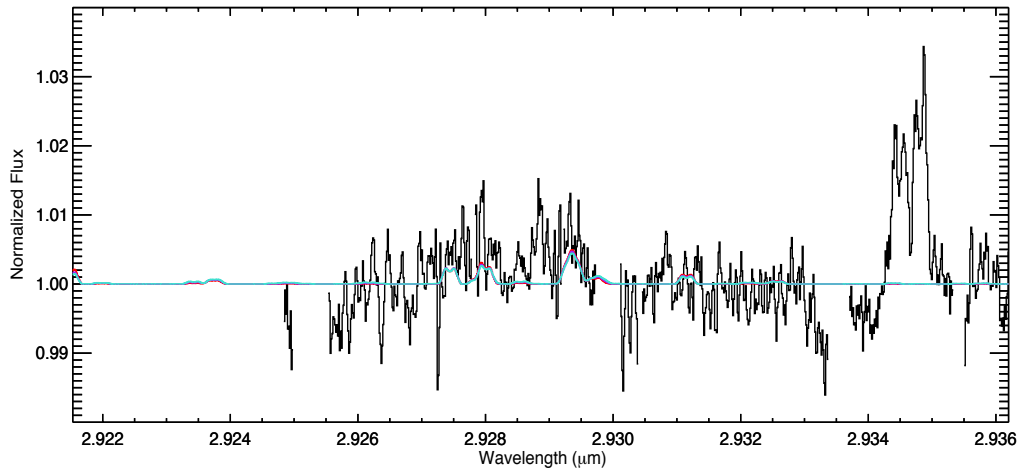
Figure 4.8:   LTE water emission model for the region near 2.93 μm. The red spectrum corresponds to a gas temperature of 700 K, the purple spectrum corresponds to a temperature of 1000 K, and the turquoise spectrum corresponds to a temperature of 1300 K. Emission region parameters are the same as used for the OH emission models: $R_{\mathrm{in}} = 2.5$ au, $R_{\mathrm{out}} = 16.0$ au, and $i = 30°$.

absorption. After the best fit parameters are determined for the P4.5 doublet, the P5.5 emission feature is fit with the model.

Models were computed looking at a range of inner emitting radius (from 2-6 au), outer emitting radius (from 10-20 au), and disk inclination angle (20°-60°). Final best fit parameters are $R_{\mathrm{in}} = 2.5$ au, $R_{\mathrm{out}} = 16.0$ au and $i = 30°$ for the P4.5 doublet. These values are consistent with best fit models from Fedele et al. (2011).

Due to the presence of a telluric absorption feature in the P5.5 doublet, we use the best fit parameters from the P4.5 model fitting. The P5.5 data is noisier across the emission feature so the fit does not align as well as the fit to the P4.5 data, however, the model emission feature's width is consistent with the data and the peaks of the model are within the noise (1σ noise is 0.0075 in normalized flux units) levels of the P5.5 data. Figure 4.7 shows the model fit to both the P4.5 (top) and P5.5 (bottom) emission features.

Modeling of the CO $\nu = 1 \rightarrow 0$ emission line profile made use of the Phoenix data due to the higher spectral resolution. The data was fit in the same manner as the OH P4.5 emission. The final best fit parameters for the CO emission are different from those found for the OH emission: $R_{\mathrm{in}} = 1.5$ au, $R_{\mathrm{out}} = 16.0$ au and $i = 30°$. This shows that the CO emission arises from a radius interior to that of the OH.

4.5 Discussion

The observations of OH and CO indicate that the molecules do not arise from the exact same location within the circumstellar disk. Specifically, CO emission arises inward of OH by about 1 au. Even with this being the case, the molecular emission appears to lie at a location consistent with model results looking at tidal effects on the inner disk wall from binary stars. Artymowicz & Lubow (1994) predict that the inner disk should extend to $r_{in} \sim 1.7a_{bin}$ for a binary star system with $\mu = 0.25$, as has been reported for V380 Ori. For the binary stars interior to the circumstellar disk, this would be about 1.36 au, which is inward of both CO and OH best fit models.

The gas temperatures we report from the Boltzmann plots do indicate a possible vertical temperature gradient in the V380 Ori circumstellar disk. The OH rotational temperature we find is considerably hotter (400 $\pm$ 160 K) than that of the CO. This could be explained by the OH gas coming from the more diffuse upper layers of the disk, whereas the CO would be coming from cooler, denser gas that lies below the OH. Our models of water emission near 2.93 μm indicate the temperature of the water is comparable to the low temperature of the CO gas, however, due to the non-detection, we are not able to tightly constrain the temperature of the water. Models from Ádámkovics et al. (2014) and Ádámkovics et al. (2016) indicate that far-ultraviolet radiation pushes the molecular layer deeper into the disk, and is able to dissociate water to produce more OH in the upper disk atmosphere. Therefore, it is expected that the CO and water in circumstellar disks would be cooler than the OH. Unfortunately, higher signal-to-noise observations would be unlikely to provide better information due to the weak water emission in V380 Ori. Better constraints of the OH gas temperature could be achieved by looking at higher energy transitions and would enable more rigorous testing of thermochemical models.

Fedele et al. (2011) first reported the detection of OH P4.5 (1+, 1−) emission from V380 Ori. In their analysis, they report an asymmetry in the OH emission. They attribute the asymmetry to either a deviation from Keplerian motion of the gas or an inhomogeneous distribution of the gas. The fact that V380 Ori has a known companion within the inner radius of the circumstellar disk could cause the inner rim to become eccentric, and, thus, deviate from a circular velocity profile (Kley & Dirksen, 2006).

If the companion is the source of the deviation from a circular velocity profile, as postulated by Fedele et al. (2011), then the asymmetry should precess on a 10°/1000 orbit timescale (Kley

& Dirksen, 2006). As such, the asymmetry would be anticipated to be mirrored in other emission lines originating from similar regions of the disk. CO $\nu = 1 \rightarrow 0$ P26 emission taken with Phoenix (Troutman, 2010; Brittain et al., 2016) shows a slight asymmetry (within the noise levels of the observations, $1\sigma = 0.015$ in units of normalized flux), however, it is in the blue portion of the emission feature, whereas the OH P4.5 asymmetry reported in Fedele et al. (2011) is in the red portion. There is a ~ 3 year gap between the observations, thus, if the asymmetry is real, the source is unlikely to be caused by tidal interactions from the binary companion. Analysis of the CO P26 emission feature shows a similar radial extent, however, the emission arises from a smaller inner radius. Best fit parameters for the P26 emission line are $R_{\mathrm{in}} = 1.5$ au, $R_{\mathrm{out}} = 16.0$ au, and $i = 30°$.

In order to compare our observations of the OH P5.5 doublet, we re-reduced the data presented in Fedele et al. (2011). Keplerian modeling of the OH emission features indicates that the emission originates in a disk that extends from 2.5 au out to 16 au, with a disk that is inclined by 30°. These findings are consistent with the disk parameters derived by Fedele et al. (2011), however, we do not detect the same asymmetry in the system in either the P4.5 or P5.5 doublets. Our observations of the OH P5.5 doublet do not show the same asymmetry, however, the strength of the asymmetry from Fedele et al. (2011) would be masked due to our lower signal-to-noise ratio. We investigated the possibility that the issue could be misalignment of the science and standard stars during the removal of the telluric absorption features, but this did not change the profile of the P4.5 emission feature to reproduce the asymmetry.

4.6 Conclusions

We present a new detection of the OH P5.5 (2−, 2+) doublet coming from the circumstellar disk of V380 Ori. This new detection allows us to estimate the rotational temperature of the OH gas in the disk. Comparison of the P5.5 doublet to archival P4.5 (1+, 1−) data show that the emission is consistent with previous reports from Fedele et al. (2011). In our report, we reduced the archival P4.5 emission in a manner consistent with our P5.5 data reduction and were unable to reproduce the observed asymmetry reported in Fedele et al. (2011).

Chapter 5

OH and H$_2$O study of Herbig Ae/Be stars

5.1 Introduction

Herbig Ae/Be (HAeBe) stars are intermediate-mass (2-8 M$_\odot$) young stellar objects that are associated with an infrared excess in their spectral energy distribution attributed to circumstellar dust and gas (Herbig, 1960; Waters & Waelkens, 1998; Vieira et al., 2003). Molecular emission is a key diagnostic for the inner dynamics of the circumstellar environments of pre-main sequence stars. The strongest molecular features in HAeBe spectra come from CO rovibrational emission (Blake & Boogert, 2004; Brittain et al., 2007; Salyk et al., 2011b,a; Brown et al., 2013; Banzatti & Pontoppidan, 2015; van der Plas et al., 2015; Hein Bertelsen et al., 2016a), however, OH has also been observed in the inner regions of their circumstellar disks (Mandell et al., 2008; Fedele et al., 2011; Brittain et al., 2016). Water vapor emission has proven to be more difficult to observe in HAeBe disks (Mandell et al., 2008; Fedele et al., 2011; Banzatti et al., 2017).

Near-infrared (NIR) OH emission in lower mass T Tauri stars tends to be weaker than the water emission observed in the same spectral region (near 2.9 μm; Salyk et al. 2008; Banzatti et al. 2017). This trend changes as you look at higher mass HAeBe stars as the OH emission tends to be the only molecular emission observed near 2.9 μm (Mandell et al., 2008; Fedele et al., 2011). Brittain et al. (2016) present a survey of OH emission from HAeBe stars and find that a fraction of 10 out of

21 (47.6%) HAeBe sources show OH in emission. They compare the strength of the OH P4.5 (1+, 1−) emission to CO $\nu = 1 \to 0$ P30 emission and find that the two line strengths correlate and their line profiles suggest they originate from similar locations within the circumstellar disk.

While difficult to observe, water vapor is expected to reside in the inner regions of HAeBe disks (Walsh et al., 2015; Ádámkovics et al., 2014, 2016; Najita & Ádámkovics, 2017). Water is an important ingredient in disk chemistry and in the origins of life on Earth, so it is necessary to understand where it resides within these systems. Water is the first molecule to condense in the disk as it has the highest condensation temperature ($\sim$150 K for the typical densities found in the circumstellar disk). This means that water determines where the first ice forms in the disk. This potentially has an impact on where and when protoplanet formation can commence. Water is also a good absorber of ultraviolet radiation. Therefore, the presence of water in the disk could act as a shield to allow for more complex molecules to form in the inner regions of the circumstellar disk and not be affected by the ultraviolet radiation from the central star.

NIR emission from H_2O was only recently detected around the HAeBe star HD 101412 (Adams et al., 2019). Adams et al. (2019) concluded that the detection of water around HD 101412, along with bright OH and CO fundamental and overtone emission are due to a combination of effects: a depletion of dust in the inner disk and a high inclination angle (i = 86°). Now the question is if this source is unique or if it is possible to find more water around systems with similar stellar and/or disk parameters.

This study expands on the OH observations presented in Brittain et al. (2016) while also looking at the relative strengths of OH and H_2O and how this ratio compares to various stellar and disk parameters across both HAeBe and T Tauri stars. All data presented in this report is taken from the European Southern Observatory (ESO) data archives. Observation and data reduction procedures are presented in Section 2. Section 3 provides an overview of the detections and non-detections from the new HAeBe sources along with a description of the modeling process for water detections and upper limits. Section 4 presents a discussion on our findings with concluding remarks.

5.2 Observations

Data were obtained using the ESO Data Archives. All observations were made using the Cryogenic Infrared Echelle Spectrograph (CRIRES, Käufl et al. 2004) on the ESO *Very Large Tele-*

scope U1 at the La Silla Paranal Observatory under programme IDs 089.C-0827(A) and 091.C-0796(A). Detailed observation information is presented in Table 5.1.

Data reduction was performed using custom software based on algorithms developed for the reduction of Phoenix and Near-Infrared echelle SPECtrograph (NIRSPEC) data (described in Brittain et al. 2007). Systematic effects were removed using flat and dark files taken at the start of each observing night. Data were acquired using an *ABBA* nod pattern in most cases. Occasionally, data were taken in an *ABAB* pattern. These files were combined (A - B), then divided by the normalized flat field file. Hot and bad pixels, along with cosmic ray hits were identified and removed using median values of the combined images. The spectra were extracted using a rectangular extraction method. Wavelength calibration was performed using Sky Synthesis Program (SSP; Kunde & Maguire 1974) model atmosphere to match-up to the telluric absorption features in the extracted spectra. Reduction of the standard stars was performed using the same method. After fully reducing the data, the standard stars were used to remove telluric absorption features by dividing the normalized science star spectrum by the normalized standard star spectrum, and by scaling the standard's spectrum based on the ratio of the airmass of the spectra. Spectral region where atmospheric transmittance was below 50% were excluded.

5.3 Results

The OH P4.5 (1+,1−) doublet is detected in emission in 5 of the 13 (38.5%) sources in this survey. Combining these results with work from Brittain et al. (2016), which also compiled previous OH observations from Mandell et al. (2008), Fedele et al. (2011), and Brittain et al. (2014), brings the total number of OH detections in HAeBe systems to 15 of 31 (48.4%). Three sources (HD 135344B, HD 141569, and HD 179218) in this sample were also observed by Brittain et al. (2016). All three sources were non-detections in both surveys with more constrained upper limits provided by Brittain et al. (2016). HD 135344B OH observations were also presented in Banzatti et al. (2017) from an earlier observation date (2008 04 29). They place the upper luminosity limit at 0.09×10^{-6} L$_\odot$ using the distance listed in Table 5.2.

The flux densities adopted for the continua of the L-band spectra are obtained using values from 2MASS K$_s$ and WISE W1 filter photometry measurements found using the VizieR Photometry Viewer (Ochsenbein et al., 2000). Table 5.3 presents the flux densities used to determine the OH line

Star	Date Observed	Airmass	Int. Time (s)
HD 95881	2012 05 28	1.54	960
γ Mus	2012 05 28	1.49	720
HD 97048	2012 05 27	1.67	1200
ϵ Cha	2012 05 28	1.69	960
HD 100453	2012 05 28	1.30	960
δ Cen	2012 05 28	1.23	240
HD 104237	2013 05 28	1.74	720
γ Mus	2013 05 28	1.54	960
HD 104237	2013 06 26	1.87	720
γ Mus	2013 06 26	1.70	960
HD 135344B	2012 05 28	1.03	1800
k Lup	2012 05 28	1.03	720
HD 139614	2012 05 29	1.08	1200
γ Crv	2012 05 29	1.18	320
HD 141569	2012 05 29	1.26	2520
γ Crv	2012 05 29	1.18	320
HD 163296	2012 05 28	1.03	600
ϵ Sgr	2012 05 28	1.04	720
HD 169142	2012 05 28	1.00	1800
ϵ Sgr	2012 05 28	1.04	720
HD 179218	2012 05 28	1.34	1200
α Del	2012 05 28	1.32	480
IRS 48	2012 05 28	1.03	1920
θ Oph	2012 05 28	1.04	480
T CrA	2012 05 28	1.15	1440
θ Sgr	2012 05 28	1.09	960
VV Ser	2013 05 29	1.10	2160
μ Ser	2013 05 29	1.21	480
VV Ser	2013 06 26	1.12	2160
μ Ser	2013 06 26	1.27	480

Table 5.1: Observation log for all sources. Standard stars used for telluric corrections are listed below the science star. Data were obtained via ESO Data Archive from observing programmes 089.C-0827(A) and 091.C-0796(A).

Star	Other Identifiers	Spectral Type	Meeus Group	Distance (pc)	Radius ($R_\odot$)	Mass ($M_\odot$)	T_{eff} (K)	Inclination (°)	$\text{Log}(\dot{M})$ ($M_\odot\ yr^{-1}$)	Age (Myr)
HD 95881		A0	II	1185^{+48}_{-45}	7.7	5.7	10000 ± 250	55 (1)	≤ -5.65	0.37
HD 97048	HIP 54413	A0Vep	I	185^{+1}_{-1}	1.8	2.5	10500 ± 500	43 (2)	≤ -8.16	6.43
HD 100453	HIP 56354	A9Ve	I	104^{+1}_{-1}	1.6	1.6	7250 ± 250	38 (3)	≤ -8.31	32.55
HD 104237	DX Cha	A0+Sh	II	108^{+1}_{-1}	2.2	2.1	8000 ± 250	18 (4)	$-6.57^{+0.15}_{-0.20}$	6.02
HD 135344B		F8V	II	136^{+1}_{-2}	2.2	1.6	6375 ± 125	14 (5)	$-7.37^{+0.24}_{-0.41}$	11.60
HD 139614		A7Ve	I	135^{+1}_{-1}	1.7	1.7	7750 ± 250	20 (6)	$-7.63^{+0.20}_{-0.30}$	14.85
HD 141569	HIP 77542	A2Ve	II	$111^{+0.5}_{-1}$	2.1	2.5	9750 ± 250	51 (7)	$-7.65^{+0.33}_{-0.47}$	4.97
HD 163296	MWC 275	A1Vep	II	101^{+2}_{-1}	2.2	2.4	9250 ± 250	46 (8)	$-7.05^{+0.14}_{-0.30}$	5.98
HD 169142 (b)	MWC 925	B9V	I	114^{+1}_{-1}	1.5	1.6	7500 ± 200	13 (9)	≤ -8.15	10.79
HD 179218 (b)	MWC 614	A0Ve	I	266^{+3}_{-3}	3.3	3.1	9640 ± 250	57 (10)	≤ -7.30	1.82
IRS 48	ISO-Oph 159	A0	I	134^{+3}_{-2}	1.9	2.0	9000 ± 550	50 (11)	-8.50 (g)	7.01
VV Ser (f)		A5Ve	II	420^{+14}_{-13}	2.4	3.3	13800 ± 200	70 (12)	$-6.51^{+0.29}_{-0.18}$	3.35
T CrA (d)		F0	I	130^{+20}_{-20} (a)	1.8	1.5	7200 (c)	–	≤ -8.20 (e)	5.69

Table 5.2: Stellar parameters for Herbig Ae/Be stars presented. Distances are from Gaia Collaboration et al. (2018) where available while other parameters were obtained from Fairlamb et al. (2015) and updated using Siess et al. (2000) Pre-main-sequence models based on Gaia distances unless otherwise noted. Reference for stellar parameters not taken from Fairlamb et al. (2015, 2017): (a) Hillenbrand et al. (1992); (b) Folsom et al. (2012), (c) Maaskant et al. (2014), (d) Menu et al. (2015), (e) Garcia Lopez et al. (2006), (f) Vioque et al. (2018), (g) Banzatti et al. (2017). Inclination references: (1) Verhoeff et al. (2010); (2) Lagage et al. (2006); (3) Benisty et al. (2017); (4) Grady et al. (2004); (5) Pontoppidan et al. (2008); (6) Labadie et al. (2014); (7) Weinberger et al. (1999); (8) Muro-Arena et al. (2018); (9) Raman et al. (2006); (10) Fedele et al. (2008); (11) van der Marel et al. (2013); (12) Pontoppidan et al. (2007).

ID	Star	Flux Density$_{2.93\mu m}$ (erg s^{-1} cm^{-2} μm^{-1})	OH EW (10^{-6} μm)	L_{OH} ($10^{-5}L_{\odot}$)	$L_{\mathrm{H_2O}}$ ($10^{-5}L_{\odot}$)	L_{CO} ($10^{-5}L_{\odot}$)	Gas/Dust	[12]−[60]	$L_{\mathrm{NIR}}/L_{\mathrm{MIR}}$
1	HD 95881	1.6×10^{-9}	1.66 ± 0.03	11.62 ± 0.21	≤ 5.69	221 ± 10.0 (1)	–	-2.0	2.1
2	HD 97048	1.5×10^{-9}	1.26 ± 0.05	0.20 ± 0.01	≤ 0.38	4.58 ± 1.23 (1)	794.3	1.7	0.9
3	HD 100453	1.5×10^{-9}	≤ 1.56	≤ 0.08	≤ 0.08	≤ 0.03 (2)	123.9	1.8	2.4
4	HD 101412	3.2×10^{-10}	43.0 ± 2.0	7.18 ± 0.33	3.96 ± 0.30	≤ 6.31 (2)	569.1	-0.7	1.6
5	HD 104237	3.6×10^{-9}	4.71 ± 0.07	0.62 ± 0.01	0.93 ± 0.03	3.44 ± 0.09 (1)	122.2	-0.5	13.8
6	HD 135344B	1.2×10^{-9}	≤ 0.96	≤ 0.07	≤ 0.07	1.06 ± 0.17 (1)	–	3.0	7.1
7	HD 139614	4.7×10^{-10}	≤ 4.59	≤ 0.12	≤ 0.12	0.26 ± 0.05 (2)	254.8	1.7	1.3
8	HD 141569	3.8×10^{-10}	≤ 3.49	≤ 0.05	≤ 0.05	≤ 0.01 (3)	541.2	2.5	10.9
9	HD 163296	3.6×10^{-9}	3.73 ± 0.08	0.43 ± 0.01	1.16 ± 0.04	1.34 ± 0.26 (3)	50.4	0.5	2.5
10	HD 169142	2.1×10^{-11}	≤ 2.31	≤ 0.002	≤ 0.002	≤ 0.05 (2)	344.9	2.5	1.9
11	HD 179218	1.2×10^{-9}	≤ 1.73	≤ 0.46	≤ 0.46	3.27 ± 0.25 (1)	364.7	0.3	0.6
12	IRS 48	4.0×10^{-10}	≤ 2.81	≤ 0.06	≤ 0.06	≤ 0.42 (4)	–	2.3	0.4
13	VV Ser	8.8×10^{-10}	3.38 ± 0.09	1.64 ± 0.04	≤ 0.55	35.6 ± 6.82 (5)	–	0.3	2.1
	T CrA[a]	6.1×10^{-10}	≤ 6.85	≤ 0.22	≤ 0.22	≤ 0.31 (4)	–	–	–

Table 5.3: OH P4.5 (1+,1−) doublet measurements. All errors are 1σ. An upper limit is determined using $1\sigma \cdot 30$ km s^{-1} for sources with no detection. The 1σ level is calculated based on the standard deviation from 2.930 - 2.936 μm for sources with non-detections of OH and H$_2$O, 2.928 - 2.934 μm for sources with an OH detection and a non-detection of H$_2$O, and 2.930 - 2.934 μm for sources with detections of both OH and H$_2$O. The upper limit calculation is determined the same as in Fedele et al. (2011) for consistency.The flux density is taken at 2.94 μm and is estimated at a value between the flux density in the Johnson:K and Johnson:L filters by a linear fit to the two data points. References for CO emission: (1) van der Plas et al. (2015); (2) Troutman (2010); (2) Brittain et al. (2007); (4) Brown et al. (2013); (5) Blake & Boogert (2004)

^{a}T CrA lacked IRAS photomoetric observations so it is not included on Figure 5.11.

luminosity. OH equivalent width is determined by calculating the equivalent width across the entire doublet, then dividing by 2. Upper limits are defined as $1\sigma \cdot 30$ km s^{-1}, where σ is the standard deviation determined from the noise in the continuum. Equivalent width errors are determined by adding the per pixel noise in quadrature across the emission feature.

5.3.1 Detections

In order to determine the emitting region of OH, we find fits to CO emission when available. Any differences in distance estimates which change stellar properties are taken into account. We assume the molecular emission to be co-spatial and at a similar temperature based on previous studies of OH and CO emission (Brittain et al., 2016). All OH modeling assumes the gas to be in Keplarian rotation in the circumstellar disk. The inclination angle of the disk is found from the literature and presented in Table 5.2. H_2O emission models assume that the gas is optically thin and in local thermodynamic equilibrium (LTE). The H_2O model spectrum is scaled such that the model equivalent width matches the equivalent width of emission between 2.927-2.930 μm for sources with detections. For non-detections, the model is scaled to match the upper limit reported in Table 5.3. The water model makes use of the BT2 water line list (Barber et al., 2006)

HD 95881: van der Plas et al. (2015) find a best fit of $R_{\mathrm{in}} = 2$ au and $R_{\mathrm{out}} = 35$ au for CO emission coming from HD 95881. van der Plas et al. (2015) place the CO rotational temperature at 850^{+400}_{-200} K for the $\nu = 1 \rightarrow 0$ transitions they observe. Figure 5.1 presents the OH P4.5 (1+, 1−) emission. Model fits to the emission are presented in Figure 5.2. We find that parameters derived in van der Plas et al. (2015) for CO match the OH emission profile.

We look at temperature values of 650 K, 850 K, and 1250 K to create the model spectra for H_2O emission while also assuming that the molecular emission is co-spatially located. The different temperatures only change the relative strengths of the different transitions in the model spectrum. We are unable to constrain the temperature of the water emission due to the lack of a detection, however, the range of temperatures investigated produce a spectrum that is consistent with the observed spectrum. Based on the upper limits of the water emission presented, it is unlikely further integration time would produce a significant detection from HD 95881.

HD 97048: van der Plas et al. (2015) find a best fit of $R_{\mathrm{in}} = 11$ au and $R_{\mathrm{out}} = 60$ au. van der Plas et al. (2015) place the CO rotational temperature at 350^{+350}_{-125} K for the $\nu = 1 \rightarrow 0$ transitions they observe. The observations of OH P4.5 emission are presented in Figure 5.3. Model
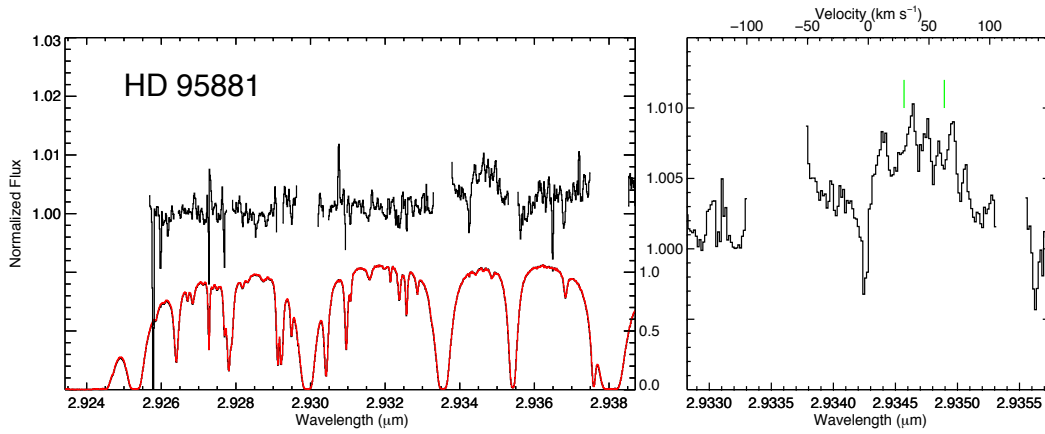
Figure 5.1: OH P4.5 (1+, 1−) emission line observed from HD 95881. We find that the OH P4.5 emission is Doppler shifted 22 km s^{-1} from the rest wavelength.
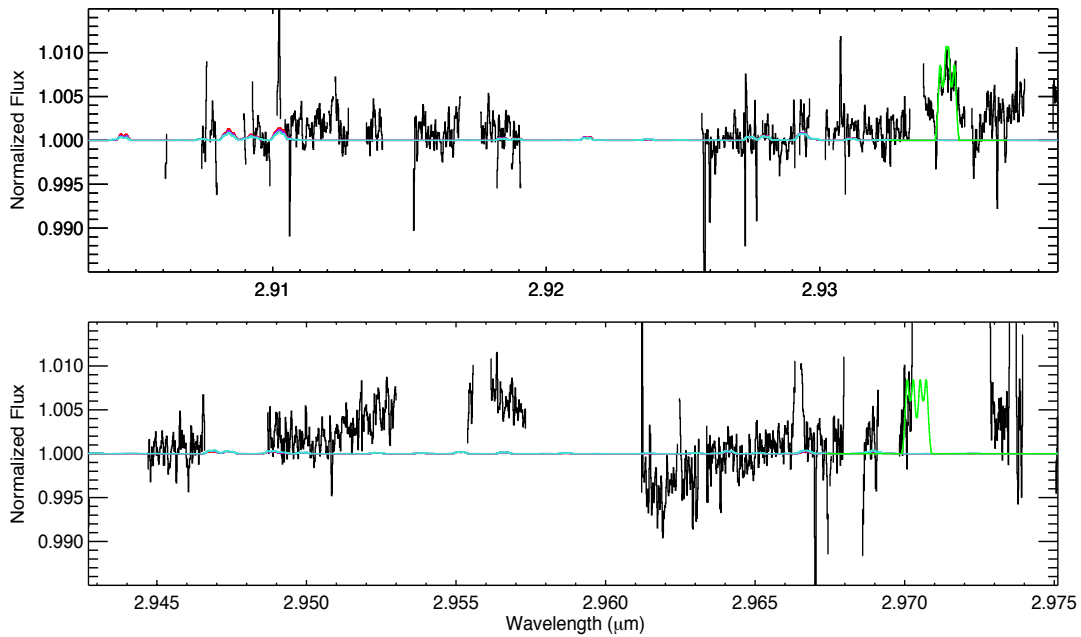

Figure 5.2: Rovibrational water emission lines observed from HD 95881. OH model profiles are shown in green. The red water emission model corresponds to a gas temperature of 650 K, purple corresponds to a temperature of 850 K, and turquoise corresponds to a temperature of 1250 K.
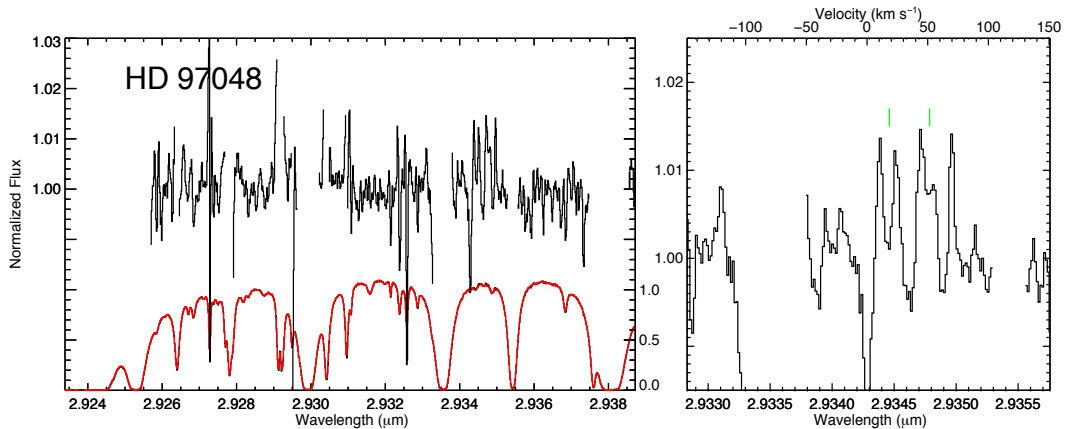
Figure 5.3: OH P4.5 (1+, 1−) emission line observed from HD 97048. We find that the OH P4.5 emission is Doppler shifted 18 km s^{-1} from the rest wavelength.

fits to the OH emission are presented in Figure 5.4. As with HD 95881, the derived disk parameters for the CO emission match the observed OH emission profile. HD 97048 observations have a lower signal-to-noise ratio than other sources with detections in this study. As a result, the OH detection is only at the 2σ level.

We look at temperature values of 350 K, 700 K, and 1000 K to create the model spectra for H_2O emission. The H_2O model indicates water could be present, however, we are unable to claim a detection due to the noise. The modeled water emission located near 2.91 μm could be present in observations if they are made in such a manner that they are shifted considerably from the telluric emission in that region of the spectrum or if observing conditions are drier such that the telluric features are weaker.

HD 104237: van der Plas et al. (2015) find a best fit of $R_{\rm in} = 0.2$ au and $R_{\rm out} = 1.5$ au for CO emission. The OH P4.5 emission is presented in Figure 5.5. The best fit model is shown in Figure 5.7. This geometry reproduces the line profile well.

Since no estimate of a temperature can be found in the literature, models for T = 1000 K, 2000 K, and 3000 K are computed and scaled to match the H_2O luminosity we find (Table 5.3). Higher temperatures lead to more transitions to appear in the model spectrum adding complexity. The prominent features at 2.91 and 2.93 μm are still the strongest features in each temperature model. The best fit to the observed water emission between 2.927-2.93 μm is produced by the cooler temperature (red) model as the transitions near 2.93 are stronger than those around 2.927. However,
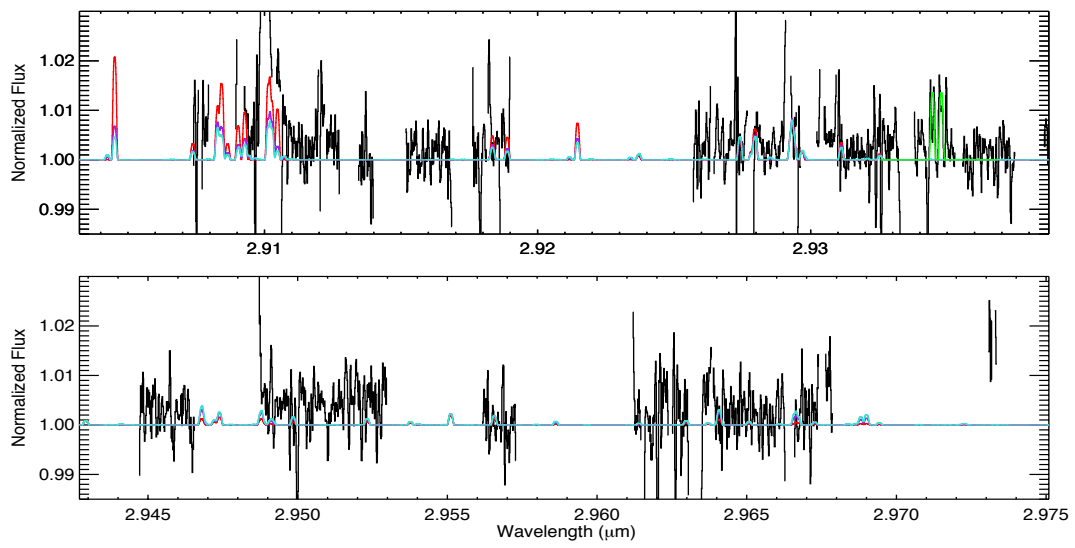
Figure 5.4: Rovibrational water emission lines observed from HD 97048. OH model profiles are shown in green. The red water emission model corresponds to a gas temperature of 350 K, purple corresponds to a temperature of 700 K, and turquoise corresponds to a temperature of 1000 K.
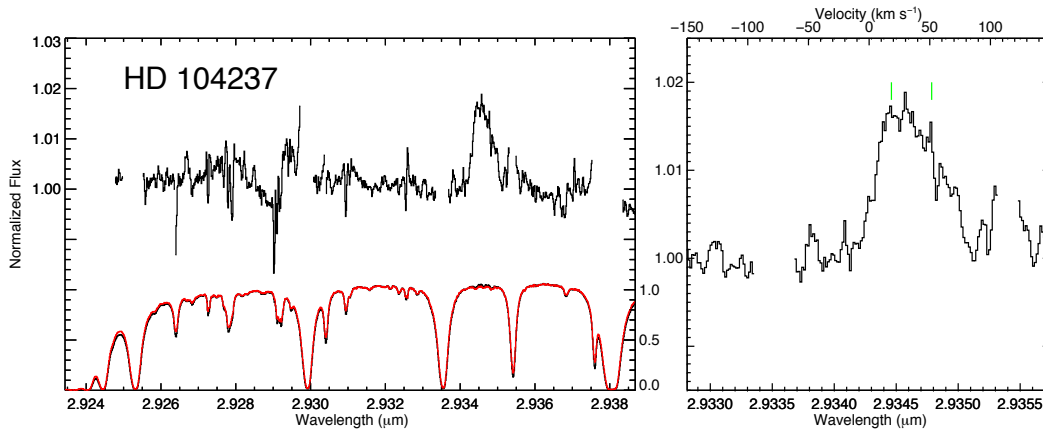
71

Figure 5.5: OH P4.5 (1+, 1−) emission line observed from HD 104237. We find that the OH P4.5 emission is Doppler shifted 18 km s^{-1} from the rest wavelength.

the higher temperature model appears to better reproduce the structure observed near 2.965 μm.

HD 163296: There are no estimates of the emitting region of molecular emission from HD 163296, so we perform a rough fitting of the OH profile. Our results give an emission region with $R_{\rm in} = 0.9$ au and $R_{\rm out} = 10$ au. Figure 5.7 shows the observed OH P4.5 emission and Figure 5.8 presents model fits to the OH emission.

We report a detection of H_2O emission from the disk of HD 163296. As no estimate of the NIR molecular gas temperature can be found in the literature, we look at temperatures of 1000 K, 2000 K, and 3000 K in Figure 5.8. The higher temperature models appear to reproduce the emission near 2.91 μm and 2.93 μm. The expected emission near 2.965 μm based on the model spectrum appears to fall in telluric absorption features that are not strong enough to be removed in analysis, but still impact the observed spectrum.

VV Ser: We do not find previously reported fits to molecular emission from VV Ser. A rough fitting gives $R_{\rm in} = 2$ au and $R_{\rm out} = 10$ au. Figure 5.9 presents the OH P4.5 emission feature with the best fit model profile presented in Figure 5.10. Some emission in the blue wings of the doublet overlaps a telluric absorption feature.

Modeling of the potential H_2O spectrum from VV Ser looks at temperatures of 1000 K, 2000 K, and 3000 K. We do not see evidence of any water emission at any temperature in the spectrum and we are unable to constrain the temperature of the gas in VV Ser from these observations.

Figure 5.11 presents the Group I/Group II designation for the sources in this study. ID

Figure 5.6:   Rovibrational water emission lines observed from HD 104237. OH model profiles are shown in green. The red water emission model corresponds to a gas temperature of 1000 K, purple corresponds to a temperature of 2000 K, and turquoise corresponds to a temperature of 3000 K.
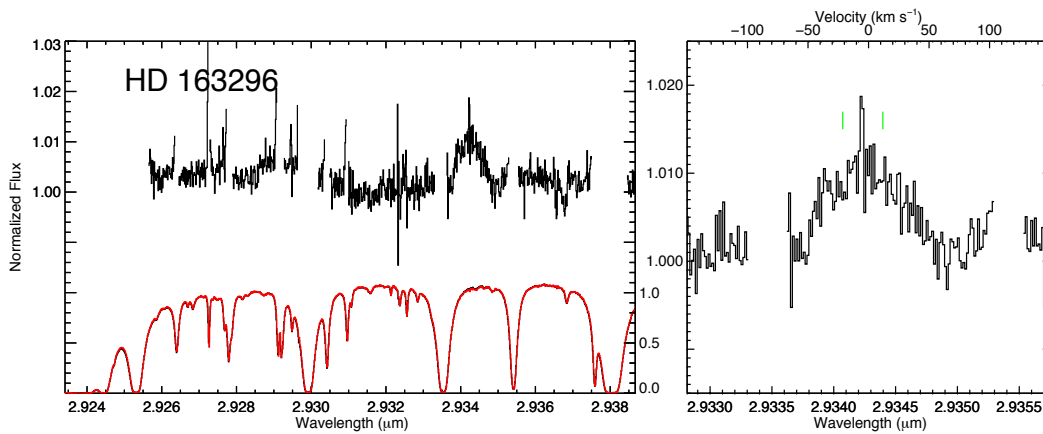
Figure 5.7:   OH P4.5 $(1+, 1-)$ emission line observed from HD 163296. We find that the OH P4.5 emission is Doppler shifted -18 km s^{-1} from the rest wavelength.
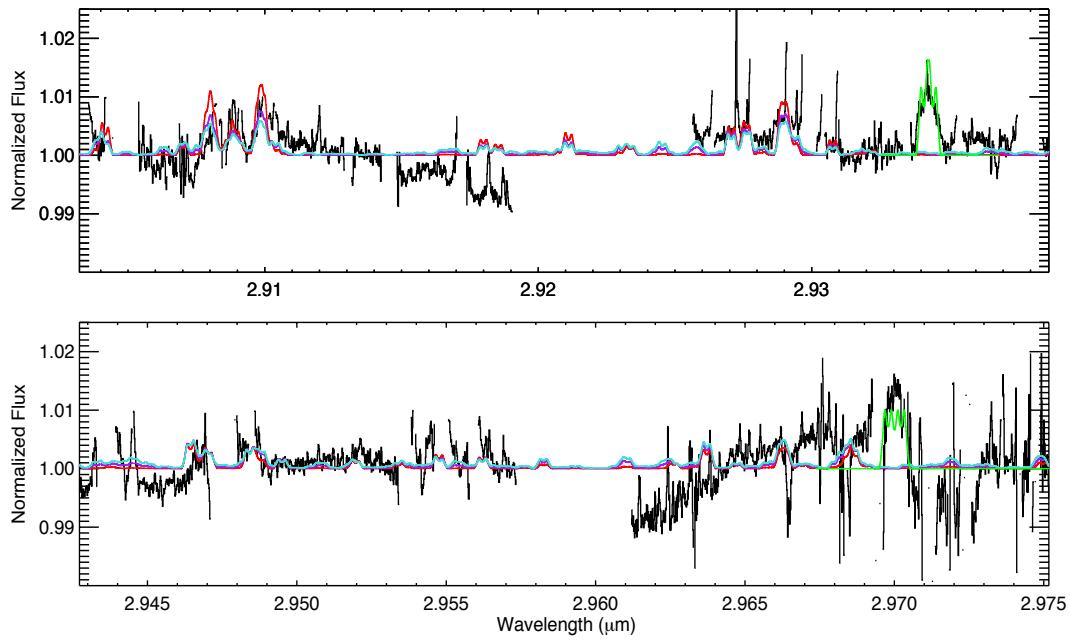
Figure 5.8: Rovibrational water emission lines observed from HD 163296. OH model profiles are shown in green. The red water emission model corresponds to a gas temperature of 1000 K, purple corresponds to a temperature of 2000 K, and turquoise corresponds to a temperature of 3000 K.
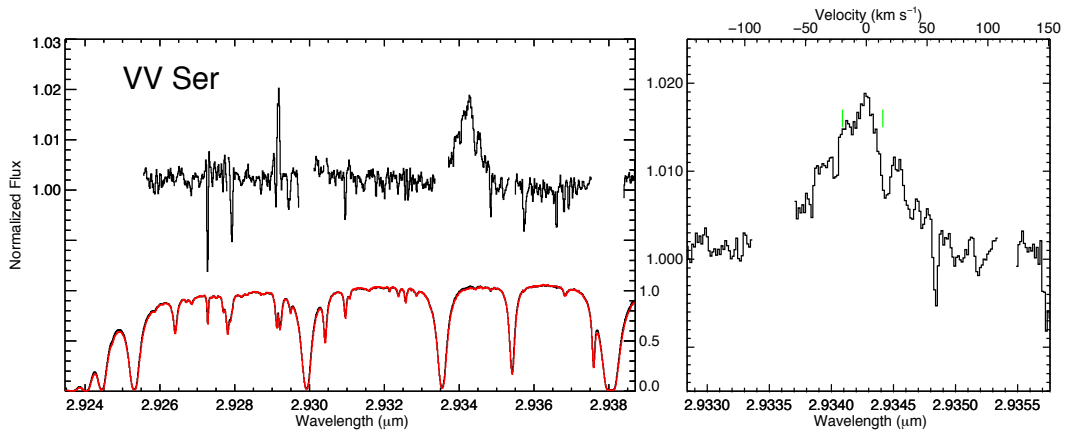
Figure 5.9: OH P4.5 (1+, 1−) emission line observed from VV Ser. We find that the OH P4.5 emission is Doppler shifted -20 km s^{-1} from the rest wavelength.
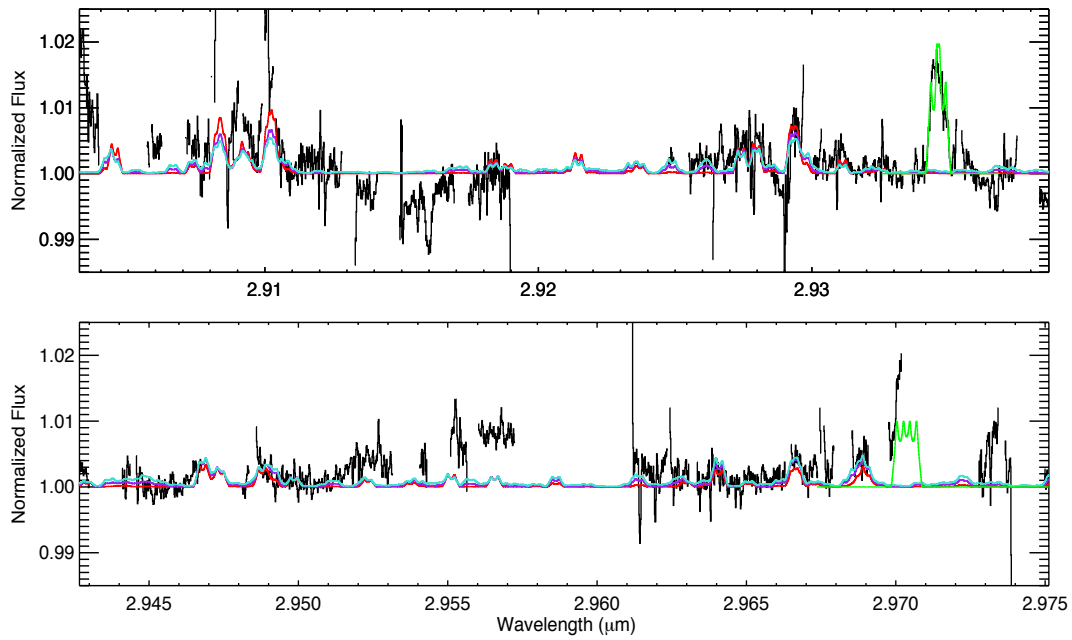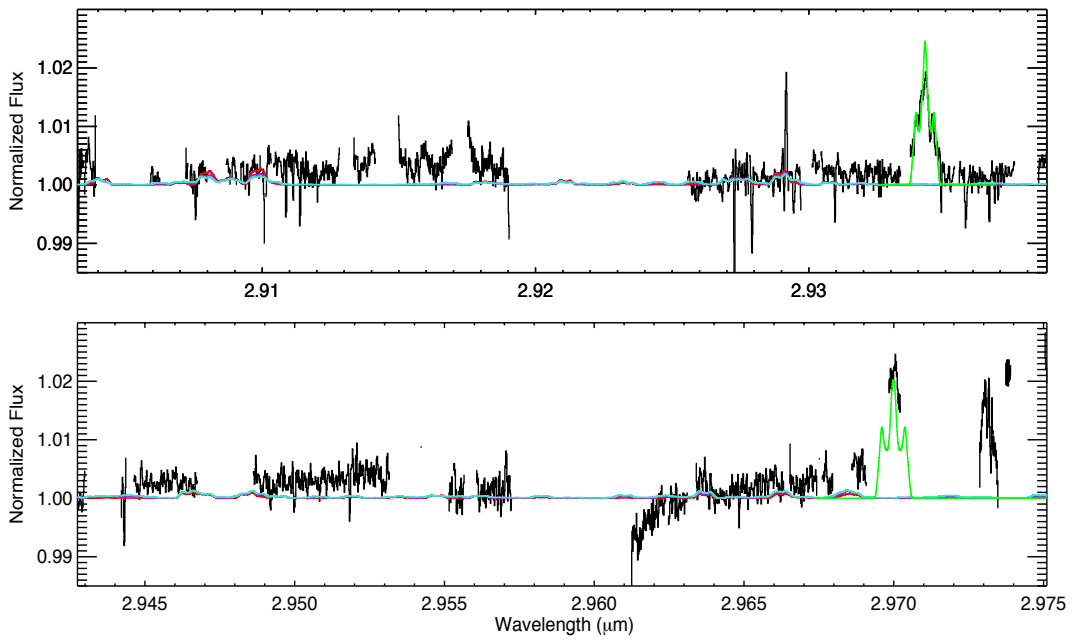
Figure 5.10: Rovibrational water emission lines observed from VV Ser. OH model profiles are shown in green. The red water emission model corresponds to a gas temperature of 1000 K, purple corresponds to a temperature of 2000 K, and turquoise corresponds to a temperature of 3000 K.
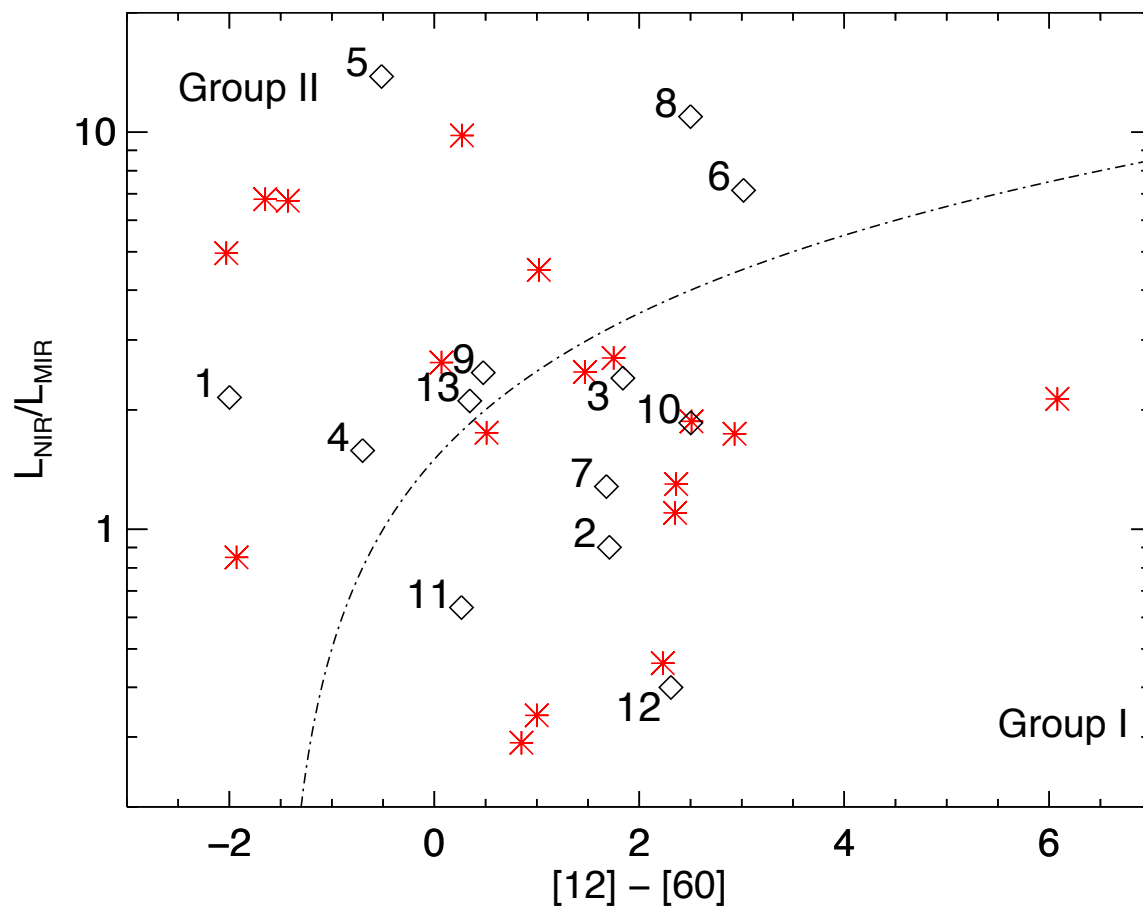
Figure 5.11: Group designation per van Boekel et al. (2005). Sources from Brittain et al. (2016) are plotted as red asterisks. New sources are symbolized by black diamonds and labeled by their corresponding ID number as shown in Table 5.3.

numbers for the sources are found in Table 5.3. HAeBes are broken into two groups: Group I sources have flared disks and Group II sources have flat disks (Meeus et al., 2001). The group designation is determined in the same manner as in Brittain et al. (2016). van Boekel et al. (2005) define the dividing line as $L_{\mathrm{NIR}}/L_{\mathrm{MIR}} \leq$ [12]-[60] + 1.5 being Group I sources. $L_{\mathrm{NIR}}$ and L_{MIR} values are determined from integrating the luminosity from 1-5 μm and 12-60 μm, respectively. [12]-[60] color is determined from IRAS flux values as [12]-[60] $= -2.5\log(\mathcal{F}_{12}/\mathcal{F}_{60})$. We include the sources from Brittain et al. (2016) in Figure 5.11 as red asterisks. There are three sources in both this study and Brittain et al. (2016): HD 135344B, HD 141569, and HD 179218. $L_{\mathrm{NIR}}/L_{\mathrm{MIR}}$ for HD 179218 is determined to be higher in this survey as compared to Brittain et al. (2016). This study looks at 7 Group I sources and 6 Group II sources.

Figure 5.12 is an updated version of Figure 3 from Brittain et al. (2016). The new sources from this study are shown as turquoise points. HD 101412 is presented as a red diamond as in Figure 3 in Adams et al. (2019). The new data points follow a similar trend as found in Brittain et al. (2016). The disks associated with holes in their inner disks ("transition" disks) tend to have weaker molecular emission and make up the majority of non-detections of OH and CO emission in this study.

Figure 5.13 shows the relationship between L_{OH} and $L_{\mathrm{H_2O}}$. It is an updated version of Figure 10 from Adams et al. (2019). Most of the new data are non-detections of both OH and H_2O emission and are not included in Figures 5.13 - 5.17. Both new detections of H_2O, along with HD 97048, show a similar relationship as the T Tauri stars presented with a ratio of about $L_{\mathrm{OH}}/L_{\mathrm{H_2O}}$ ≈ 0.5. This is at odds with most HAeBe sources with OH detected which show $L_{\mathrm{OH}}/L_{\mathrm{H_2O}} > 1$.

The potential connection between inclination angle and $L_{\mathrm{OH}}/L_{\mathrm{H_2O}}$ is investigated in Figure 5.14. One potential explanation of the detection of water vapor emission from HD 101412 was the combination of high inclination angle coupled with a dust depleted inner disk. We look at both T Tauri stars (data taken from Banzatti et al. 2017) with both OH and H_2O detections at 2.94 μm. We do not include HAeBe sources with non-detections in our figures. We do not observe a correlation between $L_{\mathrm{OH}}/L_{\mathrm{H_2O}}$ and inclination angle in either T Tauri stars or HAeBe stars.

Figure 5.15 presents $L_{\mathrm{OH}}/L_{\mathrm{H_2O}}$ vs. effective temperature (T_{eff}). There is an observed increase in $L_{\mathrm{OH}}/L_{\mathrm{H_2O}}$ as you move to higher T_{eff}, which is analogous to looking at stars with stronger ultraviolet radiation fields. Modeling of the abundance of molecular species' response to increased far-ultraviolet radiation from the central star (Ádámkovics et al., 2016; Najita & Ádámkovics, 2017)
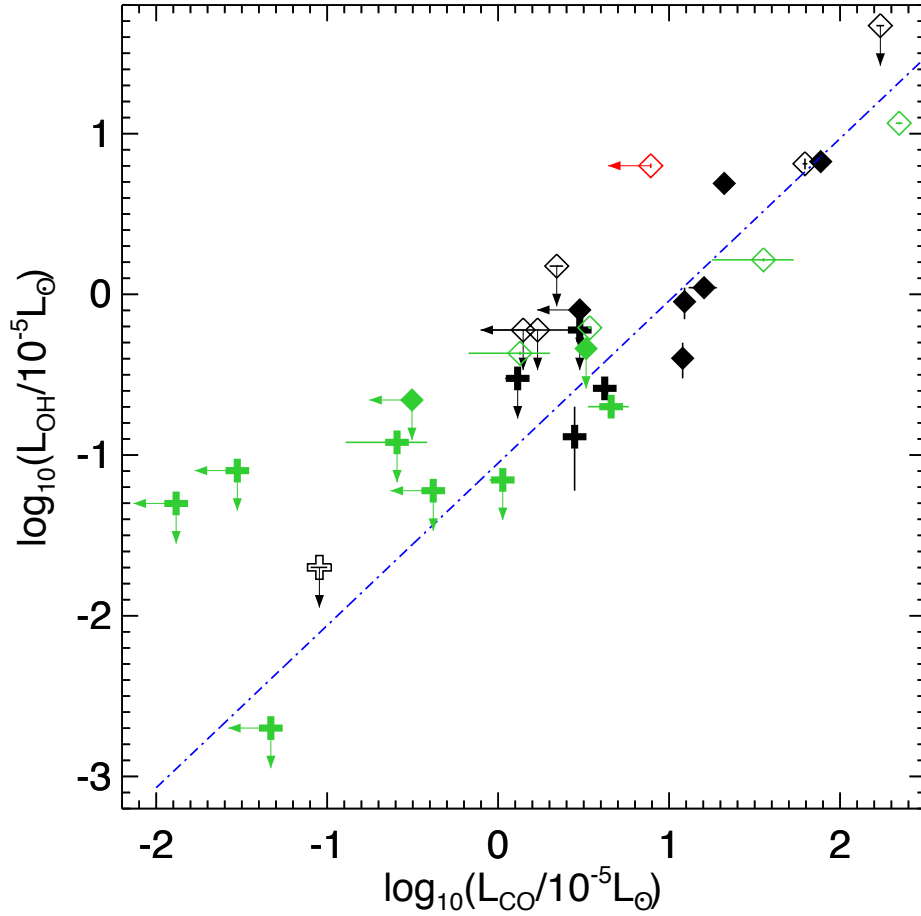
Figure 5.12: Adapted from Brittain et al. (2016). HD 101412 has been added and is plotted in red. Group I HAeBe stars are marked as filled points. Group II HAeBe stars are marked as open symbols. The disks that have been observed to have an optically thin inner disk are labeled with "plus" signs. Disks without such optically thin regions are labeled with diamonds. The dark blue dotted-dashed line is a linear least-squares fit to the detections, not including HD 101412. The green points are new sources added from this study.
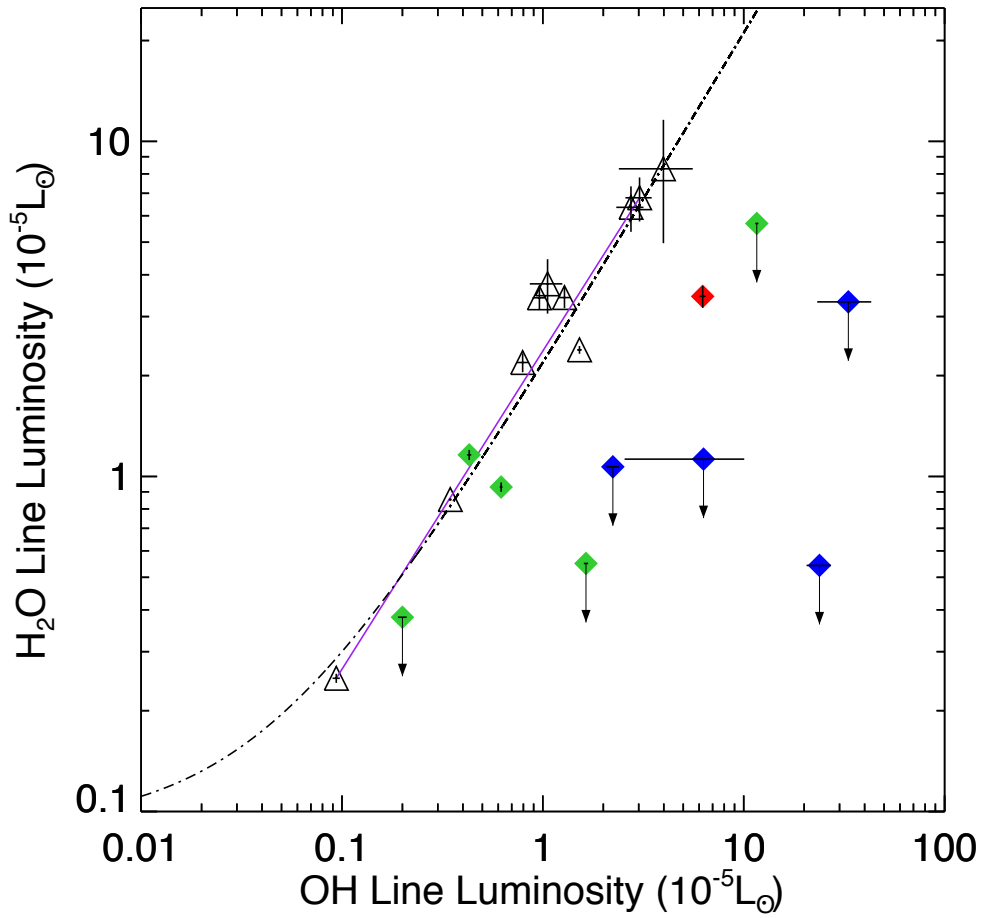
Figure 5.13: Updated Figure 10 from Adams et al. (2019). T Tauri stars are represented by open triangles with the stellar parameters taken from Banzatti et al. (2017). Blue diamonds represent HAeBe sources with previously observed OH and H_2O luminosities or upper limits. Green diamonds represent HAeBe observations from this work. HD 101412 is plotted as a red diamond. All errors and upper limits are 1σ.
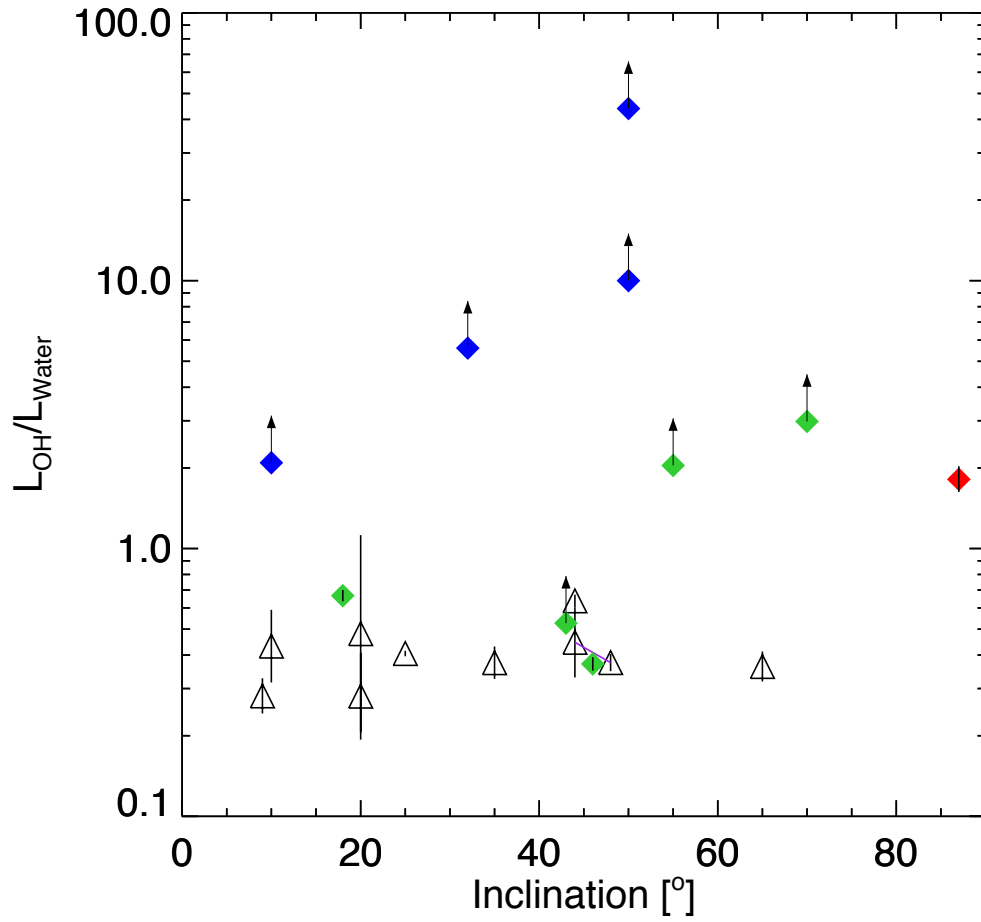
Figure 5.14: Plot of $L_{\text{OH}}/L_{\text{H}_2\text{O}}$ ratio vs. inclination angle. Refer to Figure 5.13 for a guide to what each symbol represents.
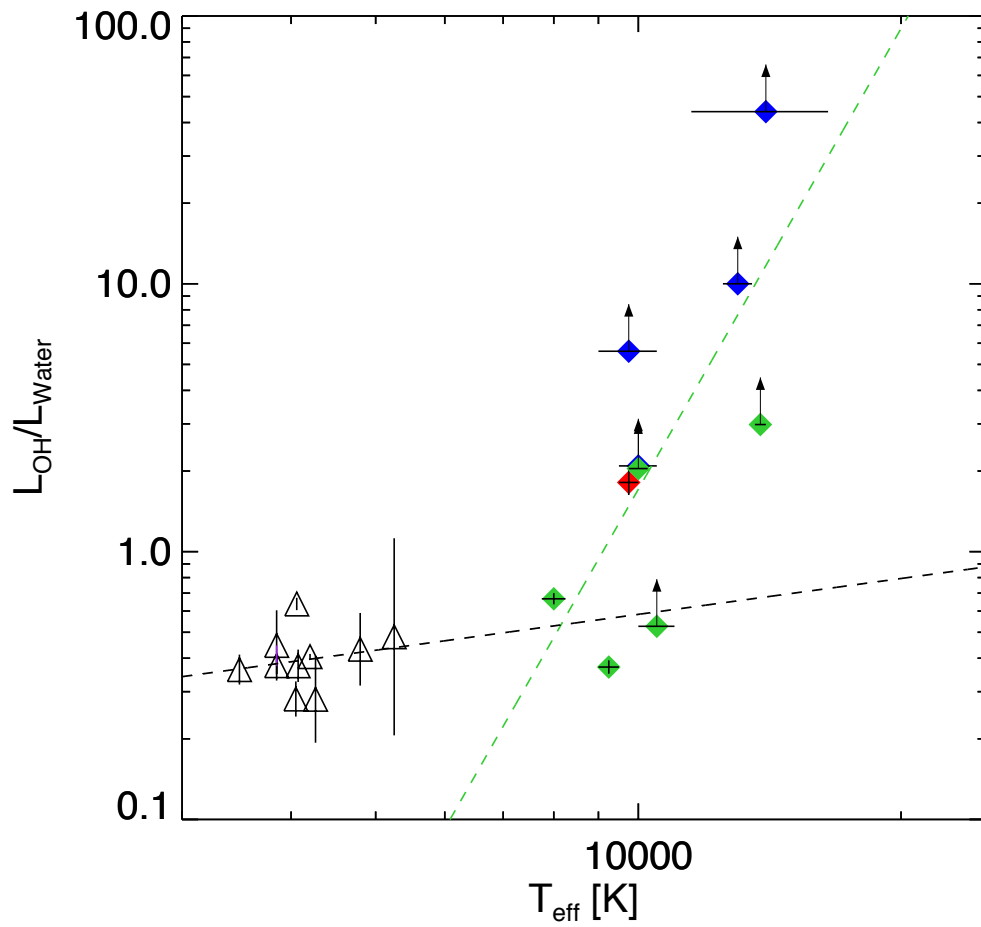
Figure 5.15: Plot of L_{OH}/L_{H_2O} ratio vs. T_{eff}. The black dashed line is the best fit line for T Tauri stars and the green is the best fit line for HAeBe stars. Correlation coefficients for each fit are $R^2 = 0.07$ and $R^2 = 0.52$ for the T Tauri and HAeBe data, respectively. Refer to Figure 5.13 for a guide to what each symbol represents.

shows that H_2O molecules are photodissociated, resulting in a larger column of OH gas in the upper atmosphere of the circumstellar disk. This would explain the observed increase in L_{OH}/L_{H_2O} as you move to higher T_{eff}. The two new detections of H_2O emission from HD 104237 and HD 163296 show stronger H_2O emission compared to OH which is more consistent with T Tauri stars. Figure 5.15 includes the best fit line for both T Tauri (in black) and HAeBe (in green) stars. The correlation coefficient for the T Tauri data is low ($R^2 = 0.07$) as L_{OH}/L_{H_2O} is consistent across the range of temperatures for the sources observed. The best fit line for HAeBes has a higher correlation coefficient ($R^2 = 0.534$) and has the form

$$\log(\frac{L_{OH}}{L_{H_2O}}) = (5.7 \pm 1.9)\log(T_{eff}) - (22.6 \pm 7.6). \tag{5.1}$$

The best fit lines are determined via a linear regression model which does not take into account lower limits on the data points.

Figure 5.16 shows the relationship between L_{OH}/L_{H_2O} and accretion rate ($\dot{M}_{acc}$). Accretion of gas and dust onto the stellar surface results in an increase in ultraviolet radiation. Typically, accretion rates are measured by looking at the excess emission in the Balmer decrement (longward of 3700 Å). We show that, as L_{OH}/L_{H_2O} increases with T_{eff}, L_{OH}/L_{H_2O} also increases with $\dot{M}_{acc}$. One implication of higher accretion rates is that more material exists in the inner disk. This would increase the column of gas available to produce molecular emission. If the dust continuum is not too great, this would allow for brighter molecular emission. Of the two new detections of H_2O emission, the accretion rates tend to be at the upper end of the T Tauri sources and in the middle of the pack with respect to HAeBes. Figure 5.16 includes the best fit line for both T Tauri (in black) and HAeBe (in green) stars. The correlation coefficient for the T Tauri data is low ($R^2 = 0.06$) as L_{OH}/L_{H_2O} is consistent across the range of accretion rates for the sources observed. The best fit line for HAeBes has a higher correlation coefficient ($R^2 = 0.72$) and has the form

$$\log(\frac{L_{OH}}{L_{H_2O}}) = (0.5 \pm 0.1)\log(\dot{M}_{acc}) - (3.4 \pm 0.9). \tag{5.2}$$

The best fit lines are determined via a linear regression model which does not take into account lower limits on the data points.

Finally, Figure 5.17 shows L_{OH}/L_{H_2O} vs. the gas-to-dust ratio as determined from Kama
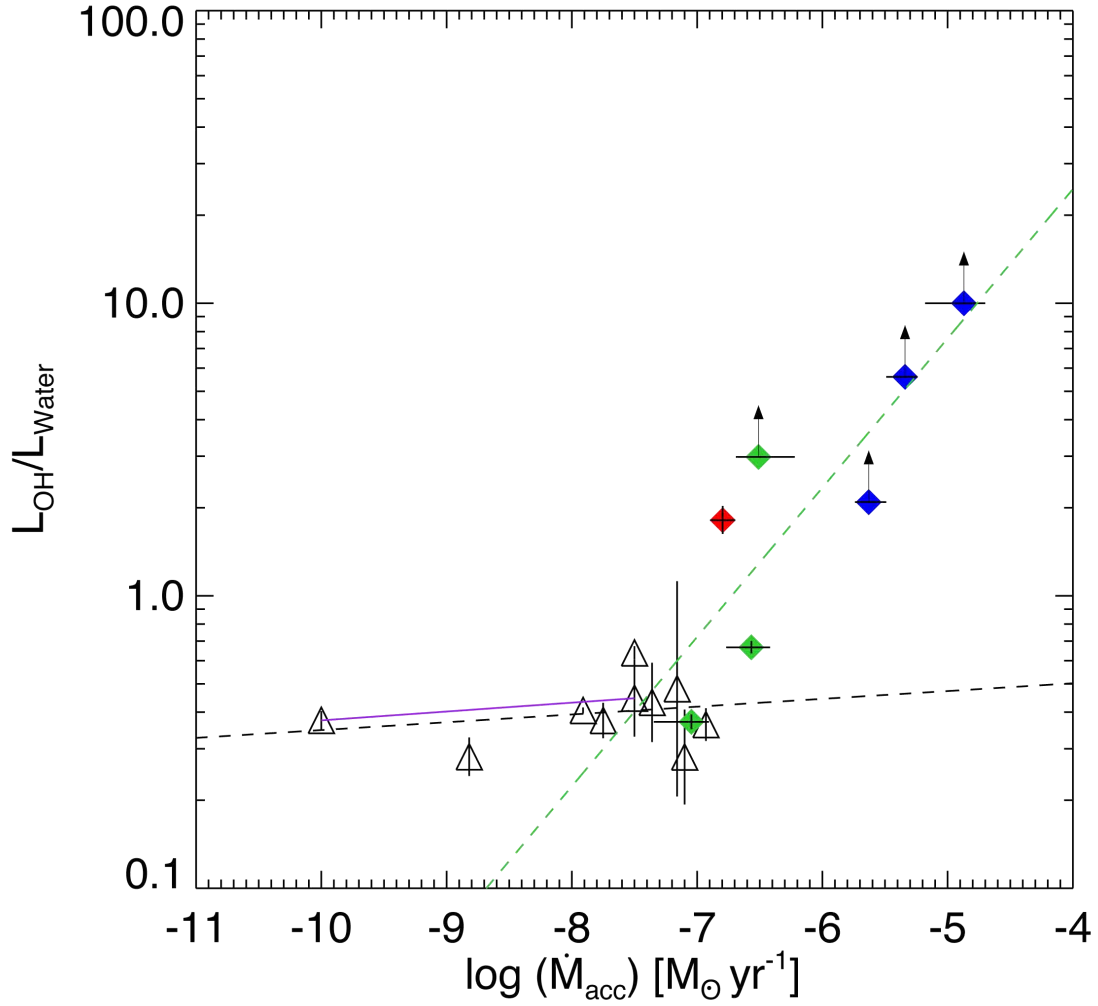
Figure 5.16: Plot of L_{OH}/L_{H_2O} ratio vs. $\dot{M}_{acc}$. The black dashed line is the best fit line for T Tauri stars and the green is the best fit line for HAeBe stars. Correlation coefficients for each fit are $R^2 = 0.06$ and $R^2 = 0.72$ for the T Tauri and HAeBe data, respectively. Refer to Figure 5.13 for a guide to what each symbol represents.
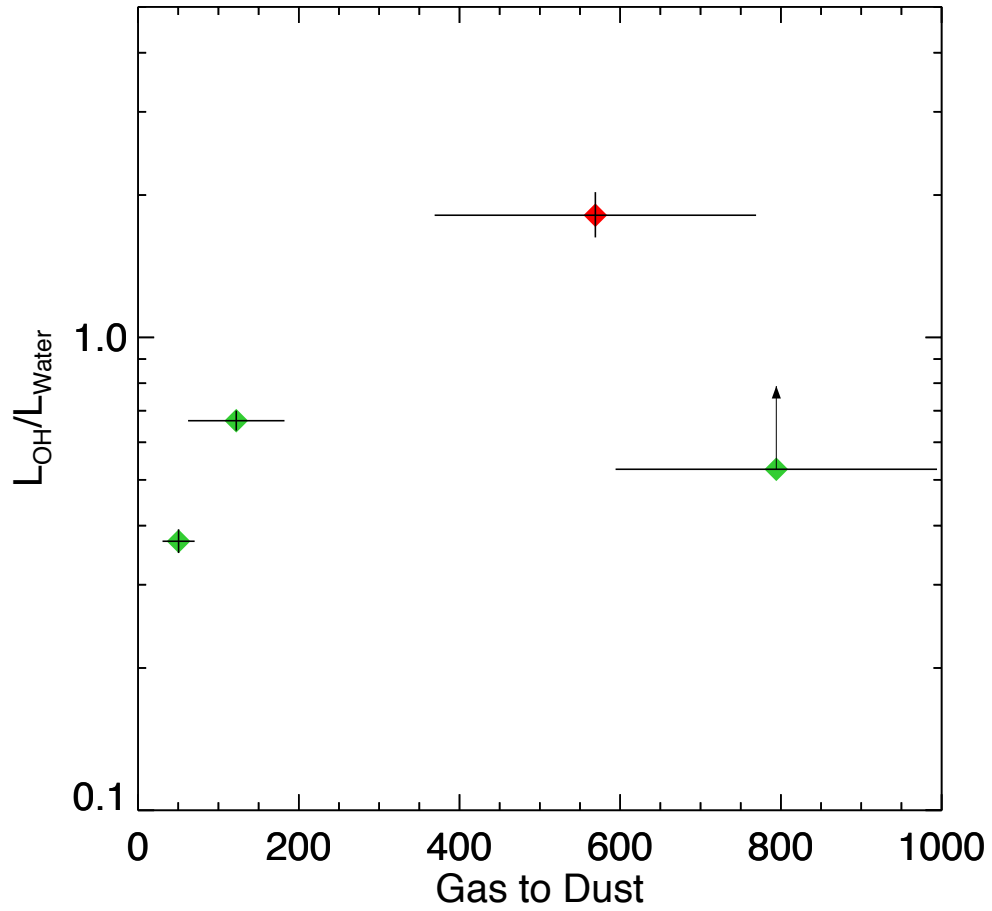
Figure 5.17: Plot of $L_{\mathrm{OH}}/L_{\mathrm{H_2O}}$ ratio vs. gas-to-dust ratio, as measured by Kama et al. (2015). Refer to Figure 5.13 for a guide to what each symbol represents.

et al. (2015). Only a handful of sources are investigated in both studies, and no T Tauri sources were included in Kama et al. (2015). As a result, not much information can be gained from this plot as the majority of sources have only upper limits of OH and H_2O. Of the three sources with detections of both OH and H_2O emission, there does appear to be an increase of L_{OH}/L_{H_2O} as more dust is depleted from the inner circumstellar disk. The one source with L_{OH}/L_{H_2O} less than 1 and a higher gas-to-dust ratio is HD 97048. The OH detected in this source is weak and the spectrum has a low signal-to-noise ratio. This decreases the L_{OH}/L_{H_2O}.

5.3.2 Non-detections

There are five sources in this study with no reported molecular emission; HD 100453, HD 141569, HD 169142, IRS 48, and T CrA. All sources minus T CrA all have optically thin inner disks which point to cleared out holes in the inner disk. As these disks lack considerable amounts of molecular gas in their inner regions, they are expected to have weak to no observable molecular emission. This is confirmed in Figure 5.12 as the sources represented by "plus" signs are disks with observed holes based on a lack of NIR excess in their spectral energy distributions.

HD 141569 and HD 169142 are both λ Boö stars (Folsom et al., 2012), however, both are also transition disk indicating not much material resides close to the central star. Adams et al. (2019) connected HD 101412's status as a λ Boö star as a possible contributing factor to the detection of water vapor emission from the inner disk. The λ Boö phenomenon is possibly an indication of selective accretion of gas onto the central star as opposed to dust (Venn & Lambert, 1990; Waters et al., 1992). This would lead to an over abundance of volatile elements (C, O, and N) and an under abundance of refractory elements (Fe, Mg, and Si) in the stellar photosphere relative to solar values. As early-type stars lack outer convective layers, this abundance pattern would persist for a while. This could explain the lack of detection of molecular emission from thee two sources.

5.4 Discussion & Conclusions

The OH P4.5 (1+, 1−) emission lines presented in this study support previous observations indicating that OH and CO emission tend to originate from the same location in the circumstellar disk (Brittain et al., 2016; Banzatti et al., 2017). This is unsurprising as fundamental rovibrational transitions of each molecule have comparable energies. Observing higher energy transitions of OH

would provide some additional constraints on the gas temperature in the inner regions of the circumstellar disk. It would also allow for better constraints on the excitation mechanism for OH gas. The NIR spectrum of water vapor emission is more complicated than those of CO and OH due to the fact that water is a tri-atomic molecule. Therefore, it is difficult to pick out individual transitions even when water emission is observable.

The molecular emission of HD 104237 is similarly narrow as that observed from HD 101412, however, the observed inclination angle is much lower (18° for HD 104237 vs. 86° for HD 101412). It is not known if HD 104237 is a λ Boö star, nor the gas-to-dust ratio. The accretion rate is high (log $\dot{M}_{\mathrm{acc}}$ = -6.57$^{+0.15}_{-0.20}$; Fairlamb et al. 2015) which is similar to the accretion rate of HD 101412. This indicates that a large amount of material exists in the inner disk of HD 104237. HD 104237 is also a magnetic star (Donati et al., 1997; Järvinen et al., 2019) with a slow rotation rate ($v\sin i$ = 8 km s^{-1}). This is also consistent with HD 101412 ($v\sin i$ = 3 kms^{-1}; Hubrig et al. 2011).

HD 163296 is chemically normal (Folsom et al., 2012) and does not show evidence of a magnetic field (Alecian et al., 2013). Variable CO emission has been observed from HD 163296, possibly due to a disk wind (Hein Bertelsen et al., 2016b). We do not have more high resolution NIR observations of OH in HD 163296 to determine if it also shows variability on the same timescales as CO, however, our assumption that the emission originates from a disk of gas in Keplerian orbit reproduces the observed line profile without an additional component from an outflow. It could be that the material launched from the disk does not contain enough OH for the emission to be detectable as the CO emission is a factor of $\sim$10 stronger when comparing the line-to-continuum ratio (Hein Bertelsen et al., 2016b). HD 163296 also has a relatively low gas-to-dust ratio as reported by Kama et al. (2015). This clouds the picture that water emission should not be detected until a large portion of the dust in the inner disk is depleted.

Fedele et al. (2013) report warm OH and H_2O emission in the far-infrared around both HD 104237 and HD 163296. The far-infrared emission traces gas further out in the disk, likely beyond 30 au, and possibly from deeper in the disk. Our study, coupled with the results of Fedele et al. (2013), show that water vapor can exist in both the inner and outer regions of the HAeBe circumstellar disk.

We present five new detections of OH P4.5 (1+, 1−) emission and two new H_2O emission from the disks of HAeBe stars. This increases the population of NIR OH detections to 15 out of 31 (48%) HAeBe stars studied, and 3 total detections of NIR H_2O emission. Our observations

support previous reports that OH and CO emission are located co-spatially. We are able to show that the relative strength of OH emission to H_2O emission increases as stellar effective temperature increases, providing further evidence that ultraviolet radiation from the central star is the likely cause for the lack of NIR H_2O emission from HAeBes. More high resolution NIR observations taken with instruments (i.e., CRIRES+ on ESO's VLT or iShell on NASA's Infrared Telescope Facility) that provide a higher spectral dispersion should provide better insights to the gas temperature and excitation processes of OH emission from HAeBe stars. These instruments will allow for concurrent observations of multiple rovibrational transitions.

Chapter 6

Hydrogen emission origins within Herbig Ae/Be stars using spectro-astrometry

6.1 Introduction

Hydrogen recombination emission observed from young stellar objects (YSOs) has been connected to their accretion and outflow properties (Kraus et al., 2008b). Based upon the line profiles observed for H I recombination emission, it is known that the gas originates from a region near the central star, too close to be spatially resolved, even with the most powerful telescopes available. It is paramount to understand the formation processes for H I emission as it pertains to mass loss from the circumstellar environment and provides a probe of the star-disk interaction region.

Lower mass (< 2 M$_\odot$) young stellar objects, known as T Tauri stars (TTS), have been extensively studied the past couple of decades. These studies have predicted through modeling (Shu et al., 1994) and shown via observations (Cabrit et al., 1990; Hartigan et al., 1995) a tight correlation between stellar accretion and mass-loss rates. Studies of H I emission lines in classical TTS and intermediate mass TTS have shown a correlation between hydrogen emission line luminosity, L_{HI}, and accretion luminosity, L_{acc}, (Muzerolle et al., 1998a; Calvet et al., 2004). This correlation suggests

that L_{HI} is dominated by accretion processes. The current paradigm for accretion in TTS is via magnetospheric accretion (MA) (Bertout et al., 1988; Bouvier et al., 2007). The magnetosphere from these stars truncate the circumstellar disk, and the field lines channel material into funnel flows that fall ballistically onto the stellar surface. This results in bright areas on the surface due to the shock from the infalling material. Observed emission line profiles have been reproduced by MA models (Muzerolle et al., 1998c,b). However, it is also possible that H I emission could arise from outflow activity (Whelan et al., 2004; Kurosawa et al., 2006; Beck et al., 2010).

Higher mass (2 - 8 $M_\odot$) young stellar objects, known as Herbig Ae/Be stars (HAeBes), have similarly had the L_{HI} and L_{acc} correlation investigated (Garcia Lopez et al., 2006; Donehew & Brittain, 2011; Mendigutía et al., 2013, 2015b; Fairlamb et al., 2015, 2017). However, as HAeBes are more massive, they do not have convective outer regions (Palla & Stahler, 1993), thus they are not expected to have strong magnetic fields. Alecian et al. (2013) performed a spectro-polarmetric study in order to determine the magnetic field strength of HAeBes. They observed 70 sources and only found 5 to be magnetic. HAeBes are generally faster rotators compared to TTS. This would shink the size of the co-rotation radius. MA cannot occur outside of the co-rotation radius (Shu et al., 1994), thus the magnetospheres of HAeBes required to drive MA would be smaller in volume than those required by TTS. HAeBes have been observed to emit X-ray radiation, which could be indicative of the presence of chromospheres (Skinner & Yamauchi, 1996; Stelzer et al., 2006) or shocked accretion flows confined by a magnetic field (Swartz et al., 2005). Guimarães et al. (2006) also detected redshifted absoprtion lines with velocities approaching free-fall velocities on to the stellar surfaces of HAeBes. Thus at least some HAeBes show evidence of MA (Fairlamb et al. (2015) report that 84 out of 91 HAeBe's Balmer excess can be modeled by MA).

Donehew & Brittain (2011) concluded that Brγ luminosity and L_{acc} in HAe stars show a similar correlation to TTS from Muzerolle et al. (1998a) and Calvet et al. (2004). However, the relationship appears to break as you get to earlier type HBe stars. This would imply a deviation in the physical processes creating the lines at the star-disk interface. Mendigutía et al. (2011) show that a MA shock model does not reproduce the Balmer excess observed in the hotter HBe stars in their study of Hα and [O I] 6300Å emission lines, indicating that the primary accretion method could differ between HAes and HBes.

Other studies provide evidence of a breakdown in the physical accretion processes of HAe and HBe stars. Vink et al. (2002) and Mottram et al. (2007) both use spectro-polarimetry to study

the circumstellar environments of HAeBes and measure the emitting regions of Hα. They both report that the Hα line becomes depolarized in the disks of HBe stars, while it is polarized in HAe disks. Difference in the linear polarization could be an indication of a transition from MA in the lower mass HAe stars to disk accretion in HBe stars (Vink et al., 2002). Mottram et al. (2007) extended their analysis to Hβ and Hγ and provided further evidence for similarities between TTS and HAes (MA) and a deviation to disk accretion in HBe stars.

More recently, Cauley & Johns-Krull (2014) observed He 1 λ10830 line profiles in a survey of 56 HAeBe stars. Their results show that HAe stars show similar signs of MA seen in TTS, whereas HBe stars exhibit signs not associated with MA. Cauley & Johns-Krull (2015) expanded this to other potential outflow tracers in HAeBe stars. They looked at optical emission lines and concluded the inner environments are not the same for HAe and HBe stars. Cauley & Johns-Krull (2015) suggest that the overall characteristics of the optical emission features point towards magnetically controlled accretion in HAe stars and boundary-layer accretion in HBe stars.

One challenge to determining the origins of H I emission lines is that most accretion models predict that the lines form near the stellar surface on milliarcsecond (mas), or sub-au, scales. Studies on the origins of H I emission lines have used spectro-interferometry to get measurements below the spatial resolution of the telescope used to make the observations. Kraus et al. (2008b) studied Brγ emission in HAeBe stars and concluded that the emission line was not a reliable tracer for accretion within these systems. Their sample only consisted of five sources, however, the data showed that the emitting region was consistent with extended sources, such as an outflow. This would imply that Brγ emission is more likely to be an indirect tracer of the accretion rate via accretion-driven mass loss. Eisner et al. (2009) also studied Brγ and determined that H I emission was arising from hot gas within the dust-sublimation radius of HAeBe disks. Recent work measuring the variability of Brγ indicated that the typical timescale variations on the order of nights to months or years (Eisner et al., 2015). The higher mass HBe stars in Eisner et al. (2015) showed variability on the shortest timescales which could trace outflows. Benisty et al. (2010) observed Brγ emission from the Z CMa binary system (consisting of a HBe star and FU Ori star). They determined that the Brγ was tracing a wind from within the dust sublimation radius of the HBe star. Mendigutía et al. (2015a) performed spectro-interferometry on the HBe star HD 100546 and determined that the Brγ emission was originating from within a Keplerian disk. Other studies of individual sources have also concluded that the Brγ emission arises from a compact region within the system and likely trace

outflows (Kraus et al., 2008b; Weigelt et al., 2011; Garcia Lopez et al., 2015, 2016; Hone et al., 2019).

6.1.1 Spectro-astrometry

Observations have angular resolution limitations based on the optical system in use. The theoretical limit for all systems is the diffraction limit,

$$\theta = \frac{1.22 \cdot \lambda}{Diameter}. \tag{6.1}$$

However, techniques have been implemented in order to achieve measurements below this theoretical limit. One such technique is spectro-astrometry (SA). SA is a combination of spectroscopy and astrometry. As the observations are made, the light is spread across the detector. The distribution of the light creates a profile known as the Point Spread Function (PSF). The PSF is fit using a Gaussian to determine the location of the center of the PSF in the detector. The centroid of the PSF can be determined to a high accuracy, giving a measurement of the center of light beyond the angular resolution of the instrument (Bailey, 1998b; Whelan & Garcia, 2008)

$$\sigma_{\mathrm{centroid}} = \frac{\mathrm{FWHM}}{2.3548 \cdot \mathrm{SNR}}. \tag{6.2}$$

Combining astrometry with spectroscopy provides information on how the center of light evolves across features in the spectrum. If a system has an emission feature in its spectrum, one can determine if the emission comes from an extended region in the system giving information on the physical processes that produce the observed emission.

The expected angular extent of emission originating from MA is on the order of the disk truncation radius, which for HAeBe stars is < 0.1 au, or < 0.7 mas, for the closest star-forming region (located at a distance of 140 pc). Use of SA will allow for ~ 0.1 mas fidelity in determining the center of light, and it can allow for the determination of H I emission origins within HAeBe star systems.

Previous SA measurements have provided access to information otherwise unresolvable with traditional observations. Close binary star systems have been detected using SA (Bailey, 1998a; Porter et al., 2004). Acke & van den Ancker (2006) studied [O I] 6300Å in HAeBe stars and

91

determined that the emission was forming from gas in a Keplerian disk rather than an outflow as in TTS. Pontoppidan et al. (2008) investigated molecular gas (CO) within protoplanetary disk gaps. They used high resolution, long-slit spectroscopy and were able to achieve a fidelity < 1 mas. Coupling the measurements with modeling, Pontoppidan et al. (2008) were able to constrain the basic geometric properties of the circumstellar disk. Pontoppidan et al. (2011) observed highly accreting young stellar objects using SA and determined that the CO emission was arising from gas in a smaller region than expected if it were in a Keplerian disk. Brittain et al. (2014) measured CO emission in HD 100546 and, using SA, determined the offsets detected in the emission line were likely caused by the presence of a circumplanetary disk orbiting at a distance of 12.5 au. Davies et al. (2010) used the Near-infrared Integral Field Spectrograph (NIFS; McGregor et al. 2003) on the Gemini South telescope to study Brγ emission within the outflow disk and envelope of the young stellar object W33A with SA. The team was able to achieve a resolution down to 0.1 mas by performing SA analysis on the Brγ emission line. Here we use SA to determine the origins of the hydrogen emission lines Paβ and Brγ within HAeBe systems.

We observe Paβ and/or Brγ emission lines in six HAeBe stars, presented in Table 6.1 with stellar parameters presented in Table 6.2. Section 6.2 discusses the observations, data reduction, and SA analysis. Section 6.3 presents the results from the observations and section 6.4 discusses the modeling to reproduce the observed emissions feature and SA offsets. Section 6.5 is the discussion on our results and the implications from the modeling, and section 6.6 concludes with how we plan to advance this study in the future.

6.2   Observations & Analysis

All data were obtained using Gemini/NIFS in queue mode. NIFS has a field of view of $3.''\times 3.''$ with a pixel size of $0.''043 \times 0.''103$ along the slit (x) and in the dispersion direction (y), respectively. NIFS provides intermediate spectral resolution of R = 5290 (56.7 km s^{-1}) in the K-band and R = 6040 (49.7 km s^{-1}) in the J-band. Observations made during the 2011A observing campaign looked at both Brγ and Paβ emission lines. Only one instrument position angle was used for the observations. Typical SA artifact removal procedures call for parallel/anti-parallel observations to be made, however, a model was used to remove the suspected primary source of artifacts (uneven slit illumination). Data from the 2015A observing run were obtained using 4

Star	Date	Band	Airmass	Exposures	Int. Time
HD 150193	20120706	J	1.85	6	360 s
	20120706	K	1.54	10	1007 s
	20150511	J	1.41	8	960 s
	20150519	J	1.49	8	960 s
HD 163296	20120409	J	1.43	10	200 s
	20150518	J	1.40	8	624 s
	20150519	J	1.40	8	624 s
HD 179218	21020608	J	1.08	6	360 s
	20120610	K	1.19	10	848 s
	20150509	J	1.08	16	2400 s
HD 250550	20130107	K	1.02	10	800 s
HD 259431	20130105	J	1.03	6	600 s
	20130106	K	1.40	11	1108 s
VV Ser	20120508	J	1.29	8	1920 s
	20120508	K	1.15	10	500 s
Standard Stars					
HIP 77111	20150511	J	1.09	2	50 s
	20150519	J	1.10	4	60 s
HIP 85391	20150518	J	1.49	4	100 s
	20150519	J	1.52	4	80 s
HIP 95793	20150509	J	1.10	8	80 s

Table 6.1: Observation information for sources included in this survey. Standard star observations were only made during the 2015 observing program. K-band observations were made without corresponding standard stars, so a model atmospheric spectrum was calculated in order to remove telluric absorption features (Lord, 1992).

separate instrument position angles: 0°, 90°, 180°, and 270°.

Data reduction was performed via the NIFS pipeline available through IRAF. A Mask Definition File (MDF) was first attached to the raw calibration files in order to add variance (VAR) and data quality planes (DQ) in order to remove hot and dark pixels from the data files. After combining the flats and darks, the integral field unit data were cut into 29 extensions each of the science (SCI), VAR and DQ planes. Next, the final flat image is created. The flat was then corrected for any inter-slice variations. The arc and arc dark files are calibrated next. These files are used to calibrate the wavelength of the NIFS data. Like the flat files, an MDF was attached to the arc and arc dark files. Only one arc exposure was obtained for each observing date (per observing band). The arc dark files were then combined. The arc and arc dark files were then processed in order to cut the data into the 29 extensions for the SCI, VAR and DQ planes, while simultaneously flat fielding the arc and arc dark files. Due to the non-standard central wavelength used for the J-band observations, the variable crval had to be manually set to 1.28 μm during calibration file reduction.

Star	Other Identifiers	Spectral Type	Distance (pc)	Radius ($R_\odot$)	Mass ($M_\odot$)	T_{eff} (K)	Inclination (°)	Disk Position Angle (°)
HD 150193	MWC 836	B9.5Ve	151^{+1}_{-1}	1.9	1.9 ± 0.1	9000 ± 250	38 ± 9[1]	358 ± 6[1]
HD 163296	MWC 275	A1Vep	101^{+2}_{-1}	1.6	1.9 ± 0.1	9250 ± 250	46 ± 4[2]	132[7]
HD 179218	MWC 614	A0Ve	266^{+3}_{-3}	3.8	$3.0^{+0.2}_{-0.3}$	9500 ± 200	40 ± 10[3]	28 ± 3[8]
HD 250550	MWC 789	B9e	714^{+54}_{-47}	3.2	$2.6^{+0.3}_{-0.1}$	11000 ± 500	12 ± 3[4]	–
HD 259431	MWC 147	B6ep	725^{+26}_{-24}	5.2	$5.2^{+1.8}_{-1.3}$	14000^{+2100}_{-2900}	50[5]	80[5]
VV Ser		B7e	420^{+8}_{-8}	2.7	2.9 ± 0.1	13800 ± 200	65 ± 5[6]	17 ± 4[6]

Table 6.2: Stellar parameters for Herbig Ae/Be stars presented. All stellar parameters were obtained from Vioque et al. (2018) except radius. Stellar radii are computed based on Siess Pre-Main Sequence models (Siess et al., 2000). Disk parameters are found in the literature. Disk position angles are measured east of north. References: 1. Fukagawa et al. 2003; 2. Isella et al. 2007; 3. Dent et al. 2005; 4. Fedele et al. 2011; 5. Kraus et al. 2008a; 6. Pontoppidan et al. 2011; 7. Isella et al. 2016; 8. Kluska et al. 2018

The standard central wavelength for J-band observations is 1.25 μm. The J-band used an Argon arc lamp for wavelength calibration. Individual emission lines were then selected interactively. Finally, the Ronchi mask was reduced in order to correct for the spatial distortion along the slices. A MDF was attached and the files cut into 29 extensions in the same manner as the flat and arc files. Spatial calibration for the Ronchi mask was also performed.

J-band calibration data was obtained using the incorrect central wavelength for some dates, therefore, the calibration files from the 2012 06 08 observing run were used for 2012 data. After adding the MDF to the raw data, the sky emission was subtracted from the object files. Sky files were obtained by first observing the target then offsetting the telescope to an empty area in order to maintain similar seeing during each exposure. One sky file was used per two target files. The science data were then flat fielded and cut into the 29 SCI, VAR and DQ planes. Using the DQ plane, the bad pixels were removed. Next, the reduced arc and Ronchi mask files were used to derive the spectral and spatial transformation and applied to the raw data files. Finally, the raw data was reformatted into the final 3-D datacube.

6.2.1   Constructing X/Y Offsets

The analysis process consists of six steps. The first step consists of reading in the reduced data cube and extracting the pertinent variables to calculate the spectro-astrometric signal. Variables input via the command line include the radial velocity correction, obtained using `rvcorrect` in IRAF, the heliocentric velocity of each target star and the x/y center of the star from each data cube. The image viewing software QFitsView was used to calculate the center by using a 2-D Gaussian function to fit the center of light in the image. The rest central wavelengths for Paβ and Brγ were obtained using the NIST database (Kramida, 2010). The spectro-astrometric signal is computed by fitting the centroid of the line with a 2D Gaussian while the radial intensity profile is fitted with a 1D Moffat function. The wavelength is converted to velocity space using the heliocentric and radial velocity correction input in step one. SA is performed on the line and continuum in the velocity interval of -2000 km/s to 1500 km/s. In order to determine the 3σ level of the SA offsets, we select a region where the spectrum is outside of the emission feature and calculate the standard deviation of the continuum SA offset which should be zero.

An artifact was discovered during the analysis due to uneven slit illumination (Marconi et al., 2003). While looking at the offset in the direction perpendicular to the slits (dispersion

direction) in NIFS, telluric absorption lines were showing evidence of SA signals. There should be no offset when measuring the centroid of the telluric lines as they are due to Earth's atmosphere which should be symmetric about the instrument, thus having no SA offset. The false signature is calculated based on equations B10

$$\int_{-\infty}^{\infty} \tilde{\Psi}_j(w)dw = 2\Delta w \int_{x_0+\Delta x}^{x_0-\Delta x} dx \int_{y_j+\Delta y}^{y_j+\Delta y} dy \int \int_{-\infty}^{\infty} dx'dy' \mathscr{P} \tag{6.3}$$

and B11

$$\int_{-\infty}^{\infty} w\tilde{\Psi}_j(w)dw = 2\Delta w \int_{x_0+\Delta x}^{x_0-\Delta x} dx \int_{y_j+\Delta y}^{y_j+\Delta y} dy \int \int_{-\infty}^{\infty} dx'dy' w_0 \mathscr{P} \tag{6.4}$$

from Marconi et al. (2003), where $\tilde{\Psi}_j(w)$ is the expected line profile in the detector at pixel j, $\mathscr{P}$ is the product of the intensity and instrumental PSF, and w is the *observed* velocity, defined as

$$w = v + k(x - x_0). \tag{6.5}$$

The second term is the spurious velocity due to uneven slit illumination, where k is given by $\mu \Delta w / \Delta y$, and μ is defined as the anamorphic magnification which accounts for the different scales on the dispersion and slit directions. Artifacts have been reported in previous SA studies (Brannigan et al., 2006; Podio et al., 2008; Whelan et al., 2015). The primary sources of artifacts appear to arise from distortion of the point spread function (PSF) or unstable adaptive optics during image exposure. The best method to remove artifacts from the SA analysis is by combing parallel and anti-parallel slit configurations. Removal of SA artifacts via modeling has previously been attempted (Brannigan et al., 2006; Podio et al., 2008). Integral field units that incorporate the use of micro lenses or fibers would potentially remove any artifacts caused by uneven slit illumination, however, there is the potential for other instrumental artifacts that we do not account for at this time.

Next, a test datacube is created by taking the central spectra from the reduced datacube and applied to each spaxel, shifted by the calculated velocity shift, then scaled by the PSF estimated from the continuum. SA is performed on the test cube in order to determine the centroid offset solely from the velocity shift. Finally, the offset from the velocity shift is subtracted from the original datacube to arrive at the final offset measurement. Final SA offsets presented in section 6.3 are not absolute offsets for the emission line. Since the flux we are observing is composed of

Star	$\mathbf{L}_{\mathrm{Pa}\beta}$ $(10^{-3} \mathbf{L}_\odot)$	$\dot{\mathrm{M}}_{acc}$ $(10^{-7} \mathbf{M}_\odot \mathbf{yr}^{-1})$	$\mathbf{FWZI}_{\mathrm{Pa}\beta}$ $(\mathbf{km\ s}^{-1})$	$\mathbf{L}_{\mathrm{Br}\gamma}$ $(10^{-3} \mathbf{L}_\odot)$	$\mathbf{FWZI}_{\mathrm{Br}\gamma}$ $(\mathbf{km\ s}^{-1})$
HD 150193	6.29	1.58	545	0.30	472
	5.57	1.36	669	–	–
	5.54	1.35	669	–	–
HD 163296	3.09	0.54	595	–	–
	3.12	0.55	545	–	–
	3.90	0.73	595	–	–
HD 179218	14.21	5.59	619	0.71	472
	9.33	3.29	619	–	–
HD 250550	–	–	–	7.80	472
HD 259431	217.5	137.3	520	21.75	473
VV Ser	14.22	4.11	693	2.36	708

Table 6.3: H I emission results. Line luminosity is calculated using photometric values taken from the VizieR Photometry Viewer (Ochsenbein et al., 2000). A linear fit between the 2MASS:J and 2MASS:H filter was used to determine the flux density near 1.282 μm for the Paβ emission. Similarly, the 2MASS:Ks filter was used to determine the flux density for the Brγ emission. Full width at zero intensity is determined from where the emission profile reaches a value of 1 on either side of the emission line.

light from the continuum and emission feature, there exists continuum dilution (Pontoppidan et al., 2011) which will underestimate the spatial extent of the emitting region. The observations made in the 2015 observing run were taken at 4 position angles such that the artifacts could be removed without modeling. This method ensures that all artifacts from uneven slit illumination are removed from the SA signal.

6.3 Results

H I recombination emission is detected and spectrally resolved in all sources observed. In general, the Paβ emission features are stronger than the Brγ emission lines. Paβ also appears to be broader in the sources with observations of each line, with the exception of HD 259431, which presents the narrowest Paβ line. This is likely due to photospheric absorption not being accounted for in the ratio for the Brγ observations and stronger continuum emission due to dust in the K-band. Standard stars in the K-band are not observed and the telluric lines are removed via the use of an atmospheric model (Lord, 1992). All emission lines present as single-peaked features at the spectral resolution of NIFS.

6.3.1 HD 150193

Figure 6.1 shows the Paβ emission line observed in 2012 (top panel) and 2015 (middle panel), with corresponding SA offsets below the spectrum. The bottom panel shows 2015 SA offset measurements in a 2D plot. Paβ and Brγ are both observed in emission from the primary star, HD 150193A. The companion is observed in the NIFS observations in both bands. The Paβ emission line does show some variability across the three observations. The strongest emission occurs in the 2012 data with the two epochs from 2015 having similar strengths. The luminosity of the Paβ emission line is a factor of 0.88 weaker in the 2015 data. The line profiles are consistent across the three observations. The primary difference in the 2012 emission shows up as an excess of emission in the blue portion of the line. The line profile is symmetric about the line peak.

No significant detections are observed in the SA offset in the data acquired in 2015. We are careful to not include the companion in the SA analysis of HD 150193A. Limits can be placed on the SA offset coming from HD 150193A. We find that the emission is compact with a right ascension offset upper limit of 0.26 mas (0.04 au) and a declination offset upper limit of 0.26 mas (0.04 au). These limits are within those found from the 2012 observations. The 2012 observations place upper limits on the SA offset at 0.73 mas (0.10 au) and 0.39 mas (0.05 au) for the right ascension and declination, respectively.

Figure 6.2 shows Brγ emission observed in 2012 along with the corresponding SA offsets. 2D SA offsets are presented in the bottom panel. The Brγ emission feature shows some slight excess emission in the blue wings of the line profile. The structure appears similar to the Paβ emission line, however, the Brγ line is weaker than the Paβ emission. SA offsets are not detected for the Brγ emission. Upper limits are determined to be 0.69 mas (0.10 au) and 0.31 mas (0.05 au) for right ascension and declination, respectively. These upper limits are on order with the Paβ upper limits.

6.3.2 HD 163296

Figure 6.3 shows the 2012 and 2015 J-band observations, with corresponding SA offsets presented in the same manor as in Figure 6.1. The only observations for HD 163296 are for the Paβ emission line. Brγ data was saturated, thus that data is not included in analysis. Paβ emission observed in 2012 is symmetrical about the peak. 2015 data show a similar profile. The Paβ emission line observed in the second epoch of the 2015 data is stronger. The emission strength increases by a
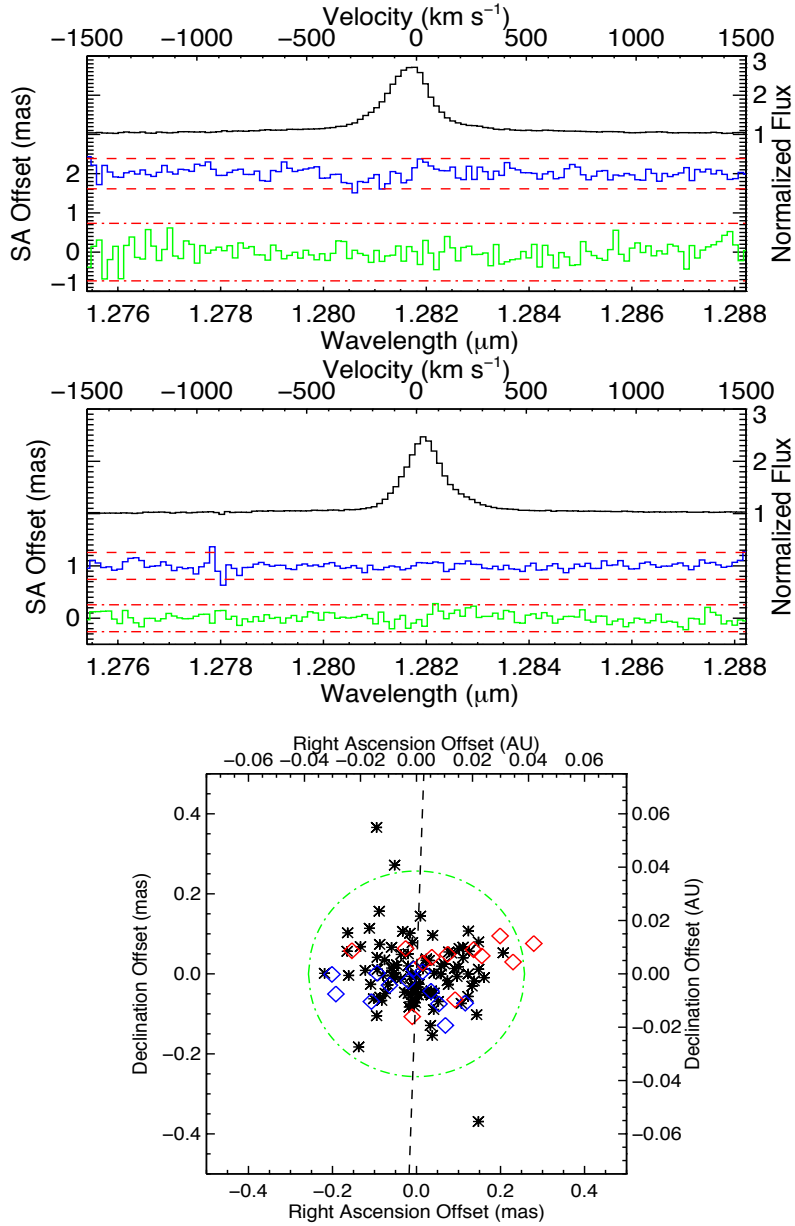
Figure 6.1: HD 150193 SA offset plots for the Paβ emission feature. The upper 2 graphs show the SA offset in right ascension (green) and declination (blue). The top panel is for the 2012 observations. The red dot-dashed line represents the 3σ limits calculated for the right ascension SA offset. The red dashed line represents the 3σ limits calculated for the declination. The declination is offset by 1 for clarity. The middle panel shows the SA offset for the 2015 observations. The 3 σ limits are denoted in the same manor as for the 2012 data. The lower panel is a 2D plot of the 2015 SA offset observations. The red diamonds represent offsets in the red-shifted portion of the Paβ emission line, while the blue represents the blue-shifted portion. Black asterisks represent the continuum. The green dashed ellipse represents the 3σ limits of the SA offset, and the black dashed line aligns with the disk position angle determined from previous work (with north being up and east being left in the plot).
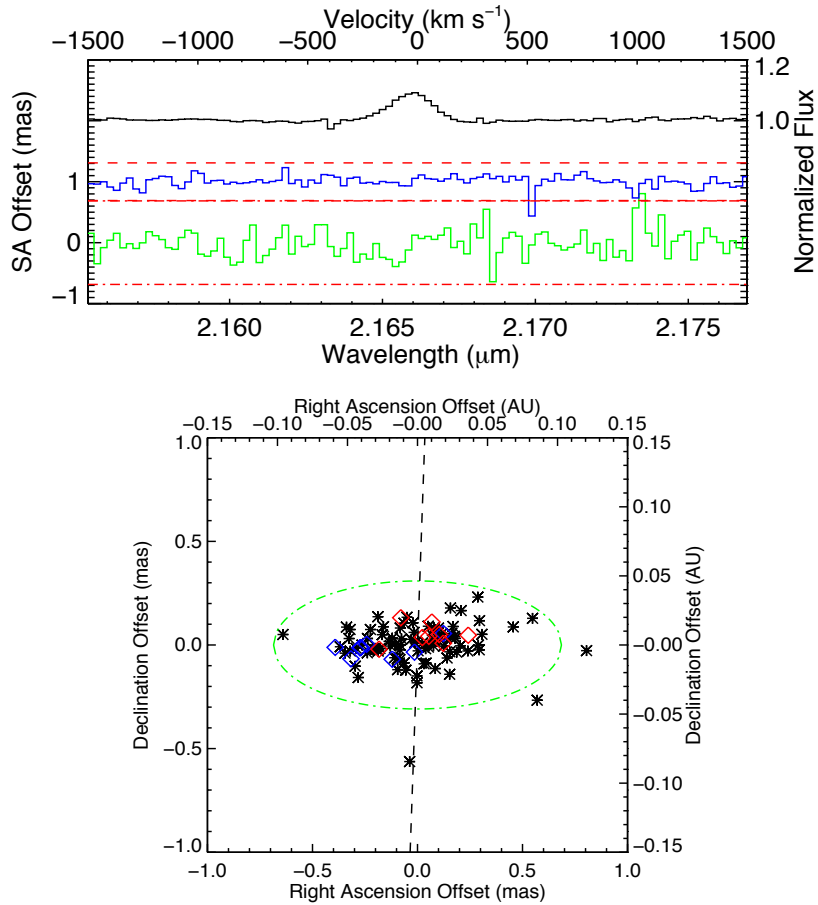
Figure 6.2: HD 150193 SA offset plots for the Brγ emission feature. The upper graph shows the SA offset in right ascension (green) and declination (blue) for observation made in 2012. The red dot-dashed line represents the 3σ limits calculated for the right ascension SA offset. The red dashed line represents the 3σ limits calculated for the declination. The declination is offset by 1 for clarity. The lower panel is a 2D plot of the SA offset observations. The red diamonds represent offsets in the red-shifted portion of the Brγ emission line, while the blue represents the blue-shifted portion. Black asterisks represent the continuum. The green dashed ellipse represents the 3σ limits of the SA offset, and the black dashed line aligns with the disk position angle determined from previous work (with north being up and east being left in the plot).

factor of 1.25 over the course of one day. The 2012 emission has the same strength as the emission from the first 2015 epoch.

We do not detect SA offsets in the 2012 data. The 3σ upper limit we place on the right ascension offset is 0.74 mas (0.08 au) and 0.52 mas (0.05 au) for the declination. 2015 observations do show a 2σ detection in the SA offset. We observe structure in the SA offset across the emission line, however, the strongest offset is observed near the peak of the emission. The strongest offsets are observed in the declination. No significant offset is seen in the right ascension. Looking at the 2D offset plot gives some insight as to where the offset could arise. We see that the emission appears to originate from an extended region that is perpendicular to the disk position angle. The 3σ detection threshold for right ascension is found to be 0.43 mas (0.04 au) and 0.26 mas (0.03 au) for declination. The 2015 limits are within the limits of the 2012 data which would explain why the 2σ offset is not observed in the first set of observations.

6.3.3   HD 179218

Paβ line profiles are consistent in shape between the 2012 and 2015 observations, as seen in Figure 6.4. They are symmetric about the line peak. The 2012 observation presents a stronger emission feature, decreasing in strength by a factor of 1.5 in the 2015 observation. HD 179218 has been shown to exhibit variability in Hα emission over the span of days (Kozlova, 2004). The cause of this variability in Hα is attributed to streams originating near the star's surface, possibly tied to accretion from the circumstellar disk.

SA offsets for HD 179218 are present at the 3σ level for the 2015 observations, but only just at the cutoff. The offsets lie perpendicular to the disk position angle. This likely indicates that the offset originates in an extended process, however, not directly coming from the circumstellar disk itself. It is still fairly compact as the 3σ levels are 0.30 mas (0.08 au) in right ascension and 0.24 mas (0.06 au) in declination. Only one velocity bin extends past the 3σ limits in the 2012 SA offsets. There is a slight offset observed in the 2012 SA measurement. As this source is only observed in one instrument position angle in 2012, we are not sure if all instrumental effects are being properly accounted for. Therefore, we are unsure if this offset is indeed real. The 3σ limits determined from the 2012 SA offsets are 0.96 mas (0.26 au) in right ascension and 0.33 mas (0.09 au) in declination. If a more extended source is the cause of the increased Paβ flux in 2012, then it is possible the SA offset would be present based on the limits we find. However, if the source of the emission across
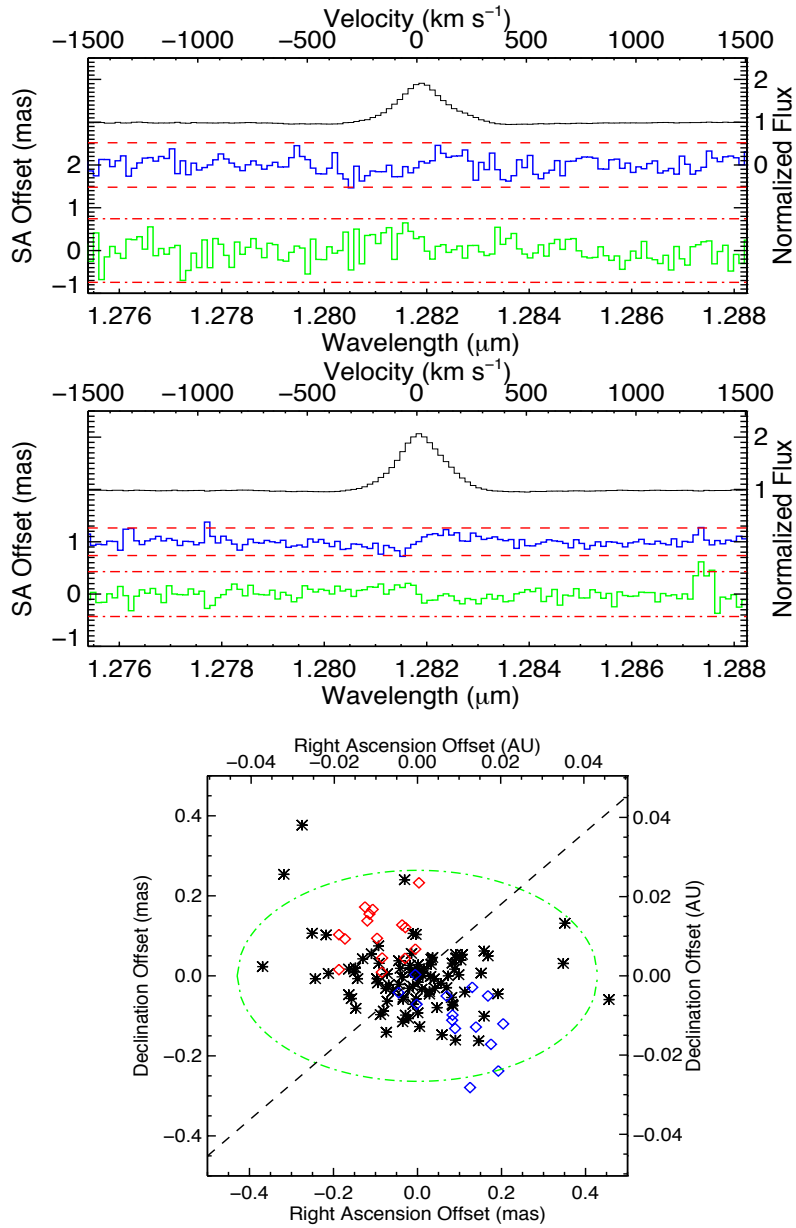
Figure 6.3: HD 163296 SA offset plots for the Paβ emission feature. The upper 2 graphs show the SA offset in right ascension (green) and declination (blue). The top panel is for the 2012 observations. The red dot-dashed line represents the 3σ limits calculated for the right ascension SA offset. The red dashed line represents the 3σ limits calculated for the declination. The declination is offset by 2 for clarity. The middle panel shows the SA offset for the 2015 observations. The 3 σ limits are denoted in the same manor as for the 2012 data. The lower panel is a 2D plot of the 2015 SA offset observations. The red diamonds represent offsets in the red-shifted portion of the Paβ emission line, while the blue represents the blue-shifted portion. Black asterisks represent the continuum. The green dashed ellipse represents the 3σ limits of the SA offset, and the black dashed line aligns with the disk position angle determined from previous work (with north being up and east being left in the plot).

both epochs is the same, then the offset observed in 2015 should be greater as the extent of the detection lies within the 2012 SA 3σ limits.

Figure 6.5 presents 2012 Brγ emission and SA offset measurements. Brγ emission observed in HD 179218 shows a similar profile as the Paβ emission. The line is symmetric about the peak. The SA offsets for the Brγ emission line do not present a detection. We place a 3σ upper limit of 0.38 mas (0.10 au) on the right ascension and 0.31 mas (0.08 au) on the declination. The possible causes for the lack of a detection in the Brγ SA offset when there is a detection in there Paβ line is discussed in Section 6.5.1.

6.3.4   HD 250550

Only Brγ data is presented for HD 250550, shown in Figure 6.6. We did not observe the J-band for this source. The emission profile is symmetric about the peak. We do not observe an offset in the SA signal. The 3σ upper limits are 0.44 mas (0.31 au) for right ascension and 0.21 mas (0.15 au) for declination.

6.3.5   HD 259431

HD 259431 is the source with the earliest spectral type (B6). The Paβ emission we observe in this source is the strongest in the survey, corresponding to a $L_{\mathrm{Pa}\beta} = 217.5\ L_\odot$. While it is the strongest, it also presents as the narrowest. This indicates that there is less emission coming from high velocity hydrogen gas (i.e, material accreting onto the stellar surface near free-fall velocities). Figure 6.7 shows the PAβ emission feature and SA offsets.

The SA offset is also the most extended in HD 259431. We determine 3σ levels to be 1.16 mas (0.84 au) in right ascension and 0.78 mas (0.57 au) in declination. The maximum offset we measure extends beyond 7 mas (5.075 au) in right ascension. The extension is not as great in the opposite direction, but still extends out to about 4 mas (2.9 au). This extension traces the disk position angle, thus the extension is likely due to some process that is occurring in the circumstellar disk. As this data only looks at one instrument position angle, further observations are required to determine if the SA signal detected is not due to systematic effects.

The Brγ emission line observed in HD 259431 presents a similar profile as the Paβ emission feature, as seen in Figure 6.8. It is also the strongest Brγ emission feature we observe, as in the case
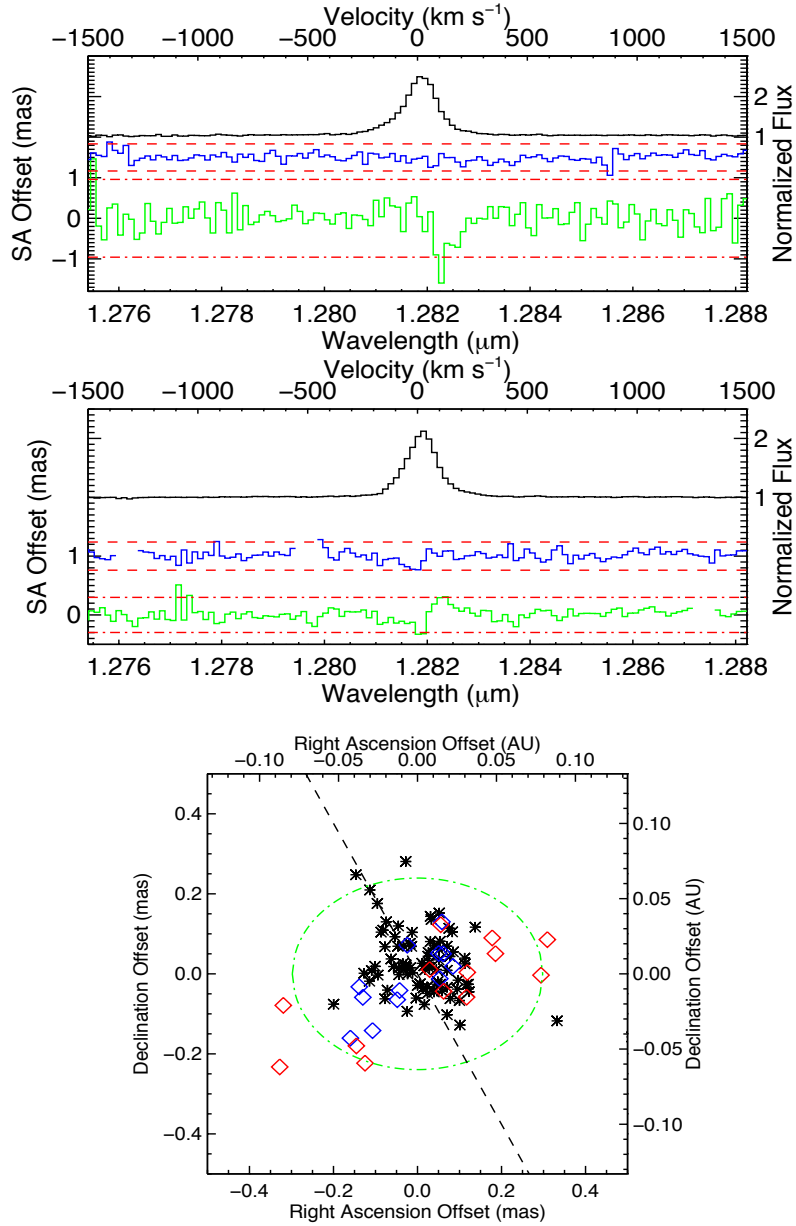
Figure 6.4: HD 179218 SA offset plots for the Paβ emission feature. The upper 2 graphs show the SA offset in right ascension (green) and declination (blue). The top panel is for the 2012 observations. The red dot-dashed line represents the 3σ limits calculated for the right ascension SA offset. The red dashed line represents the 3σ limits calculated for the declination. The declination is offset by 1 for clarity. The middle panel shows the SA offset for the 2015 observations. The 3σ limits are denoted in the same manor as for the 2012 data. The lower panel is a 2D plot of the 2015 SA offset observations. The red diamonds represent offsets in the red-shifted portion of the Paβ emission line, while the blue represents the blue-shifted portion. Black asterisks represent the continuum. The green dashed ellipse represents the 3σ limits of the SA offset, and the black dashed line aligns with the disk position angle determined from previous work (with north being up and east being left in the plot).
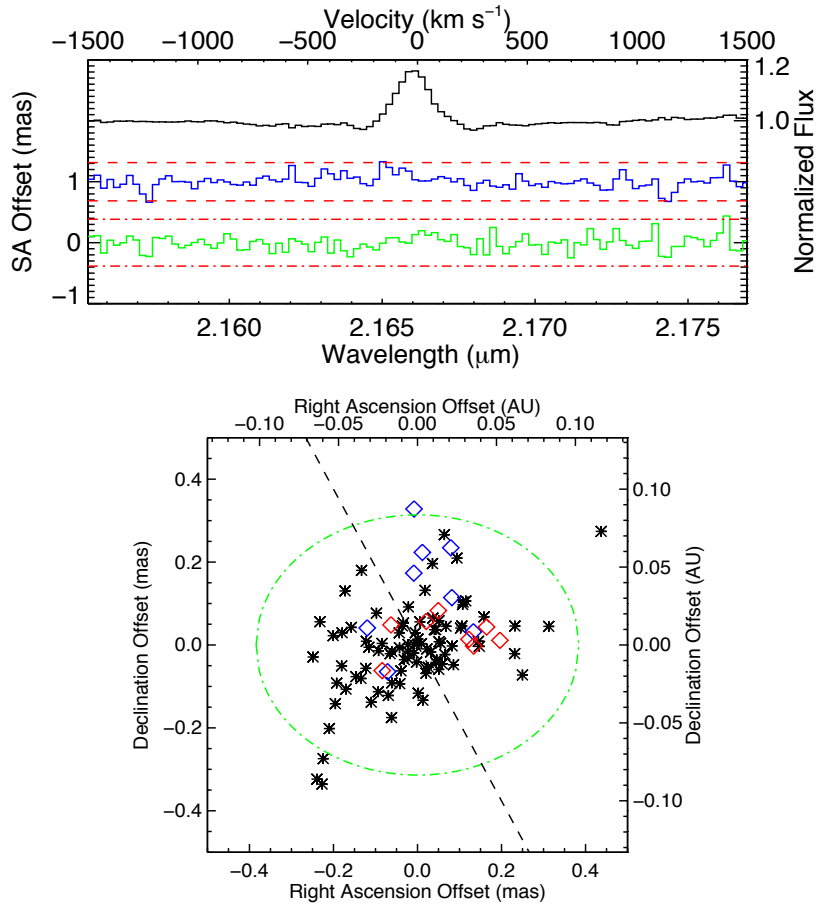
Figure 6.5: HD 179218 SA offset plots for the Brγ emission feature. The upper graph shows the SA offset in right ascension (green) and declination (blue) for observation made in 2012. The red dot-dashed line represents the 3σ limits calculated for the right ascension SA offset. The red dashed line represents the 3σ limits calculated for the declination. The declination is offset by 1 for clarity. The lower panel is a 2D plot of the SA offset observations. The red diamonds represent offsets in the red-shifted portion of the Brγ emission line, while the blue represents the blue-shifted portion. Black asterisks represent the continuum. The green dashed ellipse represents the 3σ limits of the SA offset, and the black dashed line aligns with the disk position angle determined from previous work (with north being up and east being left in the plot).
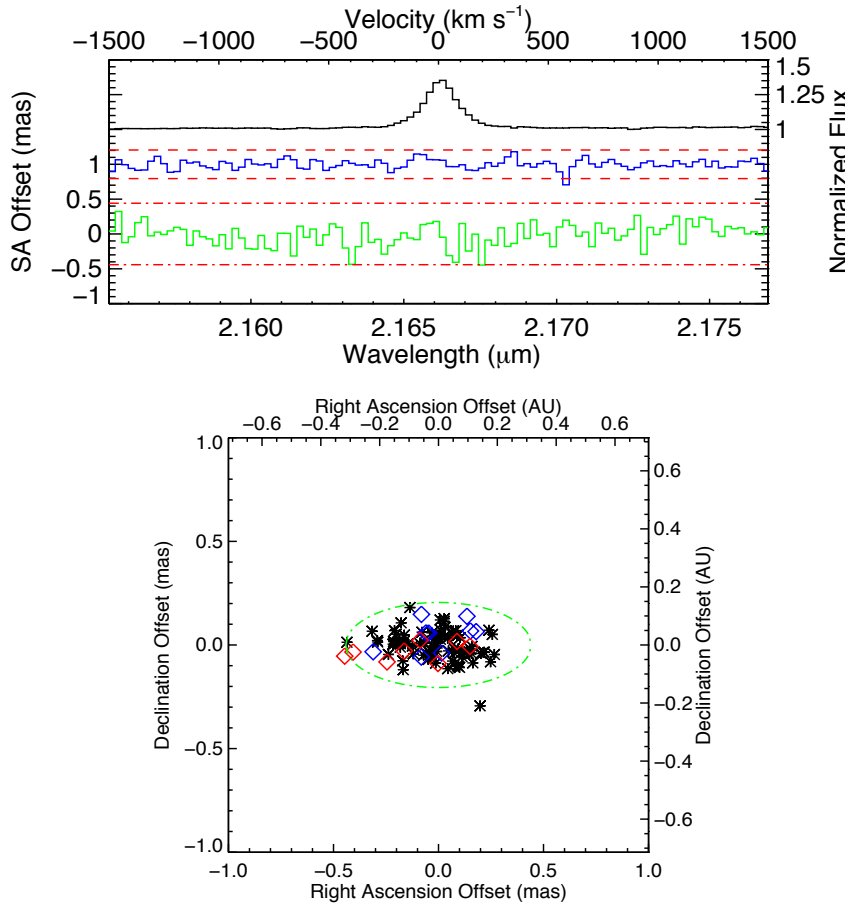
Figure 6.6: HD 250550 SA offset plots for the Brγ emission feature. The upper graph shows the SA offset in right ascension (green) and declination (blue) for observation made in 2012. The red dot-dashed line represents the 3σ limits calculated for the right ascension SA offset. The red dashed line represents the 3σ limits calculated for the declination. The declination is offset by 1 for clarity. The lower panel is a 2D plot of the SA offset observations. The red diamonds represent offsets in the red-shifted portion of the Brγ emission line, while the blue represents the blue-shifted portion. Black asterisks represent the continuum. The green dashed ellipse represents the 3σ limits of the SA offset, and the black dashed line aligns with the disk position angle determined from previous work (with north being up and east being left in the plot).

Figure 6.7: HD 259431 SA offset plots for the Paβ emission feature. The upper graph shows the SA offset in right ascension (green) and declination (blue) for observation made in 2012. The red dot-dashed line represents the 3σ limits calculated for the right ascension SA offset. The red dashed line represents the 3σ limits calculated for the declination. The declination is offset by 1 for clarity. The lower panel is a 2D plot of the SA offset observations. The red diamonds represent offsets in the red-shifted portion of the Brγ emission line, while the blue represents the blue-shifted portion. Black asterisks represent the continuum. The green dashed ellipse represents the 3σ limits of the SA offset, and the black dashed line aligns with the disk position angle determined from previous work (with north being up and east being left in the plot).
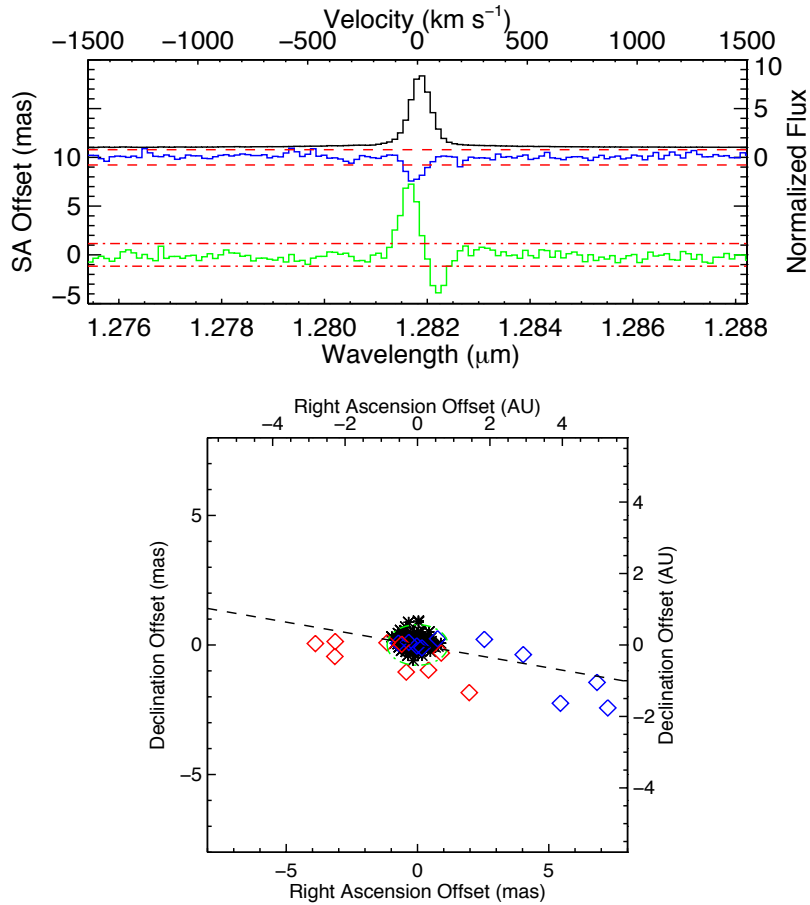
of the Paβ emission. The emission is symmetric about the peak of the line profile. HD 259431 is the only source in the survey that shows a significant SA offset in the Brγ emission line. The 3σ levels we determine are 0.47 mas (0.34 au) in right ascension and 0.27 mas (0.20 au) in declination. The offset we detect is extended in the same direction as the offset observed in Paβ. The only difference is that the extension occurs in the red portion of the emission line, whereas the largest Paβ offset is observed in the blue portion of the emission line.

6.3.5.1 CO Bandhead Emission

We also observe CO bandhead emission from $\nu = 2 \to 0$ and $3 \to 1$ bandheads (Figure 6.9, first reported by Ilee et al. (2014). Using the same region that Ilee et al. (2014) use to measure the CO equivalent width (2.29 - 2.30 μm), we determine a CO equivalent width of $5.28 \pm 0.26 \times 10^{-4}$ μm. This is slightly higher than the value determined from Ilee et al. (2014) of $4.4 \pm 0.1 \times 10^{-4}$ μm. Due to the lower resolution in the NIFS data, we are not able to resolve any isolated emission features. We do not perform SA analysis on the CO bandhead.

6.3.6 VV Ser

VV Ser presents the most distinctive hydrogen emission lines. The Paβ emission feature, shown in Figure 6.10, appears to be comprised of two components: a broad component and a narrow component. The broad component dominates the blue wings of the line profile, indicating gas moving towards the observer at high velocities. The narrow component peaks near the zero velocity bin.

A SA offset is detected in the Paβ emission feature with offsets present in both the right ascension and declination. The 3σ levels are found to be 0.69 mas (0.29 au) in right ascension and 0.26 mas (0.11 au) in declination. The largest offset is perpendicular to the disk position angle found in the literature, and extends out to about 1 mas (0.42 au).

Brγ shows a similar emission line profile as the Paβ with a broad component, dominating the blue portion of the line, and a narrow component centered at the zero velocity bin. The Brγ emission feature and SA offset measurements are presented in Figure 6.11. It is the broadest Brγ emission feature with a Full Width at Zero Intensity (FWZI) comparable to the Paβ emission line. The Brγ SA offset does not show a detection above the 3σ limit. Right ascension SA offsets are found to be 0.26 mas (0.11 au) and declination limits are found to be 0.19 mas (0.08 au). These limits are below those found for Paβ.
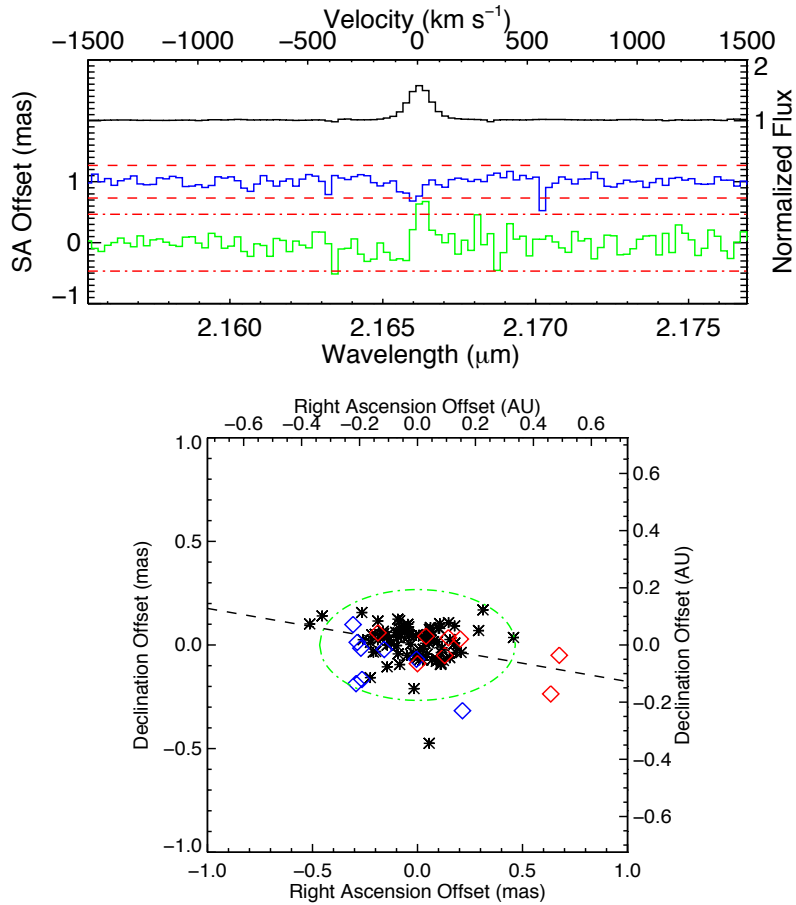
Figure 6.8: HD 259431 SA offset plots for the Brγ emission feature. The upper graph shows the SA offset in right ascension (green) and declination (blue) for observation made in 2012. The red dot-dashed line represents the 3σ limits calculated for the right ascension SA offset. The red dashed line represents the 3σ limits calculated for the declination. The declination is offset by 1 for clarity. The lower panel is a 2D plot of the SA offset observations. The red diamonds represent offsets in the red-shifted portion of the Brγ emission line, while the blue represents the blue-shifted portion. Black asterisks represent the continuum. The green dashed ellipse represents the 3σ limits of the SA offset, and the black dashed line aligns with the disk position angle determined from previous work (with north being up and east being left in the plot).
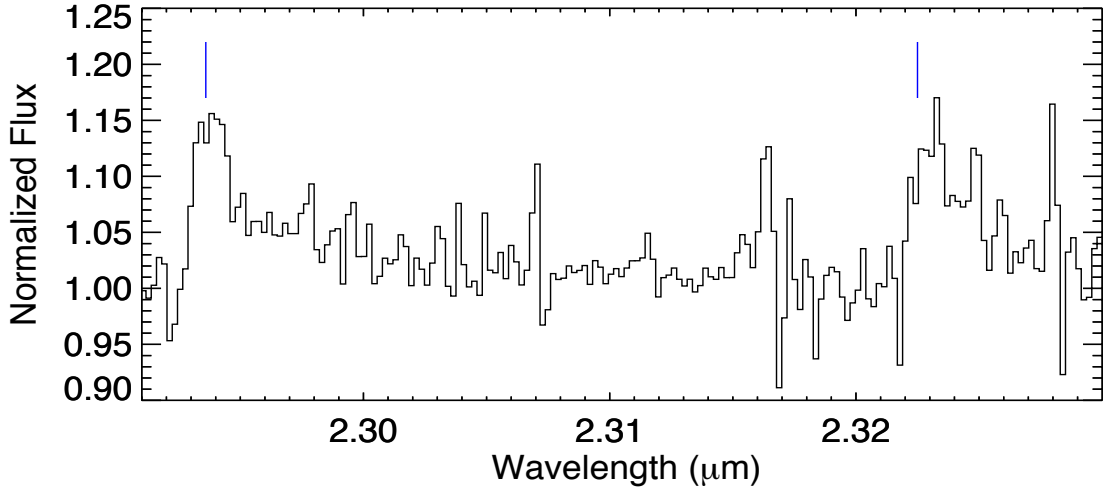
Figure 6.9:   HD 259431 CO bandhead emission.   The blue hash marks indicate the bandhead locations, with the CO $\nu = 2 \rightarrow 0$ bandhead lying to the left in the plot and $\nu = 3 \rightarrow 1$ bandhead on the right.

6.4   Modeling

We have computed a model for a purely Keplerian circumstellar disk and fit the model to the emission line and SA signal. Early (A and B) type stars are not expected to have strong magnetic fields, and, thus, would not likely accrete magnetospheically (Alecian et al., 2013). One possible source for H I emission that is not in an extended outflow would be hot material in the inner disk region. It is possible that the UV field of early type stars creates a mini-H I region on the surface of the circumstellar disk. This gas would be in Keplerian orbit and could, in principle, give rise to the Paβ and Brγ emission observed. We fit a simple power-law model to the data where

$$I(R) = I_0 \left(\frac{R}{R_0} \right)^{-\alpha},$$ (6.6)

where I is the intensity in normalized units and it varies with radius, R, to the power -α. R_0 is set to to be 1 au and I_0 is the intensity at R_0, defined as 1 for simplicity.

We compute models for HD 163296 as it is the closest source in the sample, thus, the offsets due to a circumstellar disk would be the strongest. We first fit Brγ emission observed with NIRSPEC (Brittain et al., 2007) due to its high resolution. This allows for a better constraint on the inner
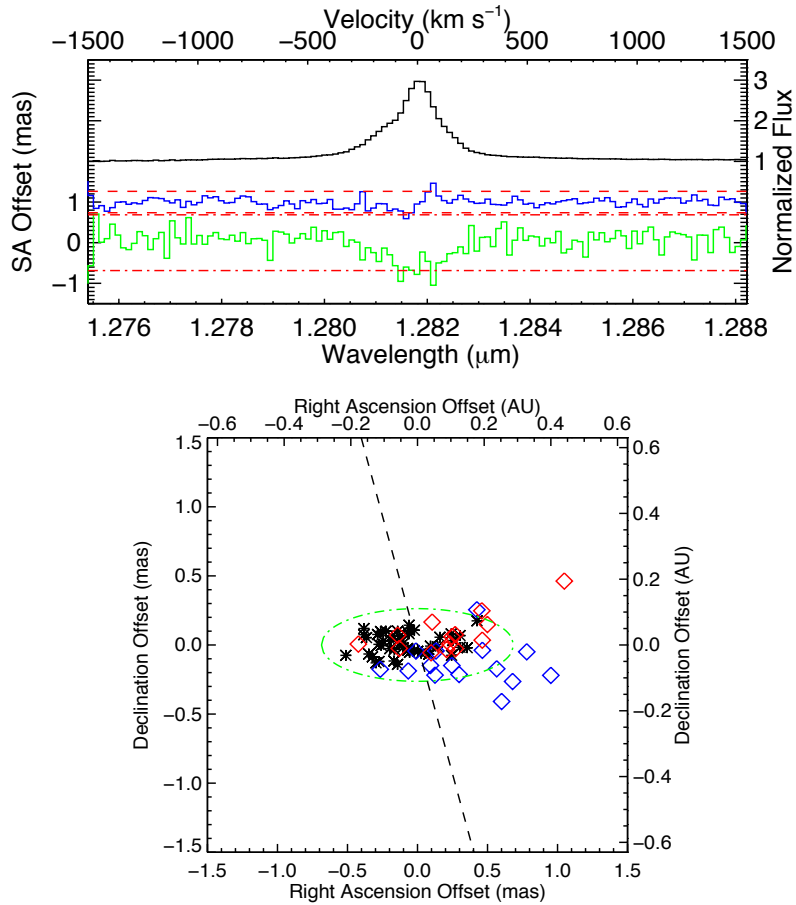
110

Figure 6.10: VV Ser SA offset plots for the Paβ emission feature. The upper graph shows the SA offset in right ascension (green) and declination (blue) for observation made in 2012. The red dot-dashed line represents the 3σ limits calculated for the right ascension SA offset. The red dashed line represents the 3σ limits calculated for the declination. The declination is offset by 1 for clarity. The lower panel is a 2D plot of the SA offset observations. The red diamonds represent offsets in the red-shifted portion of the Brγ emission line, while the blue represents the blue-shifted portion. Black asterisks represent the continuum. The green dashed ellipse represents the 3σ limits of the SA offset, and the black dashed line aligns with the disk position angle determined from previous work (with north being up and east being left in the plot).

Figure 6.11: VV Ser SA offset plots for the Brγ emission feature. The upper graph shows the
SA offset in right ascension (green) and declination (blue) for observation made in 2012. The red
dot-dashed line represents the 3σ limits calculated for the right ascension SA offset. The red dashed
line represents the 3σ limits calculated for the declination. The declination is offset by 1 for clarity.
The lower panel is a 2D plot of the SA offset observations. The red diamonds represent offsets in
the red-shifted portion of the Brγ emission line, while the blue represents the blue-shifted portion.
Black asterisks represent the continuum. The green dashed ellipse represents the 3σ limits of the
SA offset, and the black dashed line aligns with the disk position angle determined from previous
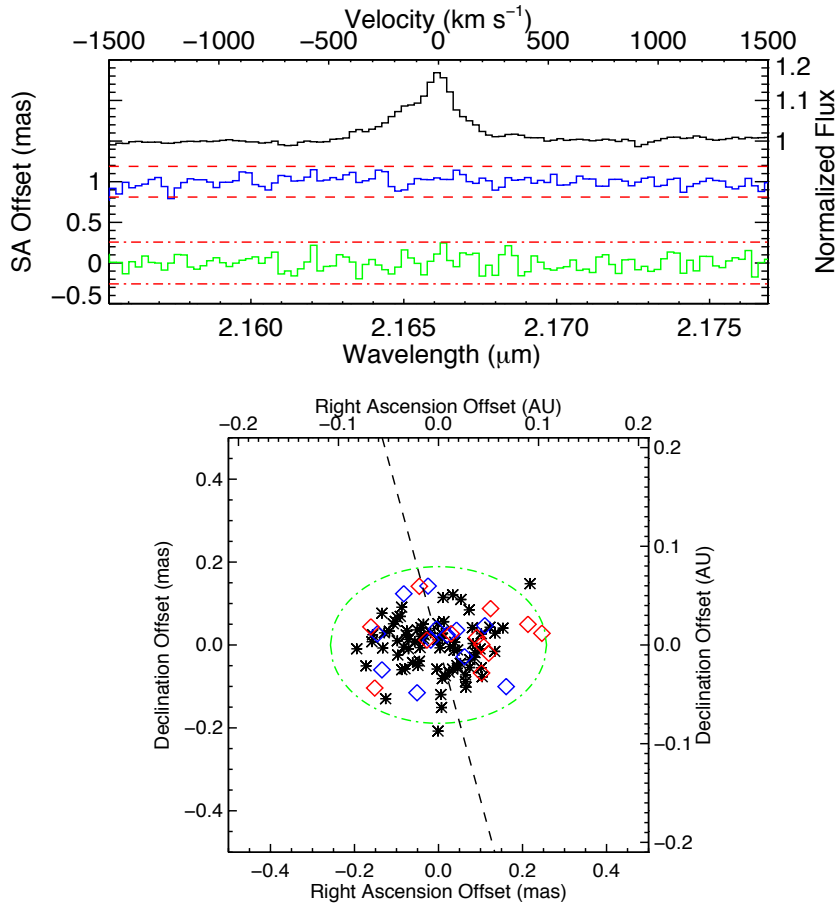work (with north being up and east being left in the plot).

and outer radius of the emitting region. In order to fit the high velocity wings of the emission, we employed the use of a double power-law. The intensity distribution follows the same functionality as in Equation 6.6, however, at the break radius, R_{break}, the power-law exponent shifts. Our model has four free-parameters; R_{out}, R_{break}, α_1, and α_2 (Equation 6.7).

$$I(R) = \begin{cases} I_0 \left(\frac{R}{R_0}\right)^{-\alpha_1} for R_{\text{in}} \leq R < R_{\text{break}} \\ I_0 \left(\frac{R}{R_0}\right)^{-\alpha_2} for R_{\text{break}} \leq R < R_{\text{out}} \end{cases} \tag{6.7}$$

R_{in} is determined from the FWZI of the emission line. We compute a reduced χ^2,

$$\chi^2_{\text{spec}} = \frac{\Sigma(\text{F}_{\text{line}} - \text{F}_{\text{model}})^2}{\sigma^2_{\text{continuum}}}, \tag{6.8}$$

to determine the final best fit parameters.

Our best fit model indicates that a circumstellar disk would need to extend down to $R_{\text{in}} = 0.01$ au (very close to the stellar surface of $\sim$0.0098 au) and have a power-law exponent of $\alpha = 1.84$, with break radius of $R_{\text{break}} = 0.06$. From here, the power-law now has an exponent of $\alpha = 2.70$ and extends to $R_{\text{out}} = 5.05$ au. The high-resolution model results are shown in Figure 6.12. The model emission line shows a double-peaked profile that could be present in the data, however, it is not discernible from the noise. Increasing the outer radius would act to fill in this double peak.

After the high resolution data is modeled, the best fit parameters are then used to determine a profile from the same geometrical set-up for Paβ emission as observed from NIFS. The top panel of Figure 6.13 shows the end result. The model is not a perfect match. This is likely caused by convolving the model with different instrument profiles in fitting the NIRESPEC and NIFS data. The major difference in the Paβ profile is that the data is dominated by the lower velocity portion of the emission feature, which would correspond to emission coming from further out in the circumstellar disk.

While computing the expected emission line profile, we also compute the expected SA offset from the circumstellar disk described from the best fit parameters. This is done by creating a model disk with the same intensity profile and then determining the center of light of each velocity bin. The expected SA offset from the circumstellar disk is plotted over the corresponding SA measurement in the top panel of Figure 6.13. The SA offset would clearly be detected in our measurements if the
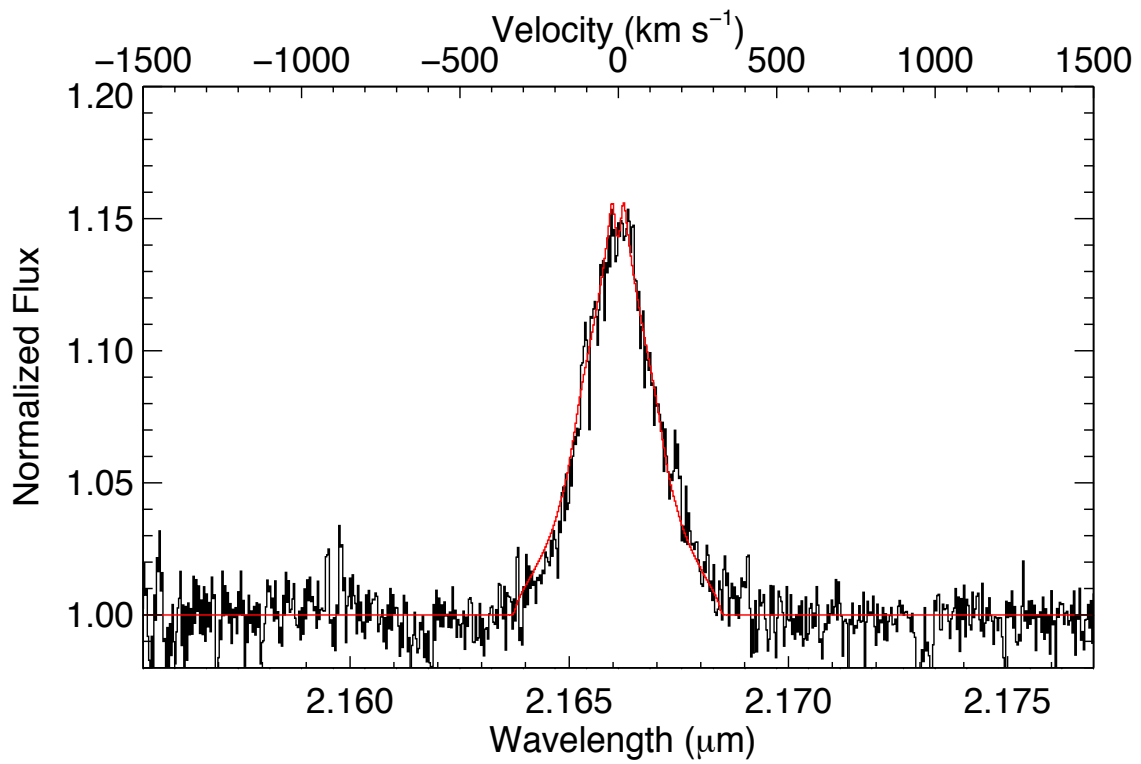
Figure 6.12: HD 163296 Brγ line profile from NIRSPEC observations. Upper x-axis shows the corresponding velocity space. Best fit model is plotted in red.
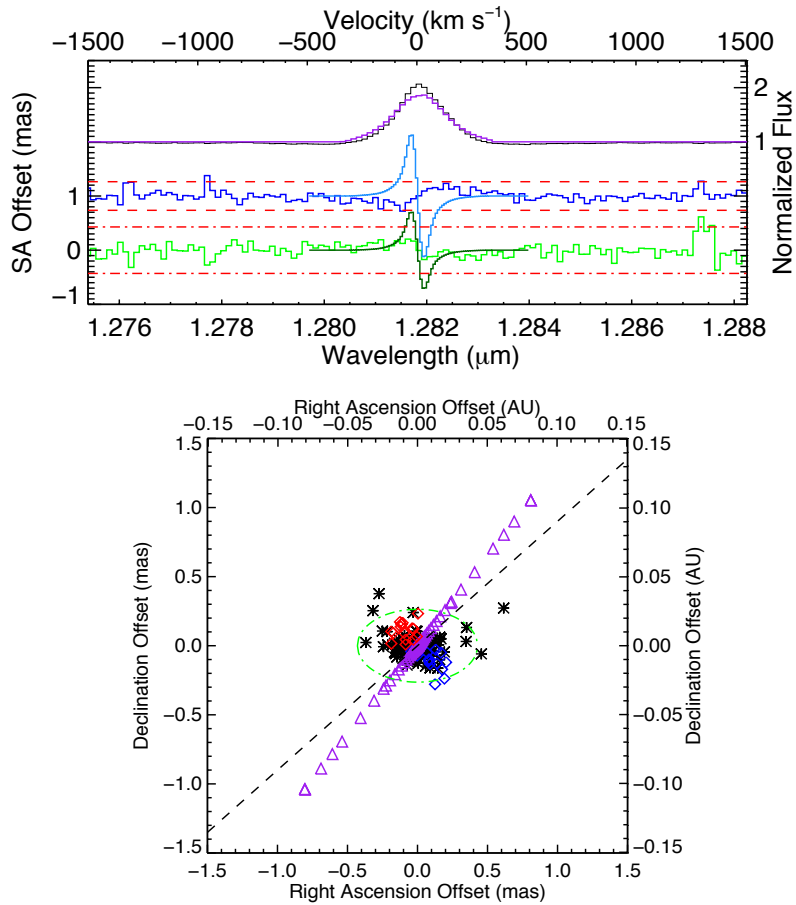
Figure 6.13: HD 163296 Paβ line profile from NIFS observations. The upper x-axis shows the corresponding velocity space. The best fit model is plotted in purple and is based on the best fit profile from the Brγ modeling. The discrepancy between this figure and the preceding figure arises due to the different instrument profiles for NIFS and NIRSPEC. This model was convolved with an instrument profile using the resolution of NIFS. The model SA offsets are plotted over their corresponding SA offset measurement (right ascension is plotted in dark green and declination is plotted in light blue). The bottom panel shows the 2D plot of the model SA offsets, as purple triangles, with the 2015 SA offset measurements plotted in the same manor as in the bottom panel of Figure 6.3.

emission was predominately produced in a circumstellar disk extending from near the stellar surface out to 5 au. The bottom panel of Figure 6.13 presents a 2D representation of the expected SA offset for the best-fit circumstellar disk model. The SA offset would be expected to extend out to ∼1 mas (∼0.1 au), which is larger than the observed SA offset in HD 163296. The SA offset follows the disk position angle, as expected from the circumstellar disk model.

6.5 Discussion

H I recombination emission lines are detected from all sources in this survey. 3 of the 5 sources observed in the J-band show significant SA offset detections, while only one source (HD 259431) shows evidence of extended emission in the K-band. Due to the larger line-to-continuum ratio observed in the Paβ line, it could prove to be a better candidate of tracing mass-loss processes in HAeBe systems. Of the sources from which SA offsets are detected, the two that show the most extended emission are the earliest type stars in the survey: HD 259431 and VV Ser. The fact that these stars are more massive and hotter should mean that the regions close to the star are more energetic. This could be more conducive to driving outflows from the inner regions of these systems, leading to more extended origins for the H I emission.

Previous interferometric observations exist for some of the sources in this survey. Brγ, Paβ, and Paδ were observed in the VV Ser system with AMBER on the Very Large Telescope Interferometer (VLTI) by Garcia Lopez et al. (2016). They find that the average H I line profile across the three lines observed is best fit with some outflow model, with only a small contribution from a magnetosphere. This is in line with our SA offset measurements.

Similarly, HD 163296 was also observed with AMBER on the VLTI by Garcia Lopez et al. (2015). They report that an outflow is the likely source of the interferometric observables in their study. The wind they model is compact (launching radius of 0.02 au out to 0.04 au). Our SA offsets indicate that the origin of Paβ emission would likely come from a compact region as well. The model of the disk wind from Garcia Lopez et al. (2015) indicate that the outflow would be perpendicular to the disk position angle. While our observations do not provide a strong 3σ detection in HD 163296, there is some structure in the SA offsets that indicate the emission could originate in a source perpendicular to the disk position angle, however, further observations are required to confirm this measurement. HD 163296 is the source of a microjet which produces knots of nebulosity called

Herbig-Haro objects (HH 409; Grady et al. 2000). This outflow has been observed to emanate roughly perpendicular to the circumstellar disk.

HD 179218 was observed with the CHARA array on the VEGA spectrometer (Mendigutía et al., 2017). The study looked at Hα emission and concluded that the emission is coming from a compact region (< 0.21 au). Our observations of Paβ are able to detect a SA offset within the limits determined by Mendigutía et al. (2017). They report that the bulk of the Hα emission can be reproduced with a MA model. However, the offset detected in Paβ emission would likely not be caused by MA. The expected magnetospheres of HAeBe stars are on the order of a few stellar radii. This would not produce a SA offset, even with the limits we are able to achieve in this study.

More recently, HD 259431 Brγ emissoin has been observed with AMBER/VLTI (Hone et al., 2019). They report that Brγ emission arises from a compact region, likely tracing hot gas inside the dust sublimation radius (< 1.52 au) and is best fit by a geometric model with an inclination of ∼19° and a position angle of ∼18°. This is contrary to our SA measurements of extended emission arising from a position angle closer to ∼80°. The geometry of the HD 259431 system is not well constrained, so more in-depth studies are necessary to unravel this issue. For now, spectro-interferometric observations are the best for observing the compact origins of H I emission.

It is possible that the SA offsets measured from the 2012 observations are not properly removing artifacts from the analysis. Observations with another integral field spectrograph, SINFONI, also on the VLT on HD 100546 indicate a SA offset perpendicular to the disk position angle (C. Dougados, private communication). Mendigutía et al. (2015a) instead report spectro-interferometric observations consistent with emission aligning with the disk position angle. It is possible that the systematic artifacts of SA offsets observed with integral field units are not fully understood. Further investigation is necessary to ensure all potential systematic effects are taken into account.

Accretion rates are calculated using the relationship presented in Fairlamb et al. (2017) for Paβ, presented in Table 6.3,

$$log(\frac{L_{\text{acc}}}{L_\odot}) = 3.47 + 1.26 \times log(\frac{L_{Pa\beta}}{L_\odot}).$$

(6.9)

These accretion rates are in line with previous values reported in the literature (i.e., Hillenbrand et al. 1992; Donehew & Brittain 2011; Fairlamb et al. 2015). Mendigutía et al. (2015b) explore the connection of various emission lines observed in pre-main seequence stars with the accretion

luminosity as determined from the Balmer excess. They report that the likely cause of the L_{acc} vs. L_{line} correlation is the connection to the stellar luminosity, i.e., brighter stars will have brighter emission lines no matter the physical processes that produce the emission line. When removing the stellar luminosity dependence from individual lines, Hα still correlated with L_{acc}, indicating that the emission is likely connected to accretion related processes.

6.5.1 Weakening of the Brγ Signal

Earlier type stars with SA offsets tend to show stronger Paβ offsets than the corresponding Brγ observations. There are two possible explanations for this discrepancy. The first is that the emission lines are created via different physical processes. The second is that the K-band could be more strongly effected by the continuum. Dust in the circumstellar disk emits more in the K-band than in the J-band. Due to this, the line-to-continuum ratio for Brγ emission would be lower, thus the continuum contribution to the SA offset would be higher.

6.6 Conclusion

We present Paβ and Brγ emission observations taken with Gemini/NIFS. SA is performed in order to determine the origins of H I emission from HAeBe stars. Data from two observing runs, one in 2012 and another in 2015, show some SA offset detections, however, the SA offsets mostly show that the emission arises from fairly compact regions within the system. Our study does provide high fidelity SA measurements on the H I emitting regions of HAeBe systems, however, we are unsure if all systematic uncertatinies are being appropriately accounted for in the integral field unit observations. Once these systematic effects are accounted for, SA combined with integral field units would be a potential avenue to study H I origins as our SA offset fidelity is consistent with the theoretical limit of SA uncertainties. Increased integration times should improve the signal-to-noise ratio of the observations, which should allow for improved SA fidelity. As for the time being, spectro-interferometric observations are recommended for the study of the accretion-ejection mechanisms of HAeBe stars. Spectro-interferometry is effected by fewer artifacts in the observables and requires shorter observation times.

Chapter 7

Conclusions

The research presented in this dissertation provides insights on the inner-most regions of circumstellar disks around Herbig Ae/Be stars. Molecular emission provides details on the dynamics in the terrestrial planet-forming region of the disk (< 10 au) and the gas temperatures of species present in these areas. Hydrogen recombination emission lines can illuminate the mass-loss processes ongoing in these systems.

7.1 Molecular Emission

7.1.1 HD 101412

The results from the HD 101412 study present the first detection of water vapor emission in the near-infrared from the disk of a Herbig Ae/Be star, along with a new detection of OH emission. The report combines the new detections with archival CO data in order to determine if the molecular emission is located in the same region of the disk and if they have comparable temperatures. Modeling of the emission line profiles indicate that all three molecules originate from a narrow annulus near the inner edge of the circustellar disk (0.8 - 1.4 au). The temperature of the molecular gas is also consistent across each species at about 1300 K, however, better contraints on the OH temperature could be obtained by looking at higher energy transitions in the future. Ultimately, it is concluded that the reason for the detection of water vapor emission in this system is due to the fortuitous geometry in which it is viewed.

HD 101412 is nearly edge-on, inclined at an angle of 86°. This coupled with the fact that the disk has a high gas-to-dust ratio would mean that we are likely observing the inner wall of the circustellar disk and looking through a higher column density of gas. This would strengthen the emission features observed. Based purely on the line-to-continuum ratio, HD 101412 presents the strongest OH P4.5 emission detected around a Herbig Ae/Be star. Typically, OH presents at about 2-3% above the continuum, whereas HD 101412's OH emission is at 9%. The gas-to-dust ratio is determined to be $\sim$600, whereas typically, it is assumed that this value is around 100.

One scenario that could allow for this clearing of dust in the inner disk is the presence of a massive planet forming interior to the snowline (< 25 au). This would create a pressure bump that would trap dust particles behind the planet, but allow the gas to move interior to the orbit. Lying interior to the snowline would mean that the water ice would sublimate before reaching the pressure bump, and the water vapor could then pass into the inner disk.

7.1.2 V380 Ori

OH P5.5 (2$-$, 2$+$) emission from the disk of V380 Ori is studied in an attempt to characterize the inner disk of the circumbinary disk. The new observations presented here do not show the asymmetries previously reported in OH emission from the system. This could be a result of lower signal-to-noise observations masking the asymmetry. CO observations also do not show the same asymmetry. The line profiles of OH and CO are consistent with originating from the same region of the system, therefore the asymmetry should be present assuming it is produced as a result of the geometry of the disk. This could indicate that the source of the asymmetry varies on a few year timescale as the OH P4.5 and CO observations are taken $\sim$3 years apart. This would rule out the asymmetry arising due to tidal interaction between the binary stars and disk creating an eccentric inner disk. Archival observations of the OH P4.5 (1$+$, 1$-$) emission feature are re-reduced in the same manner as the OH P5.5 emission for consistency. The asymmetry is not reproduced in the re-reduced data.

7.1.3 CRIRES Survey

Our survey of OH P4.5 (1$+$, 1$-$) and water vapor emission from Herbig Ae/Be disks has provided further insights to the connection of these molecules and various stellar and disk parameters.

The study finds additional detections of OH emission around 5 of 13 sources, increasing the sample of known OH emission from Herbig Ae/Be disks to 15 of 31 (48.4%) sources observed. We have also found evidence for two more sources with water vapor emission in the near-infrared: HD 104237 and HD 163296. This shows that water vapor can survive, to an extent, in the inner terrestrial planet-forming regions of Herbig Ae/Be disks. Looking at the relative strengths of OH and H_2O emission compared to various stellar and disk parameters support previous reports that the far ultraviolet radiation fields of early type Herbig Ae/Be is the main culprit in the lack of detections of water vapor emission from these sources. The water that is present in the upper layers of the circumstellar disk is photodissociated by the far ultraviolet radiation which increases the amount of OH. Further investigations are needed to determine how gas depletion in the inner disk of Herbig Ae/Be stars effects the observed molecular emission.

7.2   Hydrogen Emission

The spectro-astrometric study of Herbig Ae/Be stars provides insights on the emission origins of H I emission. Hydrogen emission is primarily determined to originate from a compact region near the star, in line with spectro-interferometric studies of H I emission. The only source with a pronounced extension in H I emission is HD 259431, an early type star (B6). HD 163296 does show some evidence of extended emission, however, the spectro-astrometric offset is less than 3σ. Modeling of the Paβ emission assuming the emission originates from a Keplerian disk indicates that the observed slight offset is unlikely to form from such a geometry. Instead, it is more likely to come from some outflow from the system as the offset lies perpendicular to the circumstellar disk's position angle. This is consistent with spectro-interferometric observations of Brγ emission. HD 163296 is also associated with a Herbig-Haro outflow that lies perpendicular to the disk position angle.

While the constraints placed on most disks in the survey indicate a small emitting region for H I emission, we are unsure if all systematic effects of the spectro-astrometric analysis with an integral field unit are being properly handled. For the time being, spectro-interferometric observations are recommended for the study of the inner most regions of Herbig Ae/Be star systems.

7.3 Future Work

7.3.1 Molecular Emission

New ground based instruments will be coming online that will provide high spectral resolution over a wide spectral range in the near-infrared (e.g., CRIRES+). Observations of various molecular species taken concurrently will allow us to determine the relative strengths of the molecular emission. This will allow us to constrain the relative abundances of these molecules in the inner disk which will allow us to constrain thermo-chemical models of protoplanetary disks. Observations made with instruments with a wider spectral coverage will allow for the concurrent observation of various rovibrational transitions for each molecule. This will allow for the determination of the temperature and excitation mechanisms of the emitting gas. Also, any asymmetries should persist across each emission feature.

It is unlikely we are able to further constrain water abundances in the inner disk of most Herbig Ae/Be stars based on the current observations in the near-infrared. Water emission is masked by the near-infrared continuum due to dust in most cases. Observations of the photospheric abundances of various atomic species could provide some insights on the gas-to-dust ratio of these systems. If we are able to find sources that show significant dust depletion of the inner disk, more thorough investigations may lead to more detections of water.

The immediate goal to come from the work presented here is to improve thermo-chemical modeling inputs for protoplanetary disk models. The better we understand the constituents of these disks, the more accurate our models can be in regards to the chemistry that is ongoing in the terrestrial planet forming regions. This will provide insights as to what type of organic molecules can form and survive in this region and hopefully lead to a better understanding of the potential atmospheric compositions of planets around other stars.

Appendices

Appendix A Observed Molecules in the Universe

Presented in this appendix is a table of the observed molecules in the universe compiled by McGuire (2018). Tables 1 and 2 show all molecular species observed, while Table 3 lists molecules observed in protoplanetary disks. See McGuire (2018) for sources to studies that detect the individual species.

2 Atoms		3 Atoms		4 Atoms	5 Atoms	6 Atoms	7 Atoms
CH	CP	H_2O	N_2O	NH_3	HC_3N	CH_3OH	CH_3CHO
CN	NH	HCO^+	MgCN	H_2CO	HCOOH	CH_3CN	CH_3CCH
CH^+	SiN	HCN	$H_3{}^+$	HNCO	CH_2NH	NH_2CHO	CH_3NH_2
OH	SO^+	OCS	SiCN	H_2CS	NH_2CN	CH_3SH	CH_2CHCN
CO	CO^+	HNC	AlNC	C_2H_2	H_2CCO	C_2H_4	HC_5N
H_2	HF	H_2S	SiNC	C_3N	C_4H	C_5H	C_6H
SiO	N_2	N_2H^+	HCP	HNCS	SiH_4	CH_3NC	c-C_2H_4O
CS	CF^+	C_2H	CCP	$HOCO^+$	c-C_3H_2	HC_2CHO	CH_2CHOH
SO	PO	SO_2	AlOH	C_3O	CH_2CN	H_2C_4	C_6H^-
SiS	O_2	HCO	H_2O^+	l-C_3H	C_5	C_5S	CH_3NCO
NS	AlO	HNO	H_2Cl^+	$HCNH^+$	SiC_4	HC_3NH^+	HC_5O
C_2	CN^-	HCS^+	KCN	H_3O^+	H_2CCC	C_5N	
NO	OH^+	HOC^+	FeCN	C_3S	CH_4	HC_4H	
HCl	SH^+	SiC_2	HO_2	c-C_3H	HCCNC	HC_4N	
NaCl	HCl^+	C_2S	TiO_2	HC_2N	HNCCC	c-H_2C_3O	
AlCl	SH	C_3	CCN	H_2CN	H_2COH^+	CH_2CNH	
KCl	TiO	CO_2	SiCSi	SiC_3	C_4H^-	C_5N^-	
AlF	ArH^+	CH_2	S_2H	CH_3	CNCHO	HNCHCN	
PN	NS^+	C_2O	HCS	C_3N^-	HNCNH	SiH_3CN	
SiC		MgNC	HSC	PH_3	CH_3O		
		NH_2	NCO	HCNO	NH_3D^+		
		NaCN		HOCN	H_2NCO^+		
				HSCN	$NCCNH^+$		
				HOOH	CH_3Cl		
				l-C_3H^+			
				HMgNC			
				HCCO			
				CNCN			

Table 1: List of detected interstellar molecules with two to seven atoms, categorized by number of atoms, and vertically ordered by detection year.

8 Atoms	9 Atoms	10 Atoms	11 Atoms	12 Atoms	13 Atoms	Fullerenes
$HCOOCH_3$	CH_3OCH_3	$(CH_3)_2CO$	HC_9N	C_6H_6	c-C_6H_5CN	C_{60}
CH_3C_3N	CH_3CH_2OH	$HO(CH_2)_2OH$	CH_3C_6H	n-C_3H_7CN		C_{60}^+
C_7H	CH_3CH_2CN	CH_2CH_2CHO	CH_3CH_2OCHO	i-C_3H_7CN		C_{70}
CH_3COOH	HC_7N	CH_3C_5N	CH_3COOCH_3			
H_2C_6	CH_3C_4H	CH_3CHCH_2O				
CH_2OHCHO	C_8H	CH_3OCH_2OH				
HC_6H	CH_3CONH_2					
CH_2CHCHO	C_8H^-					
CH_2CCHCN	CH_2CHCH_3					
NH_2CH_2CN	CH_3CH_2SH					
CH_3CHNH	HC_7O					
CH_3SiH_3						

Table 2: List of detected interstellar molecules with eight or more atoms, categorized by number of atoms, and vertically ordered by detection year.

2 Atoms	3 Atoms	4 Atoms	5 Atoms	6 Atoms
CN	H_2O	NH_3	HCOOH	CH_3CN
$C^{15}N$	HCO^+	H_2CO	c-C_3H_2	CH_3OH
CH^+	DCO^+	C_2H_2	CH_4	
OH	$H^{13}CO^+$	HC_3N		
CO	HCN			
^{13}CO	DCN			
$C^{18}O$	$H^{13}CN$			
$C^{17}O$	$HC^{15}N$			
H_2	HNC			
HD	N_2H^+			
CS	N_2D^+			
$C^{34}S$	C_2H			
SO	CO_2			

Table 3: List of molecules, including rare isotopic species, detected in protoplanetary disks.

Bibliography

Acke, B., & van den Ancker, M. E. 2006, A&A, 449, 267

Ádámkovics, M., Glassgold, A. E., & Najita, J. R. 2014, ApJ, 786, 135

Ádámkovics, M., Najita, J. R., & Glassgold, A. E. 2016, ApJ, 817, 82

Adams, F. C., Lada, C. J., & Shu, F. H. 1987, ApJ, 312, 788

Adams, S. C., Ádámkovics, M., Carr, J. S., Najita, J. R., & Brittain, S. D. 2019, ApJ, 871, 173

Alecian, E., Catala, C., Wade, G. A., et al. 2008, MNRAS, 385, 391

Alecian, E., Wade, G. A., Catala, C., et al. 2009, MNRAS, 400, 354

—. 2013, MNRAS, 429, 1001

Alexander, R., Pascucci, I., Andrews, S., Armitage, P., & Cieza, L. 2014, Protostars and Planets VI, 475

Allington-Smith, J., & Content, R. 1998, PASP, 110, 1216

Artymowicz, P., & Lubow, S. H. 1994, ApJ, 421, 651

Bailey, J. 1998a, MNRAS, 301, 161

Bailey, J. A. 1998b, in Proc. SPIE, Vol. 3355, Optical Astronomical Instrumentation, ed. S. D'Odorico, 932–939

Banzatti, A., & Pontoppidan, K. M. 2015, ApJ, 809, 167

Banzatti, A., Pontoppidan, K. M., Salyk, C., et al. 2017, ApJ, 834, 152

Barber, R. J., Tennyson, J., Harris, G. J., & Tolchenov, R. N. 2006, MNRAS, 368, 1087

Beck, T. L., Bary, J. S., & McGregor, P. J. 2010, ApJ, 722, 1360

Beck, T. L., McGregor, P. J., Takami, M., & Pyo, T.-S. 2008, ApJ, 676, 472

Benisty, M., Malbet, F., Dougados, C., et al. 2010, A&A, 517, L3

Benisty, M., Stolker, T., Pohl, A., et al. 2017, A&A, 597, A42

Bertout, C., Basri, G., & Bouvier, J. 1988, ApJ, 330, 350

Blake, G. A., & Boogert, A. C. A. 2004, ApJ, 606, L73

Blandford, R. D., & Payne, D. G. 1982, MNRAS, 199, 883

Bouvier, J., Alencar, S. H. P., Boutelier, T., et al. 2007, A&A, 463, 1017

Brannigan, E., Takami, M., Chrysostomou, A., & Bailey, J. 2006, MNRAS, 367, 315

Brittain, S. D., Carr, J. S., Najita, J. R., Quanz, S. P., & Meyer, M. R. 2014, ApJ, 791, 136

Brittain, S. D., Najita, J. R., Carr, J. S., Ádámkovics, M., & Reynolds, N. 2016, ApJ, 830, 112

Brittain, S. D., Simon, T., Najita, J. R., & Rettig, T. W. 2007, ApJ, 659, 685

Brown, J. M., Pontoppidan, K. M., van Dishoeck, E. F., et al. 2013, ApJ, 770, 94

Cabrit, S., Edwards, S., Strom, S. E., & Strom, K. M. 1990, ApJ, 354, 687

Calvet, N., Muzerolle, J., Briceño, C., et al. 2004, AJ, 128, 1294

Carmona, A., van den Ancker, M. E., Henning, T., et al. 2008, A&A, 477, 839

Carr, J. S. 1989, ApJ, 345, 522

Carr, J. S., Tokunaga, A. T., & Najita, J. 2004, ApJ, 603, 213

Cauley, P. W., & Johns-Krull, C. M. 2014, ApJ, 797, 112

—. 2015, ApJ, 810, 5

Chen, X., Launhardt, R., & Henning, T. 2009, ApJ, 691, 1729

Cowley, C. R., Hubrig, S., Castelli, F., & Wolff, B. 2012, A&A, 537, L6

Davies, B., Lumsden, S. L., Hoare, M. G., Oudmaijer, R. D., & de Wit, W.-J. 2010, MNRAS, 402, 1504

Dent, W. R. F., Greaves, J. S., & Coulson, I. M. 2005, MNRAS, 359, 663

Donati, J.-F., Semel, M., Carter, B. D., Rees, D. E., & Collier Cameron, A. 1997, MNRAS, 291, 658

Donehew, B., & Brittain, S. 2011, AJ, 141, 46

Doppmann, G. W., Najita, J. R., Carr, J. S., & Graham, J. R. 2011, ApJ, 738, 112

Dullemond, C. P., & Monnier, J. D. 2010, ARA&A, 48, 205

Eisner, J. A., Graham, J. R., Akeson, R. L., & Najita, J. 2009, ApJ, 692, 309

Eisner, J. A., Rieke, G. H., Rieke, M. J., et al. 2015, MNRAS, 447, 202

Espaillat, C., Calvet, N., D'Alessio, P., et al. 2007, ApJ, 670, L135

Fairlamb, J. R., Oudmaijer, R. D., Mendigutía, I., Ilee, J. D., & van den Ancker, M. E. 2015, MNRAS, 453, 976

Fairlamb, J. R., Oudmaijer, R. D., Mendigutia, I., Ilee, J. D., & van den Ancker, M. E. 2017, MNRAS, 464, 4721

Fedele, D., Bruderer, S., van Dishoeck, E. F., et al. 2012, A&A, 544, L9

Fedele, D., Pascucci, I., Brittain, S., et al. 2011, ApJ, 732, 106

Fedele, D., van den Ancker, M. E., Acke, B., et al. 2008, A&A, 491, 809

Fedele, D., Bruderer, S., van Dishoeck, E. F., et al. 2013, A&A, 559, A77

Folsom, C. P., Bagnulo, S., Wade, G. A., et al. 2012, MNRAS, 422, 2072

France, K., Herczeg, G. J., McJunkin, M., & Penton, S. V. 2014, ApJ, 794, 160

France, K., Burgh, E. B., Herczeg, G. J., et al. 2012, ApJ, 744, 22

Fukagawa, M., Tamura, M., Itoh, Y., Hayashi, S. S., & Oasa, Y. 2003, ApJ, 590, L49

Furlan, E., Sargent, B., Calvet, N., et al. 2007, ApJ, 664, 1176

Gaia Collaboration, Brown, A. G. A., Vallenari, A., et al. 2016, A&A, 595, A2

—. 2018, A&A, 616, A1

Garcia Lopez, R., Kurosawa, R., Caratti o Garatti, A., et al. 2016, MNRAS, 456, 156

Garcia Lopez, R., Natta, A., Testi, L., & Habart, E. 2006, A&A, 459, 837

Garcia Lopez, R., Tambovtseva, L. V., Schertl, D., et al. 2015, A&A, 576, A84

Gordon, I. E., Rothman, L. S., Hill, C., et al. 2017, J. Quant. Spec. Radiat. Transf., 203, 3

Grady, C. A., Devine, D., Woodgate, B., et al. 2000, ApJ, 544, 895

Grady, C. A., Woodgate, B., Torres, C. A. O., et al. 2004, ApJ, 608, 809

Guimarães, M. M., Alencar, S. H. P., Corradi, W. J. B., & Vieira, S. L. A. 2006, A&A, 457, 581

Haisch, Jr., K. E., Lada, E. A., & Lada, C. J. 2001, ApJ, 553, L153

Hartigan, P., Edwards, S., & Ghandour, L. 1995, ApJ, 452, 736

Hein Bertelsen, R. P., Kamp, I., van der Plas, G., et al. 2016a, A&A, 590, A98

—. 2016b, MNRAS, 458, 1466

Herbig, G. H. 1960, ApJS, 4, 337

Herczeg, G. J., Wood, B. E., Linsky, J. L., Valenti, J. A., & Johns-Krull, C. M. 2004, ApJ, 607, 369

Hillenbrand, L. A., Strom, S. E., Vrba, F. J., & Keene, J. 1992, ApJ, 397, 613

Hinkle, K. H., Cuberly, R. W., Gaughan, N. A., et al. 1998, in Proc. SPIE, Vol. 3354, Infrared Astronomical Instrumentation, ed. A. M. Fowler, 810–821

Hinkle, K. H., Joyce, R. R., Sharp, N., & Valenti, J. A. 2000, in Proc. SPIE, Vol. 4008, Optical and IR Telescope Instrumentation and Detectors, ed. M. Iye & A. F. Moorwood, 720–728

Hinkle, K. H., Blum, R. D., Joyce, R. R., et al. 2003, in Proc. SPIE, Vol. 4834, Discoveries and Research Prospects from 6- to 10-Meter-Class Telescopes II, ed. P. Guhathakurta, 353–363

Hirota, T., Bushimata, T., Choi, Y. K., et al. 2008, PASJ, 60, 37

Hone, E., Kraus, S., Davies, C. L., et al. 2019, A&A, 623, A38

Hubrig, S., Schöller, M., Savanov, I., et al. 2010, Astronomische Nachrichten, 331, 361

Hubrig, S., Mikulášek, Z., González, J. F., et al. 2011, A&A, 525, L4

Hussain, G. A. J., & Alecian, E. 2014, in IAU Symposium, Vol. 302, Magnetic Fields throughout Stellar Evolution, ed. P. Petit, M. Jardine, & H. C. Spruit, 25–37

Ilee, J. D., Fairlamb, J., Oudmaijer, R. D., et al. 2014, MNRAS, 445, 3723

Isella, A., Testi, L., Natta, A., et al. 2007, A&A, 469, 213

Isella, A., Guidi, G., Testi, L., et al. 2016, Physical Review Letters, 117, 251101

Järvinen, S. P., Carroll, T. A., Hubrig, S., et al. 2019, MNRAS, 486, 5499

Kama, M., Folsom, C. P., & Pinilla, P. 2015, A&A, 582, L10

Käufl, H.-U., Ballester, P., Biereichel, P., et al. 2004, in Proc. SPIE, Vol. 5492, Ground-based Instrumentation for Astronomy, ed. A. F. M. Moorwood & M. Iye, 1218–1227

Kley, W., & Dirksen, G. 2006, A&A, 447, 369

Kluska, J., Kraus, S., Davies, C. L., et al. 2018, ApJ, 855, 44

Koenigl, A. 1991, ApJ, 370, L39

Kozlova, O. V. 2004, Astrophysics, 47, 287

Kramida, A. E. 2010, Atomic Data and Nuclear Data Tables, 96, 586

Kraus, S., Preibisch, T., & Ohnaka, K. 2008a, ApJ, 676, 490

Kraus, S., Hofmann, K.-H., Benisty, M., et al. 2008b, A&A, 489, 1157

Kunde, V. R., & Maguire, W. C. 1974, J. Quant. Spec. Radiat. Transf., 14, 803

Kurosawa, R., Harries, T. J., & Symington, N. H. 2006, MNRAS, 370, 580

Labadie, L., Matter, A., Kreplin, A., et al. 2014, in Proc. SPIE, Vol. 9146, Optical and Infrared Interferometry IV, 91462T

Lagage, P.-O., Doucet, C., Pantin, E., et al. 2006, Science, 314, 621

Leinert, C., Richichi, A., & Haas, M. 1997, A&A, 318, 472

Leinert, C., Richichi, A., Weitzel, N., & Haas, M. 1994, in Astronomical Society of the Pacific Conference Series, Vol. 62, The Nature and Evolutionary Status of Herbig Ae/Be Stars, ed. P. S. The, M. R. Perez, & E. P. J. van den Heuvel, 155

Lord, S. D. 1992, A new software tool for computing Earth's atmospheric transmission of near- and far-infrared radiation, Tech. rep.

Maaskant, K. M., Min, M., Waters, L. B. F. M., & Tielens, A. G. G. M. 2014, A&A, 563, doi:10.1051/0004-6361/201323137

Maciejewski, W., & Binney, J. 2001, MNRAS, 323, 831

Mamajek, E. E., Meyer, M. R., Hinz, P. M., et al. 2004, ApJ, 612, 496

Mandell, A. M., Bast, J., van Dishoeck, E. F., et al. 2012, ApJ, 747, 92

Mandell, A. M., Mumma, M. J., Blake, G. A., et al. 2008, ApJ, 681, L25

Marconi, A., Axon, D. J., Capetti, A., et al. 2003, ApJ, 586, 868

Martin-Zaïdi, C., Augereau, J.-C., Ménard, F., et al. 2010, A&A, 516, A110

Martin-Zaïdi, C., van Dishoeck, E. F., Augereau, J.-C., Lagage, P.-O., & Pantin, E. 2008a, A&A, 489, 601

Martin-Zaïdi, C., Deleuil, M., Le Bourlot, J., et al. 2008b, A&A, 484, 225

McGregor, P. J., Hart, J., Conroy, P. G., et al. 2003, in Proc. SPIE, Vol. 4841, Instrument Design and Performance for Optical/Infrared Ground-based Telescopes, ed. M. Iye & A. F. M. Moorwood, 1581–1591

McGuire, B. A. 2018, ApJS, 239, 17

McLean, I. S., Becklin, E. E., Bendiksen, O., et al. 1998, in Proc. SPIE, Vol. 3354, Infrared Astronomical Instrumentation, ed. A. M. Fowler, 566–578

Meeus, G., Waters, L. B. F. M., Bouwman, J., et al. 2001, A&A, 365, 476

Meeus, G., Montesinos, B., Mendigutía, I., et al. 2012, A&A, 544, A78

Mendigutía, I., Calvet, N., Montesinos, B., et al. 2011, A&A, 535, A99

Mendigutía, I., de Wit, W. J., Oudmaijer, R. D., et al. 2015a, MNRAS, 453, 2126

Mendigutía, I., Oudmaijer, R. D., Mourard, D., & Muzerolle, J. 2017, MNRAS, 464, 1984

Mendigutía, I., Oudmaijer, R. D., Rigliaco, E., et al. 2015b, MNRAS, 452, 2837

Mendigutía, I., Brittain, S., Eiroa, C., et al. 2013, ApJ, 776, 44

Menu, J., van Boekel, R., Henning, T., et al. 2015, A&A, 581, A107

Mottram, J. C., Vink, J. S., Oudmaijer, R. D., & Patel, M. 2007, MNRAS, 377, 1363

Mould, J. R., Hall, D. N. B., Ridgway, S. T., Hintzen, P., & Aaronson, M. 1978, ApJ, 222, L123

Muro-Arena, G. A., Dominik, C., Waters, L. B. F. M., et al. 2018, A&A, 614, A24

Muzerolle, J., Calvet, N., & Hartmann, L. 1998a, ApJ, 492, 743

Muzerolle, J., Hartmann, L., & Calvet, N. 1998b, AJ, 116, 2965

—. 1998c, AJ, 116, 455

Najita, J., Carr, J. S., Glassgold, A. E., Shu, F. H., & Tokunaga, A. T. 1996, ApJ, 462, 919

Najita, J. R., & Ádámkovics, M. 2017, ApJ, 847, 6

Ochsenbein, F., Bauer, P., & Marcout, J. 2000, A&AS, 143, 23

Palla, F., & Stahler, S. W. 1993, ApJ, 418, 414

Petrov, P. P., Kurosawa, R., Romanova, M. M., et al. 2014, MNRAS, 442, 3643

Podio, L., Garcia, P. J. V., Bacciotti, F., et al. 2008, A&A, 480, 421

Pontoppidan, K. M., Blake, G. A., & Smette, A. 2011, ApJ, 733, 84

Pontoppidan, K. M., Blake, G. A., van Dishoeck, E. F., et al. 2008, ApJ, 684, 1323

Pontoppidan, K. M., Dullemond, C. P., Blake, G. A., et al. 2007, ApJ, 656, 991

Pontoppidan, K. M., Salyk, C., Blake, G. A., et al. 2010, ApJ, 720, 887

Porter, J. M., Oudmaijer, R. D., & Baines, D. 2004, A&A, 428, 327

Raman, A., Lisanti, M., Wilner, D. J., Qi, C., & Hogerheijde, M. 2006, AJ, 131, 2290

Rice, W. K. M., Armitage, P. J., Wood, K., & Lodato, G. 2006, MNRAS, 373, 1619

Rothman, L. S., Barbe, A., Benner, D. C., et al. 2003, J. Quant. Spec. Radiat. Transf., 82, 5

Rothman, L. S., Gordon, I. E., Babikov, Y., et al. 2013, J. Quant. Spec. Radiat. Transf., 130, 4

Salyk, C., Blake, G. A., Boogert, A. C. A., & Brown, J. M. 2011a, ApJ, 743, 112

Salyk, C., Pontoppidan, K. M., Blake, G. A., et al. 2008, ApJ, 676, L49

Salyk, C., Pontoppidan, K. M., Blake, G. A., Najita, J. R., & Carr, J. S. 2011b, ApJ, 731, 130

Schleicher, D. G., & Ahearn, M. F. 1982, ApJ, 258, 864

Shu, F., Najita, J., Ostriker, E., et al. 1994, ApJ, 429, 781

Siess, L., Dufour, E., & Forestini, M. 2000, A&A, 358, 593

Skinner, S. L., & Yamauchi, S. 1996, ApJ, 471, 987

Stahler, S. W., & Palla, F. 2005, The Formation of Stars, 865

Stelzer, B., Micela, G., Hamaguchi, K., & Schmitt, J. H. M. M. 2006, A&A, 457, 223

Strom, K. M., Strom, S. E., Edwards, S., Cabrit, S., & Skrutskie, M. F. 1989, AJ, 97, 1451

Swartz, D. A., Drake, J. J., Elsner, R. F., et al. 2005, ApJ, 628, 811

Takami, M., Bailey, J., & Chrysostomou, A. 2003, A&A, 397, 675

Thé, P. S., de Winter, D., & Perez, M. R. 1994, A&AS, 104, 315

Thi, W.-F., & Bik, A. 2005, A&A, 438, 557

Thi, W. F., van Dishoeck, E. F., Blake, G. A., et al. 2001, ApJ, 561, 1074

Troutman, M. R. 2010, PhD thesis, Clemson University

Valenti, J. A., Fallon, A. A., & Johns-Krull, C. M. 2003, ApJS, 147, 305

Valenti, J. A., Johns-Krull, C. M., & Linsky, J. L. 2000, ApJS, 129, 399

van Boekel, R., Min, M., Waters, L. B. F. M., et al. 2005, A&A, 437, 189

van der Marel, N., van Dishoeck, E. F., Bruderer, S., et al. 2013, Science, 340, 1199

van der Plas, G., van den Ancker, M. E., Fedele, D., et al. 2008, A&A, 485, 487

van der Plas, G., van den Ancker, M. E., Waters, L. B. F. M., & Dominik, C. 2015, A&A, 574, A75

Venn, K. A., & Lambert, D. L. 1990, ApJ, 363, 234

Verhoeff, A. P., Min, M., Acke, B., et al. 2010, A&A, 516, A48

Vieira, S. L. A., Corradi, W. J. B., Alencar, S. H. P., et al. 2003, AJ, 126, 2971

Vink, J. S., Drew, J. E., Harries, T. J., & Oudmaijer, R. D. 2002, MNRAS, 337, 356

Vioque, M., Oudmaijer, R. D., Baines, D., Mendigutía, I., & Pérez-Martínez, R. 2018, ArXiv e-prints, arXiv:1808.00476

Walsh, C., Nomura, H., & van Dishoeck, E. 2015, A&A, 582, A88

Waters, L. B. F. M., Trams, N. R., & Waelkens, C. 1992, A&A, 262, L37

Waters, L. B. F. M., & Waelkens, C. 1998, ARA&A, 36, 233

Weigelt, G., Grinin, V. P., Groh, J. H., et al. 2011, A&A, 527, A103

Weinberger, A. J., Becklin, E. E., Schneider, G., et al. 1999, ApJ, 525, L53

Whelan, E., & Garcia, P. 2008, in Lecture Notes in Physics, Berlin Springer Verlag, Vol. 742, Jets from Young Stars II, ed. F. Bacciotti, L. Testi, & E. Whelan, 123

Whelan, E. T., Huélamo, N., Alcalá, J. M., et al. 2015, A&A, 579, A48

Whelan, E. T., Ray, T. P., & Davis, C. J. 2004, A&A, 417, 247

Zhu, Z., Nelson, R. P., Dong, R., Espaillat, C., & Hartmann, L. 2012, ApJ, 755, 6